DERIVING THE INTERNAL BONY STRUCTURE OF THE COCHLEA FROM HIGH-RESOLUTION μCT IMAGES FOR TRANSLATION TO LOW-RESOLUTION IMAGE-BASED CONSTRUCTION OF PERSON-SPECIFIC COMPUTATIONAL MODELS OF COCHLEAR IMPLANTS

by

René Human-Baron

Submitted in partial fulfilment of the requirements for the degree

Philosophiae Doctor (Biosystems)

in the

Department of Electrical, Electronic and Computer Engineering

Faculty of Engineering, Built Environment and Information Technology

UNIVERSITY OF PRETORIA

December 2019

SUMMARY

DERIVING THE INTERNAL BONY STRUCTURE OF THE COCHLEA FROM HIGH-RESOLUTION µCT IMAGES FOR TRANSLATION TO LOW-RESOLUTION IMAGE-BASED CONSTRUCTION OF PERSON-SPECIFIC COMPUTATIONAL MODELS OF COCHLEAR IMPLANTS

by

René Human-Baron

Supervisor: Prof. T. Hanekom

Department: Electrical, Electronic and Computer Engineering

University: University of Pretoria

Degree: Philosophiae Doctor in Biosystems

Keywords: µCT; anatomical landmarks; cochlear spirals; cochlear implant; cochlear anatomy; dynamic range; automate landmark-based search fields; obscured spirals

To investigate cochlear implant (CI) performance, geometric computational models of the cochlea have been used to assess and optimise electrode insertion strategies and to investigate current flow through the cochlear volume as a result of intra-cochlear stimulation. Most of these models are derived low-resolution computed tomography (CT) and radiographic scans of humans or high-resolution histological sections of cochleae that are not viable for *in vivo* studies. Often these models lack a significant set of detail, still use a generic shape of the inner structures of the cochlea or obscured structures and are not clinically translatable. A method for the predication of obscured landmarks from reference landmarks is needed to generate user-specific computational models of the cochlea if the data source is of low quality. A standard set of prediction polynomial functions derived from high-resolution µCT scans needs to be developed and applied to clinically available CT images of the cochlea. Although histological sections of the human cochlea provide the best

resolution of the cochlear structures, midmodialar sequential sectioning of the cochlea is not possible. µCT scans provide a solution, as the images are still of high quality and allow for detailed measurement of cochlear parameters on midmodiolar sections. Secondly, the more recent construction of a knowledge-based automated landmark computational model needs to be refined. The search fields that the automated models template uses to place a landmark need to be standardised and should have the ability to morph the cochlear shape together with the inner bony structures. Such models are of great clinical importance, as they can be generated much more quickly to inform CI surgeons on the individual cochlear anatomy of a CI patient and maintenance of CI.

Lastly, the effect that taxonomic class has on the functional implications of an implanted electrode array has yet to be determined. The cochlear geometry that best predicts the location of the electrode array is important, as it has a significant implication for hearing outcomes.

This thesis assesses the anatomical geometric factors that affect inter-person variations at the peripheral-electrode interface by developing a pre-operative approach to person-specific model design for implant candidates. This approach aims to increase the accuracy and details of geometric parameters that are available for model construction and integrate the image data into three-dimensional (3D) computational volume conduction models. The study used a landmark-based approach to measure the cochlear parameters that contribute to cochlear variation, as well as the development of algorithms to derive obscured landmarks from consistently available cochlear landmarks. A workflow in the form of a custom script `UPCochlea.m` that describes the technical aspects of landmark analysis was created to describe each cochlea algorithmically and to extract spiral trajectories that describe cochlear anatomy. Polynomial algorithms for the description of each spiral were created for use as standard for determining each cochlear class and the prediction of obscured spirals on clinically available data. This is the first study of its kind to describe all eight spirals that constitute the cochlea and spiral lamina.

Automatic generation of user-specific landmark-based 3D computational models is a rapid process that can easily be translated into a clinical tool that may inform surgeons, manufacturers of CI's and bio-engineers on the maintenance of such models. By refining the search fields for the template that landmark-based automated cochlear computational models

search for a landmark to be placed, more accurate automated computational models could be generated.

Psychometric data from CI users are correlated with the anatomical dimensions, their taxonomic classification and electrode locations derived from postoperative patient scans to determine the factors, if any, that may affect electrode array locations and thus the functional outcomes of CI users. The factors that contribute to speech and hearing outcomes may be used to optimise the parameter settings for CI user device programming.

DEDICATION

This thesis is dedicated to my dear husband, Andreas Baron, a strong melanoma fighter and survivor. You are a true warrior whom fought hard battle with the black beast. May it forever be conquered. Our Lord is stronger than any disease.

ACKNOWLEDGEMENTS

"Praise be to the Lord, To God our Saviour who daily bears our burdens." Psalm 68:19

I wish to thank:

- My dear husband, Andreas for his love and for always cheering me on; you are my everything and I appreciate you more than I can say.
- My two angels Liam (5) and Lexi (3) who were born while I was busy with this work; you made it all worthwhile
- Prof Tania Hanekom, my study leader for her patience and unwavering support. For being there during the toughest times and encouraging me; you are a true role model. I cannot wait to continue our research journey together.
- The Biogroup head, Prof Johan Hanekom for his kindness and willingness to lend a hand whenever I needed something
- Prof P Soma, my HOD for supporting me and allowing me the time to complete this study.
- My parents for helping out with Liam and Lexi whenever possible
- The National Research Fund for their financial contribution for two years.

"Let us run with perseverance the race marked out for us, fixing our eyes on Jesus the Pioneer and Perfecter of our Faith." Hebrews 12:1b-2a

LIST OF ABBREVIATIONS

µCT	microCT
µm	micrometer
3D	three-dimensional
AL	angular length
AMG	automated model generator
BM	basilar membrane
C- or M-level	comfort level
CBCT	cone beam computed tomography
CI	cochlear implant
CIMVW	cochlear implant model validation workflow
CI's	cochlear implants
CL	cochlear length
CSRF	cochlear reference spiral framework
CN X	vagus nerve
CNII	olfactory nerve
CNVII	facial nerve
CNVIII	vestibulocochlear nerve
CT	computed tomography
DR	dynamic range
EM	expectation maximum
IAC	internal acoustic canal
IAM	internal acoustic meatus
ILS	inferolateral spiral
IS	inferior spiral
LMS	least mean squared
LS	lateral spiral
LSH	height of the lateral spiral
LSL	lateral spiral lamina
Matlab	matrix laboratory
mm	millimeter

mm^3	cubic millimeter
MRI	magnetic resonance imaging
MRM or µMR	magnetic resonance microscopy
MS	medial spiral
MSL	medial spiral lamina
NECSA	Nuclear Energy Corporation of South Africa
MAE	mean absolute error
NMAE	normalized mean absolute error
OoC	Organ of Corti
OSL	osseous spiral lamina
OW	oval window
PCA	principal component analysis
PNE	percentage normalized error
PNMAE	percentage normalized mean absolute error
RM	Reisnner's membrane
ROI	region of interest
RW	round window
RWM	round window membrane
SGC	spiral ganglion cell
SL	spiral lamina
SLS	superolateral spiral
SM	scala media
SS	superior spiral
ST	scala tympani
SV	scala vestibuli
T-level	threshold
TM	tectorial membrane
VC	volume conduction

TABLE OF CONTENTS

CHAPTER 1 INTRODUCTION

1.1 CHAPTER OVERVIEW

1.1.1 Context of the problem

Cochlear implants (CIs) have been used as a rehabilitative tool for the treatment of severe hearing loss. Over the last few decades, significant improvements in the design and development of CIs have been made. Still, many users experience variable speech and language outcomes, with some having no hearing benefit at all. Such variability makes predicting hearing outcomes very difficult and has prompted further research in the hope of finding solutions to optimise hearing restoration. To address the variance experienced by CI users, computational modelling that describes how the biological cochlear system reacts in an electrically stimulated environment has been used.

These geometrical computational models should represent the morphologies and dimensions similar to the real cochlear structures. Recently user-specific models have been created to understand the factors that may contribute to the variable outcomes better. The anatomical details included in these user-specific models are however lacking, as they are mostly derived from low-resolution images. A need exists for parameters that describe the cochlear spirals that constitute the cochlea and that reflect individual variations, for the generation of three-dimensional (3D) computational models of higher geometric accuracy.

Even though cochlear anatomy can be better visualised using higher resolution images, such as those derived from histological sections, micro computed tomography (μCT) scans and magnetic resonance microscopy (MRM) images, these modalities are not suitable for use in *in vivo* and clinical settings. Most often, clinicians and researchers are presented with low-

resolution data in the form of CT scans. The question then arises: How well and with what accuracy can one determine the anatomical landmarks that describe the cochlear anatomy and its variation? It is important to determine which of these landmarks are useful for inclusion in user-specific model generation and which can be used to derive the smaller inner structures that are obscured by either electrode or metal artefacts or are too small to visualise on clinically available CT scans. A standardised method is needed to obtain obscured spirals (from the measured landmarks that describe these spirals) from visible or reference spirals and to assess the accuracy with which these spirals can be determined.

Three-dimensional modelling of the cochlea for volume conduction studies uses a few landmarks that are visible on clinical CTs to reconstruct a detailed representation of a user's cochlea. Since the inner structure of the cochlea is not visible, a fixed inner structure template is morphed onto these landmarks to fill in obscured structures. Whether the obscured structures are placed in the correct locations is, however, unknown since the low-resolution source images do not allow a direct assessment of the integrity of the model and ultimately of a specific model generator process. A method is thus required to (i) assess the fidelity of a model (and model generator process) against a known reference, and (ii) inform a strategy for improvement if necessary. This is particularly important in the domain of automatic model generators where manual landmark identification is replaced by an algorithmic approach to landmark detection in an attempt to generate fast, accurate and detailed computational models of the cochlea for clinical application. The search fields used by the automated landmarks to place a valid landmark are still needed. These search fields need to be quantified to improve landmark-based automated computational modelling of the cochlea details. Manual generation of landmark-based computational models is a time-consuming process and has been translated into an automated landmark-based modelling approach in the work done by Bioengineering@UP.

In addition, the cause of the variable outcomes in psychoacoustic measures in CI users' needs to be investigated. The anatomical factors that affect variation in outcomes, such as cochlear taxonomy (class) and electrode position relative to the target neural elements, need to be investigated to advise clinicians, manufacturers and bio-engineers on which parameters

need to be considered during the surgical approach, electrode array design and the construction of 3D computational volume conduction models.

The thesis addresses the following:
Firstly, high-resolution µCT scans are used to define a standardised set of landmarks to describe the 3D spiralling nature of the cochlea for model construction. This cochlear reference spiral framework (CSRF) includes the spiral lamina, since this structure may be used to adapt the inner-structure template better to the specific morphology of an individual. Polynomial equations are derived to describe each spiral that constitutes the cochlea, as well as those describing the spiral lamina. These polynomial equations are then used as reference spirals for the derivation of obscured spirals when using an image source of low quality, which is mostly the case when modelling the cochlea of live CI users. The accuracy with which obscured landmarks can be derived from visible parameters is given.

Secondly, a workflow is developed to apply the CSRF as a reference to test the integrity of specific 3D models and that of model generation protocols. The CSRF model-integrity test is applied to a specific automated landmark-based 3D model generator. Validation of the test is performed against the full set of manually measured landmark spirals as identified on µCT images for which automated landmark-based models were also created. Application of the CSRF model-integrity test on low-resolution CT-images is then performed to assess the fidelity of models constructed through this model generator for live users. Finally, analysis of the performance of the automated model generator (AMG) against the reference spirals is used to inform refinements to the current AMG that could improve the accuracy of the models it produces.

Thirdly, the CSRF is applied to derive the location of a number of CI users' electrode arrays relative to cochlear geometry. A comparison of electrode trajectory with the spiral trajectories of the cochlea is used to determine which cochlear spirals may influence electrode location. This section of the work further investigates the interrelation between electrode location and psychoacoustic measures.

1.1.2 Research gap

The study addresses the need for an analytical description of anatomical cochlear variation in terms of cochlear class, the prediction of obscured cochlear spirals as well as the accuracy of this method. The application of the resulting CSRF addresses a gap in evaluating the integrity of CI models and model generators, and it provides a reference that can inform the steps that are required to develop new model generators or improve existing ones. Finally, the CSRF provides a means to investigate the variation in cochlear implantation outcomes by providing a more detailed comparison of the trajectory of the cochlear spirals of each cochlear class and the spiral of the electrode array with the functional outcomes of a selected CI user than was previously possible.

1.2 RESEARCH OBJECTIVES AND QUESTIONS

The research objectives are to develop a tool

1. for the standardisation and extraction of the cochlear spirals that describe the spiralling nature of the cochlea and its inner bony structures for each cochlear class;
2. to calculate obscured cochlear spirals when the data source is of low quality;
3. to assess the integrity of an automated landmark-based computational model of the cochlea; and
4. to investigate the anatomical factors, including cochlear class, that affect electrode position and the associated interrelation between anatomy and outcomes of cochlear implantation.

The research questions addressed by the study are the following:

1. How accurately can the spiralling nature of the cochlea be algorithmically described from measured landmarks that describe these spirals? Can the cochlear spirals for each cochlear class be standardised?
2. How well can the trajectory of obscured cochlear spirals be derived from reference spirals for which all cochlear landmarks are visible? What is the accuracy of such a method?

3. Can a CSRF be used to validate the integrity of an existing automated model generator and what would such a workflow entail?
4. What is the outcome of the inclusion of refined search fields in landmark-based automated computational models of the cochlea?
5. Which of the quantified cochlear spirals, if any, contribute to the functional outcomes of cochlear implantation? Do the spiral trajectories of the cochlea predict the position of the electrode array? What is the effect of the electrode position on the functional outcomes influencing the objective outcomes after CI insertion?

1.3 APPROACH

The approach in this study was to construct a cochlear spiral reference database from a high-resolution image set. High-resolution µCT images of a collection of temporal bones and dry skulls were obtained. From these images, landmarks were manually digitised through the use of open-source (Image J[1]) and commercial (VGStudio[2]) image-processing software. The raw measured landmark data were subsequently processed through custom Matlab[3] scripts to produce a standardised set of cochlear spirals. These spirals were subsequently fitted with sixth order polynomial equations to produce an analytical description of the spirals. The analytical descriptors were used to derive a set of predictor coefficients that describe the obscured spirals as a function of spirals that may readily be digitised from low-resolution images. Furthermore, the reference spirals were used to classify cochleae according to taxonomy with regard to the vertical trajectory of the cochlea. The CSRF thus constitutes polynomial descriptors for the reference spirals as well as polynomial predictors for obscured spirals according to cochlear taxonomy (for cases where this is known) as well as for the pooled dataset where the cochlear class is unknown. The application of the CSRF is then demonstrated as a tool to assess the integrity of 3D models that describe user-specific cochlear geometry and to validate the particular model generation workflow that was used to create these models. This is done through an analysis of the estimated error between the

[1] https://imagej.nih.gov/ij/
[2] https://www.volumegraphics.com/
[3] https://www.mathworks.com/

spirals produced for several cochleae by a specific automated 3D cochlear model generator, the measured spirals for the same cochleae and the trajectories of the obscured spirals as predicted by the polynomial predictors. The comparison is also performed by a custom Matlab[1] script. Finally, the CSRF is used to calculate the location of several electrode arrays implanted in live cochleae with information about the location of the spiral lamina, i.e. presumably a more detailed description of the location of the neurons relative to the electrode array than was previously possible. This allows assessment of the effect of cochlear anatomy on thresholds and dynamic range outcomes in CI users.

Null hypothesis (H0): A CSRF can be constructed for the extraction and description of cochlear spirals of each class that reiterates the anatomical variation in cochlear anatomy and can be applied for the accurate prediction of obscured spirals. The CSRF can be used to validate the integrity of an AMG. Algorithmically described cochlear spirals, cochlear taxonomy and the position of the electrode array have a large influence on the functional outcomes of cochlear implantation.

Alternative hypothesis (HA): The spirals that constitute the cochlea cannot be described using polynomial equations, nor can these spirals be used as a reference for the prediction of the trajectory of obscured cochlear spirals. An improved method is needed to validate search fields for landmark-based automated computational modelling. Functional outcomes of cochlear implantation are not significantly influenced by cochlea taxonomy or electrode array position.

[1] https://www.mathworks.com/

1.4 RESEARCH GOALS

The goal of this study was to create a detailed cochlear reference spiral framework from landmarks measured from high-resolution data and to interpret the data by using custom Matlab[1] algorithms for the classification of cochleae into the taxonomy and for the interpretation of the cochlear spirals that constitute the cochlea and spiral lamina. The reference spirals were subsequently processed in a second Matlab[2] script algorithmically describing each spiral of the cochlea and spiral lamina. This script allowed for the prediction of spirals, which may be obscured on data sources of low resolution. The goal of the study was to develop a standard set of polynomial equations that can be used to refine the development of user-specific computational modelling of the cochlea. The study further aimed to define search fields for the creation of more rapid landmark-based automated computational models that can be translated into a clinical setting. The anatomical class and spirals that constitute the cochlea and spiral lamina are correlated with the functional outcomes.

1.5 RESEARCH CONTRIBUTION

A first contribution is made in the form of detailed techniques that assist in extracting the anatomical landmarks, data refinement and classification of cochleae. A method by which obscured landmarks proposed for inclusion in 3D computational modelling of the cochlea is given. The second contribution is made by proposing a validation tool for 3D cochlear model integrity. The third contribution is made by evaluating which anatomical landmarks, if any, are correlated with the electrode location and/or hearing performance data of CI patients.

[1] https://www.mathworks.com/
[2] https://www.mathworks.com/

1.6 RESEARCH OUTPUTS

1.6.1 Submitted peer-reviewed journal articles

Human-Baron, R., Hanekom, T. and Hanekom, J.J. (2019). "Non-invasive landmark-based approach to computational reconstruction of the human cochlea. Variations in the dimensions of the human cochlea using microCT and CT scans: implications for computational modelling of the auditory periphery", *Journal of Medical Imaging Analysis.*

1.6.2 Peer-reviewed journal articles in preparation

Human-Baron, R., Hanekom, T. and Hanekom, J.J. (2019). "Prediction of the trajectory of obscured cochlear spirals for the development of three-dimensional computational modelling."

Human-Baron, R., Hanekom, T. and Hanekom, J.J. (2019). "Non-invasive landmark-based approach to computational reconstruction of the human cochlea – Translation to automated geometry reconstruction."

Human-Baron, R., Hanekom, T. and Hanekom, J.J., "Functional consequences of human cochlear taxonomy: Experimental assessments of the device performance of participating implant users." *To be determined.*

1.6.3 Conference outputs

Hanekom, T., Asvat, R., Baron, R., Malherbe, T.K., Badenhorst, W. and Hanekom, J.J., "Cochlear implants: Quantifying user-specificity in peripheral neural responses", University of Pretoria 4th Neuroscience Day, University of Pretoria, Pretoria, 9 May 2013.

Asvat, R., Human-Baron, R., Hanekom, T. and Hanekom, J.J. (2016). "User-specificity of anatomical landmarks of the cochlea for use in computational models", 44th Annual

Conference of the Anatomical Society of Southern Africa, 8-12 May 2016, Bloemfontein, Free State, South Africa.

Havenga, W., Asvat, R., Human-Baron, R., Hanekom, T. and Hanekom, J.J. (2017). "Variations in the macro-anatomic structure of the cochlea", 45th Annual Conference of the Anatomical Society of Southern Africa, 23-26 April 2017, Langebaan, Western Cape, South Africa.

Human-Baron, R., Asvat, R., Hanekom, T. and Hanekom, J.J. (2017). "Reconstruction of the cochlea using geometric parameters: Technical aspects", 45th Annual Conference of the Anatomical Society of Southern Africa, 23-26 April 2017, Langebaan, Western Cape, South Africa.

Human-Baron, R., Asvat, R., Hanekom, T. and Hanekom, J.J. (2017). "Determining the number of turns of the human cochlea across imaging modalities", 45th Annual Conference of the Anatomical Society of Southern Africa, 23-26 April 2017, Langebaan, Western Cape, South Africa.

Human-Baron, R., Hanekom, T. and Hanekom, J.J., and Uys A. (2019). "Accuracy with which modalities suitable to image live CI users can represent cochlear anatomy", 47th Annual Conference of the Anatomical Society of Southern Africa, 07-10 April 2019, Pilansberg, North West, South Africa.

1.7 OVERVIEW OF STUDY

An overview of the thesis is presented in Figure 1.1. The first part of the study involves the derivation of a knowledge and predictor base Refer to figure 1.1a. The knowledge base is derived from measurement of a set of predefined landmarks on µCT scans of dry skulls. The knowledge base is optimised and used to inform a predictor base. The predictor base involves the prediction of the different spiral trajectories that describe cochlear morphology from known spiral trajectories in cases where a spiral may be obscured. Predictor polynomial coefficients are determined. The next part of the study involves the application of the predictor base to CT scans of live cochleae without and with an electrode array inserted.

Validation of the knowledge and predictor base is performed using error analysis. Next the knowledge and predictor base are applied to an automated model generator (AMG) developed by the Bio-engineering research group at the University of Pretoria. The derived knowledge base for the AMG for pooled cochlea and per cochlear class is compared to the manual digitization of each cochlear spiral and the predictor base to test the performance and integrity of the AMG, i.e. how well the AMG can predict cochlear morphology. Finally as given in figure 1.1b, the user outcomes of CI users (dynamic range, threshold and comfort-level) are correlated to the manually digitized spirals to determine which spiral influence these outcomes. The spiral trajectory of the electrode array is also determined and correlated to user outcomes.

In Chapter 2 a review of relevant literature is given to lay down a foundation for the study presented. A literature study on the application of imaging in temporal bone assessment and landmarks that have been used by other researchers in an attempt to describe cochlear anatomy is given. The literature review includes cochlear variations reported in the literature, methods to assess cochlear geometry, cochlear parameters that are required to construct computational cochlear models, methods to determine electrode location and the anatomical factors that have been found to contribute to hearing and speech outcomes.

In Chapter 3 a landmark set is defined and proposed to include in user-specific 3D computational modelling of the cochlea. The landmarks describe the spiralling nature of the cochlea. A method for the calculation of obscured landmarks that describe the spiralling of the cochlea from references spirals are presented.

Chapter 4 provides recommendations validating the integrity of 3D computational models by using a CSRF. The chapter includes the application of the CSRF on CT scans to test whether the prediction algorithms for the spirals that constitute the cochlear geometry can be applied to images available in a clinical setting.

In Chapter 5 the relation between the anatomical class, spirals and functional outcomes of the cochlea is presented. The chapter investigates which factors contribute to variability in the functional outcomes of the CIs.

In Chapter 6 the findings of the preceding chapters are summarised and discussed in the context of the relevant literature and the research objectives of the thesis. Application of this study in future research is also discussed.

In Chapter 7 a final summary and conclusion of this study are provided.

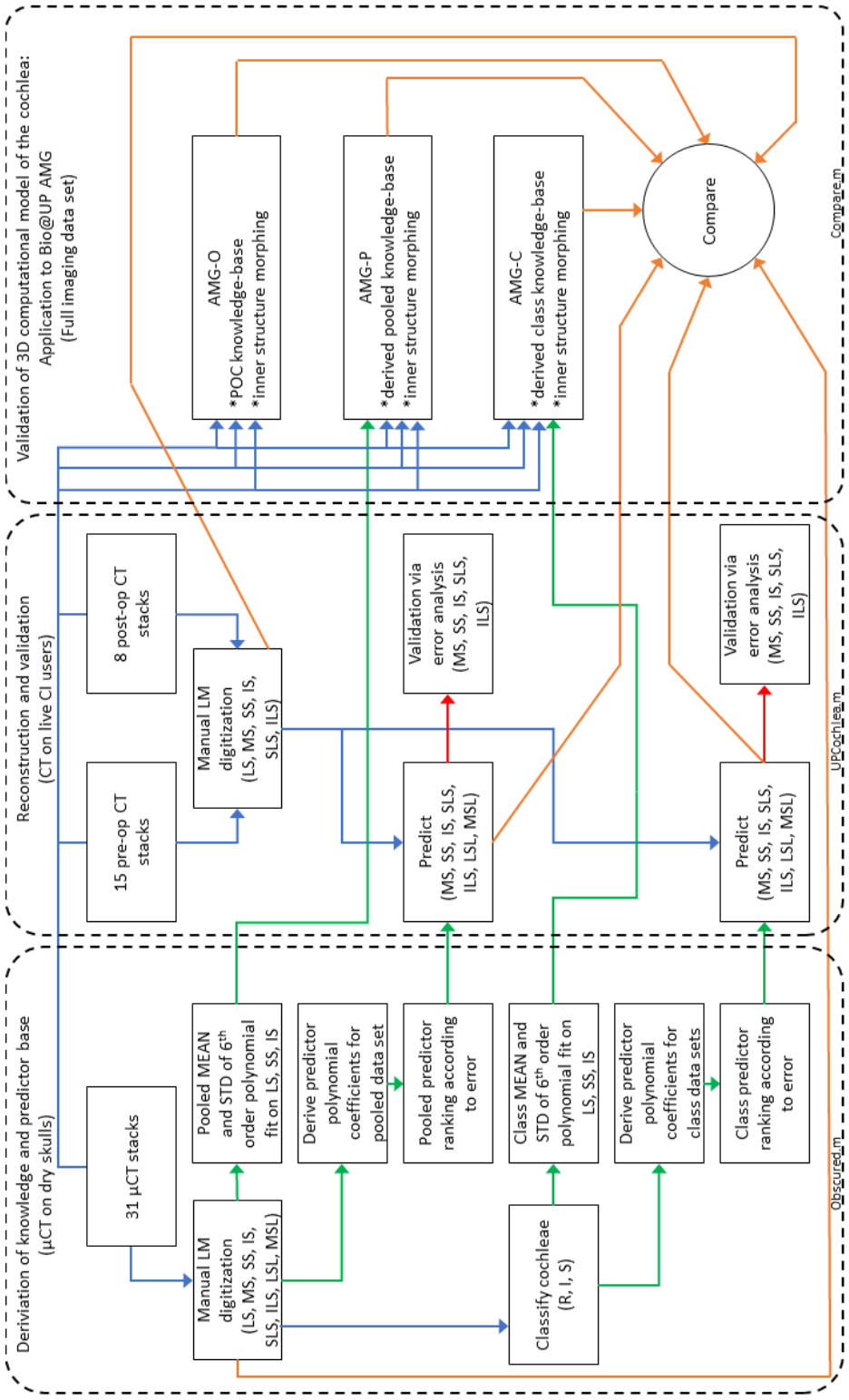

a.)

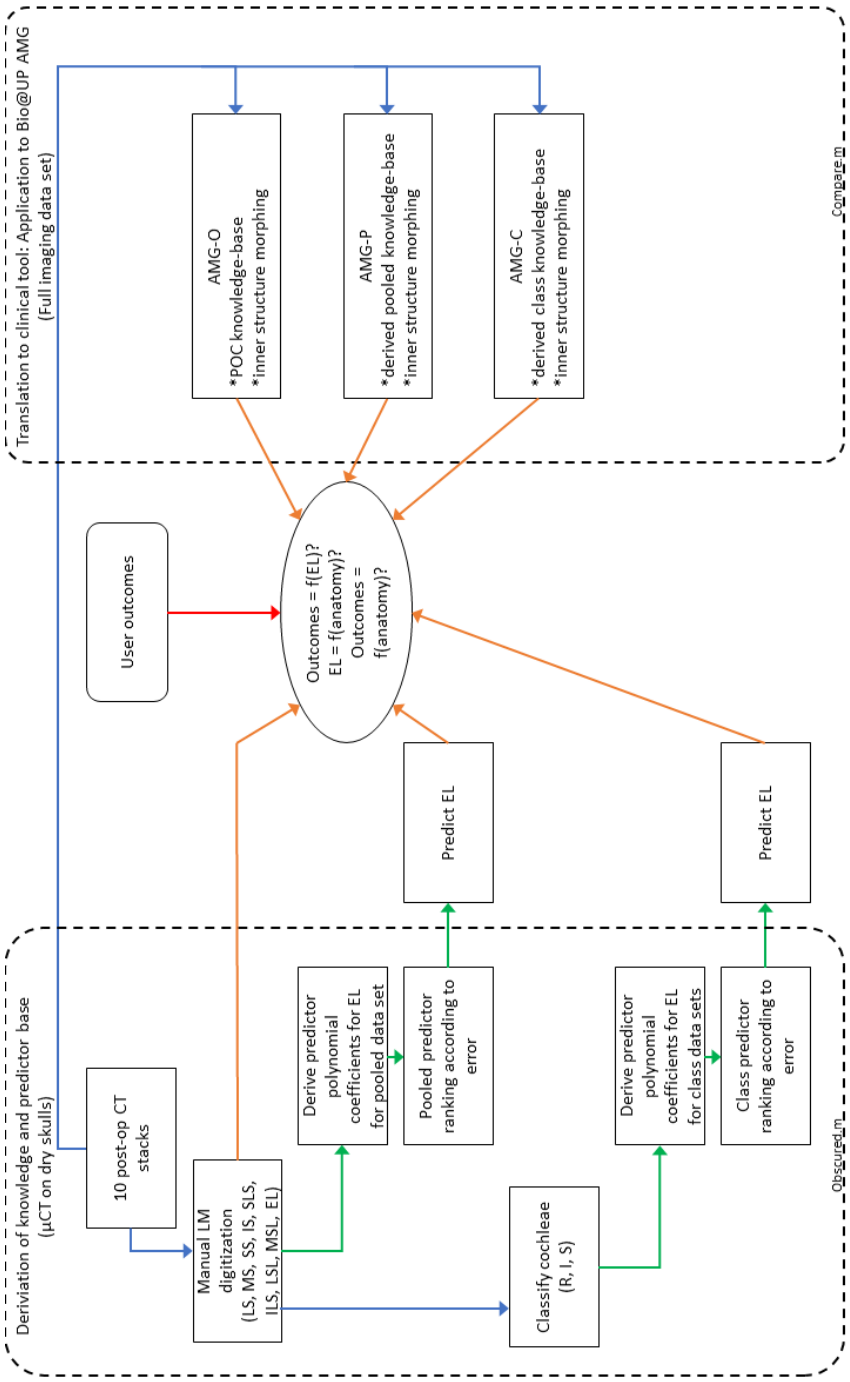

b.)

Figure 1.1 Overview of study. a) Graphical summary of how the CSRF is derived from µCT datasets and validated against CT data and data from an automated model generator (AMG). b) Graphical overview of how the CSRF can be applied to assess the questions in the central oval.

CHAPTER 2 LITERATURE STUDY

CHAPTER OVERVIEW

The objective of this chapter is to provide a foundation for the work presented in this thesis. The chapter comprises a review of the relevant literature, which includes a brief overview in the following sections: 2.2 Human cochlear anatomy, 2.3 Cochlear geometry and variance reported in the literature, 2.4 Methods to assess cochlear geometry variance, 2.5 Imaging in live CI users, 2.6 The origin and role of inter-person variance in CI performance, 2.7 Methods to determine electrode location, 2.8 Modelling in cochlear implantation, 2.9 Cochlear parameters used in modelling in CI, 2.10 Landmark-based methods to measure cochlear parameters, 2.11 Methods to determine obscured landmarks, 2.12 Modiolar correction methods and 2.13 Landmark-based automated computational modelling approaches.

2.1 COCHLEAR ANATOMY

The human inner ear that is involved in the hearing and balance senses, is located within the petrous part (*pars petrosa*) of the temporal bone. The inner ear complex includes the cochlea, vestibule, semicircular canals and membranous labyrinth within a bony labyrinth (Coetzee *et al.*, 2003, Fatterpekar *et al.*, 2006, Meng *et al.*, 2007, Kirk and Gosselin-Ildari, 2009, Gunz *et al.*, 2012, Shin *et al.*, 2013). Perilymph is found within the bony labyrinth that surrounds the membranous labyrinth filled with endolymph (Fatterpekar *et al.*, 2006). Perilymph communicates with the cerebrospinal fluid via the cochlear aqueduct (endolymphatic duct), which can enable the spread of infections between these fluid compartments (Rask-Andersen *et al.*, 2012). The vestibuli and semicircular canals are responsible for balance while the

cochlea is responsible for hearing (Coetzee *et al.*, 2003, Fatterpekar *et al.*, 2006, Drake *et al.*, 2010).

The cochlea is surrounded by the hardest bone in the body, the otic capsule. The compact bone of the otic capsule consists of trilaminar arranged bone with high mineral content and cartilage islands. The specialised bone is responsible for reflecting fluid sound vibrations so that these are not absorbed by the temporal bone. The two mirrored human cochleae are shaped like conical snail shells composed of a bony canal, which twists around a central axis, the modiolus (Coetzee *et al.*, 2003, Fatterpekar *et al.*, 2006, Kirk and Gosselin-Ildari, 2009, Rask-Andersen *et al.*, 2012). The word modiolus is derived from the Latin word 'hub of a wheel' (Coetzee *et al.*, 2003, Kendi *et al.*, 2004a). Usually the bony canals winds around the cone-shaped modiolus 2 ½ times (Coetzee *et al.*, 2003, Kendi *et al.*, 2004b, Fatterpekar *et al.*, 2006) to 2 ¾ times in an anticlockwise direction for left cochleae and a clockwise direction for right cochleae (Kirk and Gosselin-Ildari, 2009), resulting in a basal, middle and apical turn.

The basal turn begins between the oval (OW) and round windows (RW) and ends between the geniculate ganglion and cochleariform process, resulting in the formation of a completely closed ring surrounding two pouches. The medial pouch or cochlear fossa forms part of the fundus of the internal auditory meatus (IAM) while the lateral pouch contains the middle and apical cochlear turns with their smaller radii. The protrusion of the basal turn into the middle ear cavity is overlaid by the bony promontory. This projection is represented by a curved line. The basal turn has a characteristic projection in the horizontal plane where the first portion lying between the OW and RW runs laterally. The basal turn then curves medially to run posterior to the Jacobson's canal or tympanic canaliculus. This portion forms the apex of the promontory, which is the most superficial area of the basal turn (Tóth *et al.*, 2006).

The basal end of the cochlea or cochlear hook is of great surgical importance. At this point it curves in three dimensions, i.e. anterior-posterior, lateral-medial and inferior-superior in three dimensions (Rask-Andersen *et al.*, 2012). Several structural relationships exist in the

hook region. The cochlear duct runs between the stapes footplate and RW. Here the scala tympani (ST) terminates and the scala vestibuli (SV) opens into the vestibule. The saccule of the vestibule is connected to the cochlear region via the *ductus reuniens* (Kirk and Gosselin-Ildari, 2009).

The inner aspect of the cochlea contains the spiral lamina (SL) or osseous spiral lamina (OSL), which projects from the modiolus and twists around the axis of the basal turn. The SL lies almost horizontally near the RW, then coils continuously, after which it turns to lie in the longitudinal plane next to the carotid canal (Tóth *et al.*, 2006). The SL ends in the hook-shaped hamulus at the apex (Fatterpekar *et al.*, 2006). Near the outer edge of the SL, a thickening of the periosteum forms the spiral limbus that is covered with a thin layer of epithelial cells. A vestibular lip is caused by the extension of the upper outer lip of the spiral limbus. An internal spiral sulcus is formed between the vestibular lip and basilar membrane (BM). On the upper surface of the spiral limbus, a membrane called the tectorial membrane (TM) extends over the organ of Corti (OoC). This membrane consists of a gelatinous matrix containing thin keratinised fibres, which are in contact with the microvilli of the hair cells (Coetzee *et al.*, 2003). A second membrane, the Reissner's or vestibular membrane (RM) is found in the cochlear duct. The RM extends from the spiral limbus medially to the outer wall of the cochlear duct laterally. This thin membrane consists of two layers of squamous epithelial cells with a small amount of connective tissue in between. The spiral ligament and stria vascularis are found in the lateral wall of the cochlear duct. A thickening of the connective tissue layer of the periosteum is the cause of the spiral ligament. A groove called the external spiral sulcus is found in the outer wall of the cochlear duct or spiral ligament. Two spiral ridges, the upper *prominentia spiralis* and lower *crista basilaris*, are found on both sides of the external spiral sulcus. The *crista basilaris* serves as attachment site for the BM. The stria vascularis is found just above the *prominentia spiralis* and is responsible for the production of endolymph. The stria vascularis consists of unique specialised epithelium containing capillaries between the epithelial cells (Coetzee *et al.*, 2003).

The SL divides the bony canal into two passages known as the SV and ST (Coetzee *et al.*, 2003, Kendi *et al.*, 2004a, Fatterpekar *et al.*, 2006). The SV and ST communicate through

and opening, the helicotrema which is bounded by the hamulus located at the apex (Fatterpekar *et al.*, 2006, Kirk and Gosselin-Ildari, 2009). The SV and ST contain perilymph (Coetzee *et al.*, 2003, Fatterpekar *et al.*, 2006). The scala media (SM) or cochlear duct which is filled with endolymph, is found between the SV and ST. The SM is separated from the ST below by the BM and from the SV above by the RM (Coetzee *et al.*, 2003, Fatterpekar *et al.*, 2006, Kirk and Gosselin-Ildari, 2009).

The ST is the largest of the compartments (Rebscher *et al.*, 1996), with the round window membrane (RWM) found at the end of it where the hook bends posteromedially (Li *et al.*, 2007, Rask-Andersen *et al.*, 2012). In the area adjacent to the RW, the width and height of the ST are very small. These increase as one moves anteriorly and inferiorly away from the RW. This is the area in which CIs are usually inserted. A cochleostomy is usually performed in the otic capsule anterior to the RWM at the midpoint of its vertical axis. This allows for direct insertion of the electrode array into the ST. This bony area adjacent to the RW is referred to as the anteroinferior margin of the RWM (Li *et al.*, 2007), the *crista fenestra* (Adunka *et al.*, 2004, Briggs *et al.*, 2005, Clark *et al.*, 2012), *crista semilunaris* or *postis anterior* (Proctor *et al.*, 1986).

The RWM is located from the exterior under the tegmen, a bony overhang that is formed by the wall of the promontory. Surgically the RWM is difficult to see, as it is covered by the RW niche and mucosal fold. At first, anatomists thought that the RWM was flat, but later it was found that the membrane is conical in shape with a long and short diameter. It is believed that the RWM plays a larger role than the tympanic membrane in sound transmission (Rask-Andersen *et al.*, 2012). On average the RWM is 2.3 by 1.87 mm in size and does not grow postnatally (Proctor *et al.*, 1986). It has an infero-anterior part that runs vertically and a supero-posterior part that runs horizontally. The membrane lies very close to the SL posteriorly. A small space with a maximal diameter of 2.98 ± 0.23 mm, the *fossula fenestrae rotunda*, is formed by the entrance of the RWM (Sato *et al.*, 1991, Kirk and Gosselin-Ildari, 2009). Important relations of the RWM include the BM, spiral ligament, SM and SL running anteriorly from the posterior margin of the RWM. The inferior cochlear vein and cochlear

aquaduct are related to the inferior margin, while the *ductus reuniens* is closely related to the posterior margin (Li *et al.*, 2007).

The SM or cochlear duct has a triangular appearance when viewed in cross-section. At the bottom of the cochlear duct, the BM extends from the edge of the SL to the outer wall of the cochlear duct. The cochlear duct terminates in the hook region near the posterior edge of the stapes footplate, which coincides with the posterior edge of the RW. The duct is convex in shape in relation to the stapes and lies closest to the footplate in the midline. Anteriorly the duct angles away from the footplate with a narrowing of the ST. The OoC is located within this cavity on the BM and is responsible for converting mechanical sound waves into electrical nerve impulses (Coetzee *et al.*, 2003, Kirk and Gosselin-Ildari, 2009, Rask-Andersen *et al.*, 2012).

The OoC consists of hair cells and supporting cells arranged in a specific manner. The hair cells are the receptor cells, while the support cells surround the hair cells. The first supporting cells encountered are the border cells. These cells are either cuboidal or columnar epithelial cells formed by the epithelial layer covering the spiral limbus. A single row of flask-shaped inner hair cells lies next to the border cells. The inner hair cells contain microvilli on their free surface that are arranged in a C- or U-shape. The microvilli are in contact with the TM. At the bases of the inner hair cells, several nerve endings are present. Another layer of support cells, the inner support or phalangeal cells, surround the inner hair cells. Two rows of uniquely structured support cells, the pillar cells, are present on the outside of the inner supporting cells. The pillar cells have broad bases with long, narrow pillars extending obliquely upwards. The pillars contain longitudinal filaments and microtubules. The free surfaces of the pillar cells come into contact with one another to form a triangular tunnel of Corti. The pillar cells are followed by three to five rows of cylinder-shaped outer hair cells, which rest on supporting cells called Dieter's or outer phalangeal cells. Many microvilli arranged in a Y- or W-pattern are found on the free surface of the outer hair cells. The microvilli come into contact with the TM. Nerve endings are located at the bases of the outer hair cells. The outer hair cells are bordered by tall supporting cells called Hensen's cells. These cells gradually decrease in height until they end at the *crista basilaris*. Here the cells become cuboidal and no longer form part of the OoC and are known as the cells of Claudius.

The cells of Claudius are continuous with the epithelium lining the spiral ligament. The inner hair cells function merely as mechanoreceptors, while the outer hair cells are responsible for registering sound waves (Coetzee *et al.*, 2003, Rask-Andersen *et al.*, 2012).

The bases of the hair cells of the OoC are supported by the BM. The vibration of the BM causes stimulation of the hair cells. The BM is divided into two sections. The thinner *pars arcuata*, which contains blood vessels, extends from the SL to the outer pillar cells. The thicker *pars pectinata* extends to the basilar crest. The BM is composed of transversely arranged bundles of collagenous fibres. In the *pars pectinata* these bundles are known as the auditory cords. These bundles vary from lengths of 65 to 500 µm. The shortest bundles are located closer to the base of the cochlea, while the longer bundles are located closer to the apex. These bundles are tonotopically arranged and responsible for the registration of different frequencies by the cochlea. The longer auditory cords register low frequencies, while the shorter auditory cords register high frequencies (Kirk and Gosselin-Ildari, 2009, Rask-Andersen *et al.*, 2012).

The BM is suspended between the modiolus and anchored at the lateral wall via the spiral ligament. The membrane is narrow and thick at the basal end and becomes thinner and broader towards the apex, making the risk of BM perforation during CI insertion greater with increased insertion depth. The part of the BM between the tunnel of Corti and OSL is perforated (*habenular perforatae*), which allows for the passage of nerve fibres from the OoC (Rask-Andersen *et al.*, 2012). A tubular structure, the spiral ganglion canal or Rosenthal's canal, runs close to the ST inner wall. It parallels the basal turn but terminates in the middle turn. Here the cells that innervate the upper region of the OoC are tightly packed with their peripheral processes running vertically through the thin, apical modiolus (Hochmair *et al.*, 2015).

Figure 2.1 gives a diagrammatic representation of the cochlear anatomy and it's surrounding structures.

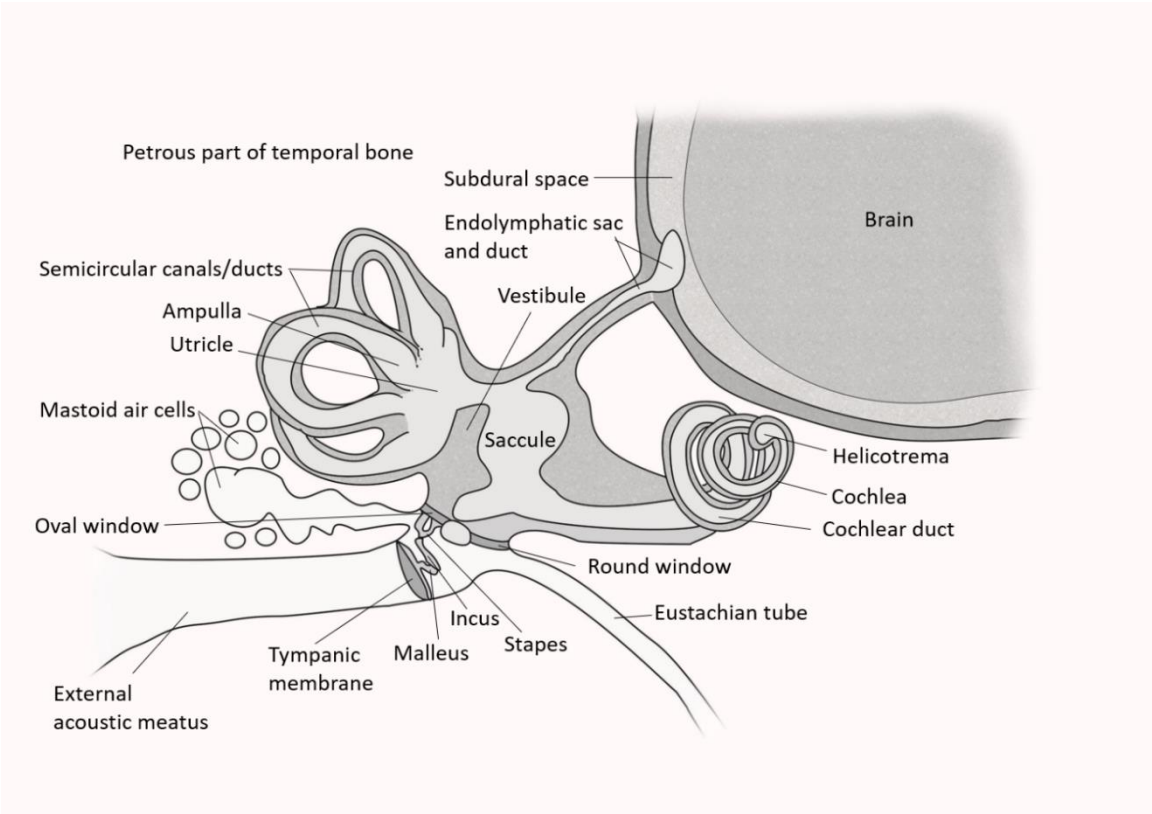

a.)

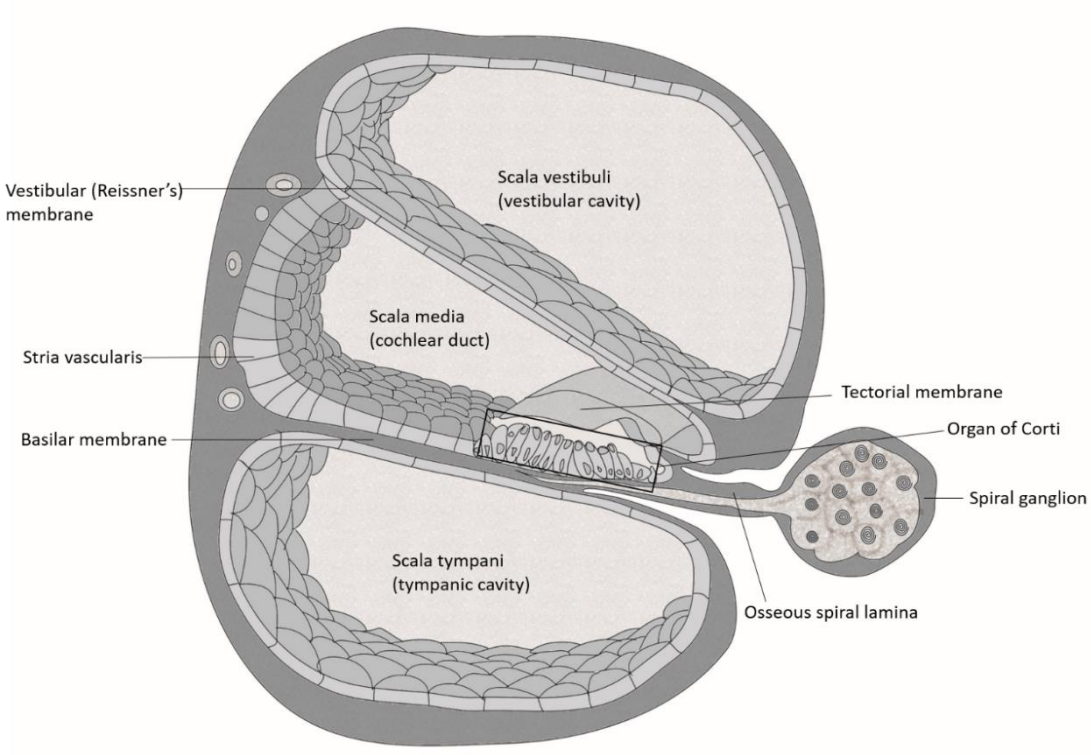

b.)

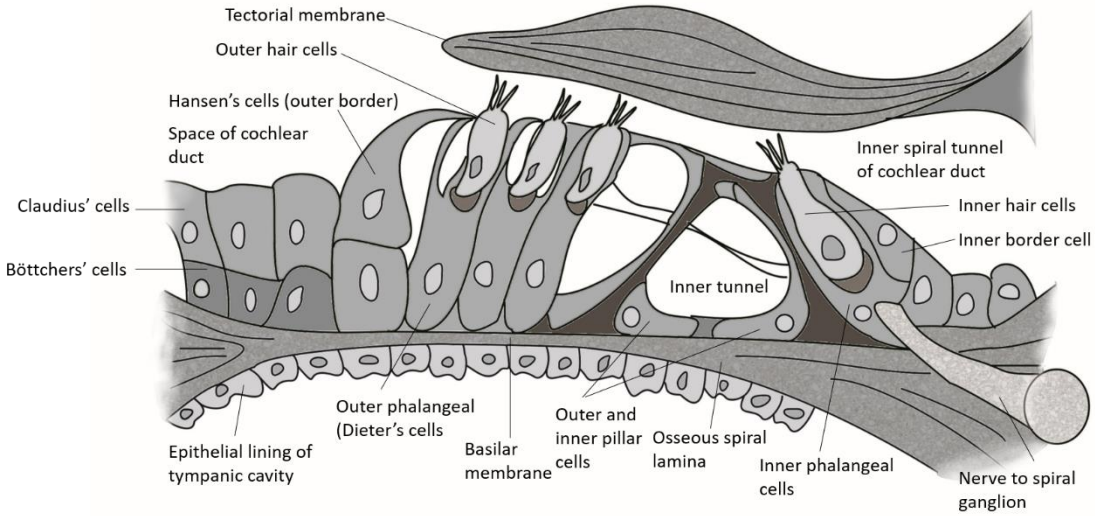

c.)

Figure 2.1. Cochlear anatomy where a.) shows the relationships, connections and labyrinths of the cochlea; b.) is a cross-section through a cochlear turn and c.) shows the histological structure of the organ of Corti

When a sound enters the external acoustic meatus and reaches the tympanic membrane, it moves and causes the auditory ossicles (malleus, incus and stapes) to move hereby converting a sound wave to a mechanical wave. This conversion cause amplification of the wave so that it can enter a dense fluid medium. The stapes is connected to the OW. Movement of the stapes by a sound wave causes the OW to move medially, thereby generating a wave in the perilymph of the SV. This wave moves along the cochlea until it reaches the RW at the lower end of the SV. Sound vibrations are transferred to the cochlear duct, causing vibrations of the BM, and causes stimulation of the underlying hair cells. These stimuli are converted into electrical impulses and conducted by bipolar neurons. The cell bodies of these neurons are located in the spiral ganglion, which is found in the modiolus. The auditory nerve fibres are afferent fibres, which consist of two types of fibres, type I and type II fibres. The thicker type I fibres are those that innervate the inner hair cells, while the

type II fibres are those that innervate the outer hair cells. Both of these fibres leave the OoC through an opening, the *habenula perforata*, as the cochlear nerve (Kendi *et al.*, 2004a, Fatterpekar *et al.*, 2006, Kirk and Gosselin-Ildari, 2009). The dendrites terminate at the bases of the hair cells, while the axons of auditory nerve fibres form the cochlear branch of the vagus nerve (CN IIX) and terminate in the cochlear nucleus in the brainstem (Kendi *et al.*, 2004a, Fatterpekar *et al.*, 2006). The pathway of sound transmission is given in figure 2.2.

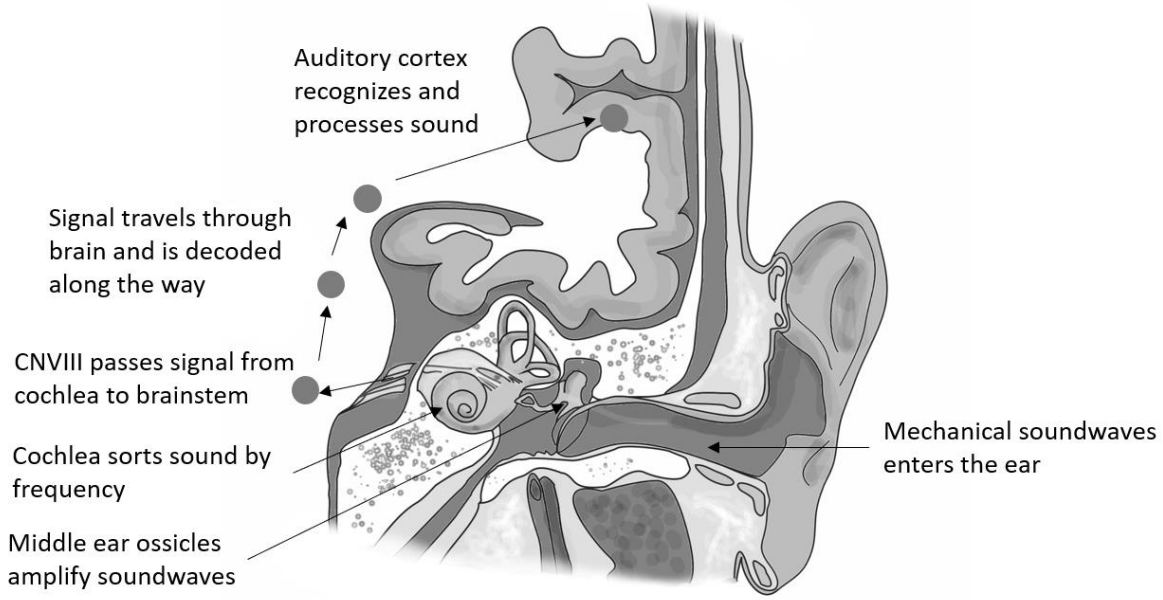

Figure 2.2. Sound transmission and interpretation pathway

CN VIII courses from the inner ear to the brainstem through an opening in the petrous part of the temporal bone, the internal acoustic canal (IAC) or IAM. The facial nerve (CNVII) also courses through the internal acoustic meatus (Fatterpekar *et al.*, 2006). The medial opening of the IAC is known as the *porus acusticus*. The lateral end or fundus is separated from the inner ear by a perforated vertical plate. A horizontal ridge, the falciform crest, divides the fundus into an upper and a lower portion. The upper portion of the fundus is further divided by a vertical plate of bone known as the Bill bar. This results in the formation of an anterior opening for the CNVII and a posterior opening for the superior vestibular

nerve. The lower compartment of the fundus contains openings for the cochlear nerve (Fatterpekar *et al.*, 2006) anteriorly, and the inferior vestibular nerve posteriorly (Kendi *et al.*, 2004a, Fatterpekar *et al.*, 2006). The opening for the cochlear nerve is the largest.

The cochlear nerve terminates at the cochlear nucleus of the pons. The cochlear nucleus receives ipsilateral afferent input. Anatomically the cochlear nucleus is divided into three parts, the antero-ventral cochlear nucleus, the postero-ventral cochlear nucleus and the dorsal cochlear nucleus. Each part has different neural innervation. The antero-ventral cochlear nucleus contains various cells that are sensitive to changes in intensity and frequency of sounds and also processes the changes in the spectral profile of stimuli. The axons of the neurons of the antero-ventral cochlear nucleus leave as a tract, the *ventral acoustic stria*, that travels to the superior olivary complex of the pons. The nuclei of the superior olivary complex receive input from both cochleae. The axons of the nuclei that make up the superior olivary nucleus form a tract called the lateral lemniscus. The lateral lemniscus connects the superior olivary complex to the inferior colliculus of the midbrain. From here the stimulus travels to the ipsilateral thalamus and finally to the auditory area (Coomes Peterson and Schofield, 2007).

Although the anatomy of the cochlea and auditory pathway has been well described, the diverse morphological and physiological properties of auditory pathways (Lee and Sherman, 2011), as well as interindividual variability in the size and shape of the cochlea, among others (Zrunek and Lischka, 1981, Kawano *et al.*, 1996, Wysocki, 1999, Escudé *et al.*, 2006a, Erixon *et al.*, 2009, Biedron *et al.*, 2010, Verbist *et al.*, 2010, Rask-Andersen *et al.*, 2012, Shin *et al.*, 2013, Avci *et al.*, 2014, Van der Marel *et al.*, 2014), carry great clinical and translational significance (Pelliccia *et al.*, 2014).

2.2 COCHLEAR GEOMETRY AND VARIANCE REPORTED IN THE LITERATURE

In the literature, researchers have confirmed the interindividual variability in cochlear geometry. Dimopoulos and Muren (1990) evaluated 95 human cochlea casts of the Swedish

population and found variations in the dimensions of the size and shape of the cochlea. The researchers measured the transverse diameter from the RW to the opposite side (cochlear length), vertical diameter across the basal turn (width of the basal turn) and the axial diameter from the base to the helicotrema (total cochlear height). Ranges were 7.00 to 9.80 mm for the transverse diameter, 6.00 to 7.50 mm for the vertical height and 3.10 to 5.00 mm for the axial height. A positive correlation ($p < 0.05$) between the transverse and vertical diameters were found. When comparing axial height diameters with the transverse and vertical diameters, no correlations were found. The range of variation was not age-dependent.

Cochlear length dimensions on 120 CT scans from a German population reported ranges of 8.10 to 10.40 mm for right cochleae and 8.00 to 10.10 mm for left cochleae. The same study reported a range of 0.90 to 2.20 mm for the height of the basal turn (Krombach *et al.*, 2005). A CT study of 42 cochleae of a French population group reported cochlea lengths of 9.23 ± 0.53 mm, widths of the basal turn of 6.99 ± 0.37 mm and outer wall lengths of 34.40 ± 2.20 mm (Escudé *et al.*, 2006a). A Filipino study reported smaller cochlear lengths of 7.55 mm for right cochleae and 7.60 mm for left cochlea; however, the total cochlear heights were larger when compared to other studies (4.36 for right cochleae and 4.34 for left cochleae, showing that cochleae with shorter bases and lengths have a total cochlear height (Fernando *et al.*, 2011).

Erixon *et al.* (2009) studied 73 corrosion casts and found significant variations in the dimensions and coiling characteristics in different cochleae. Figure 2.3 provides a summary of the findings from the Erixon study. The relative scale of the figures in terms of angular degrees, total height and width of the first turn is approximately correct to provide an appreciation for the observed dimensional variations. On average (the mean representation in Figure 2.2) the lengths of the first, second and third turns account for approximately 53%, 30% and 17% of total cochlear length respectively. The study also evaluated the number of turns, RW diameter and the width and height of each turn. The authors found that each cochlea was individually shaped, with large variations in the dimensions and coiling characteristics. Variable coiling patterns had an influence on the shape of the first turn. If the coiling started more distally, the basal part of the first turn was straighter, but if the coiling pattern started more proximally the basal turn was shorter and the cochlea more compressed.

In some cochleae, the various turns appeared to be tilted around the central axis. The half diameter of the RW ranged from 0.3 to 1.6 mm (n=65). The length of the first, second and third turns ranged from 20.3 to 24.3 mm (n=65), 10.7 to 13.3 mm (n=63) and 1.5 to 8.2 mm (n=58) respectively, with the total length ranging from 38.6 to 45.6 mm (N=58). The height of each turn ranged from 1.6 to 2.6 mm (n=73) for the first turn, 0.8 to 1.6 mm (n=67) for the second turn, 0.3 to 1.1 mm (n=60) for the third turn and 3.3 to 4.8 mm (n=60) for the total height. The width of the first turn ranged from 5.6 to 8.2 mm (n=71), that of the second turn ranged from 3.3 to 4.3 mm (n=68) and that of the third turn ranged from 0.6 to 3.6 mm (n=60). Differences of up to 7 mm in the length of the outer cochlear wall were also found.

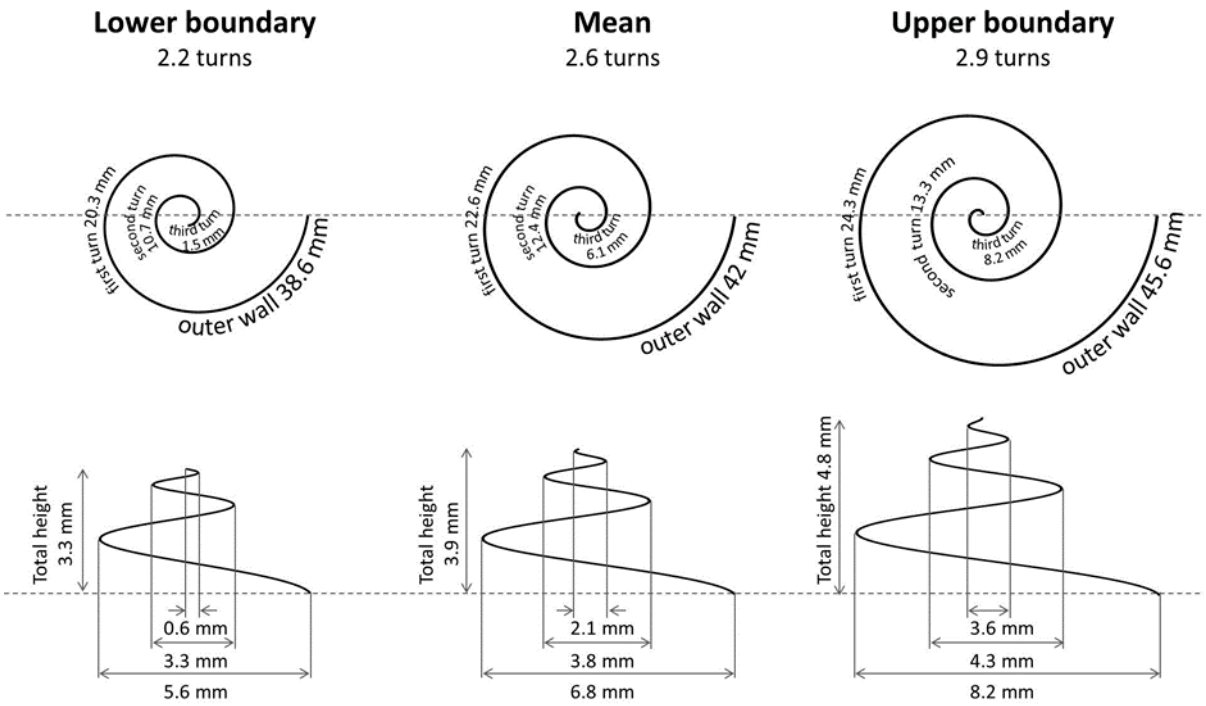

Figure 2.3. Schematic representation of the variation in cochlear dimensions found by Erixon, Högstorp *et al.* (2009). The cochlear height, width of the first turn and number of turns are approximately to scale relative to one another to provide a visual illustration of the range of measured values.

Morphometric studies by Martinez-Monedero *et al.* (2011) using 124 CT scans of CI candidates of an American population showed considerable variability with regard to the cochlear length (range 6.8 to 10.3 mm) and width of the base (range 5.2 to 7.8 mm), angle

between the first and second turns (range 7.1^0 to 22.5^0) and cochlear orientation. The diameter of the modiolar inlet diameter of normal cochleae ranged from 3.42 to 3.82 mm. Measurement of cochlear length on six cadaver cochleae using magnetic resonance imaging (MRI) varied from 17 to 26.5 mm (Pochini Sobrinho *et al.*, 2009).

When µCT scanning became more freely available, a study on one temporal bone reported measurements of 7.70 mm for the width of the basal turn, 4.35 mm for the width of the middle turn, 2.84 mm for the width of the apical turn, 4.06 mm for the total cochlear height, 1.90 for the height of the basal turn, 1.30 mm for the height of the middle turn and 0.80 mm for the height of the apical turn (Braun *et al.*, 2012). Shin *et al.* (2013) reported the mean cochlear length of a Korean sample as 9.70 mm, width of the basal turn as 7.00 mm, width of the middle turn as 3.90 mm, total cochlea height as 3.80 mm, height of the basal turn as 1.90 mm, height of the middle turn as 1.80 mm and height of the apical turn as 0.70 mm. A German research group conducted two studies in 2014 and in 2017 on µCT scans of fresh frozen temporal bones. Mean cochlear lengths were 9.20 ± 0.40 mm and 9.35 ± 0.31 mm, respectively. The widths of the basal turn were 7.00 ± 0.30 mm and 7.04 ± 0.34 mm (Avci *et al.*, 2014, Avci *et al.*, 2017). A 3D analytical model of cochlear casts and µCT scans of German origin found cochlea lengths of 9.30 ± 0.30 mm for the casts and 9.20 ± 0.40 mm for the µCT scans, basal urn widths of 7.00 ± 0.30 and 6.80 ± 0.40 mm, total cochlear heights of 4.40 ± 0.40 mm and 4.00 ± 0.20 mm. The researchers defined outer wall length as the metric length of the cochlea, which ranged from 36.00 to 46.00 mm (Pietsch *et al.*, 2017). Mean metric lengths have long been reported as 38.64 ± 3.19 mm (Sato *et al.*, 1991), 40.81 ± 1.97 mm (Kawano *et al.*, 1996), 41.20 ± 1.86 mm (Erixon and Rask-Andersen, 2013) and 37.90 ± 1.98 mm (Wurfel *et al.*, 2014).

The number of cochlear turns or angular length (AL) may influence the location and insertion angle of the CI array, which in turn may influence the alignment of the array to the intended neural stimulation sites (Biedron *et al.*, 2009). Variance in the number of turns of the cochlea, determined by measurements of histologic sections, cochlear casts, CT images and µCT images, has intermittently been reported in the literature (Hardy, 1938, Takagi and Sando, 1989, Kawano *et al.*, 1996, Tian *et al.*, 2006, Biedron *et al.*, 2009, Erixon *et al.*, 2009, Shin

et al., 2013). There seems to be little agreement on the basic question concerning the number of cochlear turns. In a detailed study by Biedron *et al.* (2009) more than 2.5 turns were found in 65% of cases analysed. Other studies have mentioned the number of turns only as side information without taking the frequency of variations into account (Hardy, 1938, Kawano *et al.*, 1996, Tian *et al.*, 2006). Shin *et al.* (2013) found the mean number of cochlear turns to be 2.54, with a range from 2.36 to 2.8 turns. Tian *et al.* (2006) reported three cases of cochleae with three turns; these cochleae were longer, with a longer BM. Different methods have been used to determine the number of cochlear turns. Biedron *et al.* (2009) counted the number of segments present on mid-modiolar histological sections. In 54 to 74% of cases (n = 157), more than 2½ but fewer than 2¾ turns were found. Hardy (1938) used the same method and found more than 2½ turns in 74% of cases. Three-dimensional reconstruction was used to count the number of turns by Kawano *et al.* (1996), who found 2.63 turns in 71% of instances. Erixon *et al.* (2009) divided cochlear casts into quadrants and the number of quadrants was counted to determine the number of turns. The researchers reported a mean of 2.6 turns for the cochlear casts.

Shin *et al.* (2013) used 3D reconstructions of µCT images to determine the angle between the starting line of the cochlea and another line from the central axis of the cochlea to the terminal point of the apical turn. The mean number of turns was found to be 2.54 ± 0.09. Fernando *et al.* (2011) found 2.5 turns in 92.3% of cases by determining the number of quadrants present on the 3D reconstruction of CT scans. Tian *et al.* (2006) reported the incidence of more than three cochlear turns in three cases by counting the number of segments present on mid-modiolar histological sections. In a study by Pietsch *et al.* (2017) on the spatial form of the human cochlea, the number of turns was defined as angular length (AL). The authors expressed AL in degrees, with means of 965.00 ± 40.00º for cochlear casts and 967.00 ± 45.00º for µCT scans of human cochleae.

The size and shape of the ST are especially important with regard to the final position of the intracochlear array and the probability of insertion damage (Rebscher *et al.*, 2008). In a study conducted by Biedron *et al.* (2010) the cross-sectional diameter of the ST varied significantly among individuals (n=20). Several researchers report dimensional variations of the ST (Zrunek *et al.*, 1980, Zrunek and Lischka, 1981, Walby, 1985, Rebscher *et al.*, 1996,

Wysocki, 1999, Rebscher *et al.*, 2008). Research measuring the cross-sectional diameter of the ST shows that the ST also tapers from the RW to the helicotrema, but that this is not a continuous phenomenon and may show enlargements in some places, leading to even more variation and unconformity (Zrunek *et al.*, 1980, Zrunek and Lischka, 1981). Measurements of the inner wall length of the ST ranged from 15 to 18.3 mm (n=5) (Johnson *et al.*, 2012) and outer wall length ranged from 32.94 to 36.57 mm (n=26) (Skinner *et al.*, 2002). Estimation of ST volume using MRI shows a range of 172.3 to 272.6 mm^3 (Melhem *et al.*, 1998).

The hook region is of special interest. Researchers such as Gibson *et al.* (2012) have noted inter-subject variability regarding the basal turn of the cochlea, cochlear hook region and rotation and orientation of the SL, using high-resolution MRI. Sites inferiorly from the cochleostomy site (hook region) showed the greatest variation, with sharp rotations of the OSL near the hook region and tapering of the cross-sectional area of the ST, resulting in a high-risk region for insertion trauma. Angular rotation of the OSL relative to the vertical axis along the basal turn ranged from 17^0 to 55^0 for the right cochlea and 14^0 to 30^0 for the left (Gibson *et al.*, 2012).

As most of the current spreads via the ST and across the turns before leaving the cochlea through the modiolus, variance in the modiolar dimensions should be noted (Micco and Richter, 2006). Lemmerling *et al.* (1997) found that normal variations of the modiolus are a constant feature. Area and volume measurements of the modiolus have been evaluated using MRI, but researchers did not investigate variations among subjects (Naganawa *et al.*, 1999).

Variations in cochlear morphology may influence the introduction and location of the electrode array into the cochlea and the patterns of electric fields that are generated to stimulate target neurons in the CI user (Ketten *et al.*, 1998, Lane *et al.*, 2007, Rebscher *et al.*, 2008, Martinez-Monedero *et al.*, 2011), limit potential hearing preservation or cause significant surgical trauma (Adunka *et al.*, 2004, Wardrop *et al.*, 2005, Erixon *et al.*, 2009, Biedron *et al.*, 2010, Pelliccia *et al.*, 2014, Avci *et al.*, 2017). In addition, cognisance of these variations is important for the creation of 3D volume conduction computational models that

predict the electrical properties of the implanted cochleae (Frijns *et al.*, 1995, Frijns *et al.*, 2000, Yoo *et al.*, 2000, Briaire and Frijns, 2000b, Hanekom, 2001, Yifang and Collins, 2005, Poznyakovskiy *et al.*, 2008, Malherbe, 2009, Braun *et al.*, 2012, Malherbe *et al.*, 2013, Hanekom and Hanekom, 2016, Kalkman *et al.*, 2016, Nogueira *et al.*, 2016, Seeber and Bruce, 2016), manufacturing and selection of CIs (Balkany *et al.*, 2002, Rebscher *et al.*, 2007, Rebscher *et al.*, 2008, Eshraghi *et al.*, 2012, Brant and Ruckenstein, 2016, Aschendorff *et al.*, 2017, Dhanasingh and Jolly, 2017) and surgical planning before CI (Tóth *et al.*, 2006, Pelliccia *et al.*, 2014).

All of the cochlear variations were studied using several techniques, each with its own advantages and disadvantages. These techniques are discussed in the following section.

2.3 METHODS TO ASSESS COCHLEAR GEOMETRY VARIANCE

The cochlea is a small structure embedded within the dense otic capsule, and obtaining accurate geometric and morphological data is a challenge (Fatterpekar *et al.*, 2006). To assess cochlear variations and obtain the geometrical data needed for the construction of person-specific models and the estimation of the locations of the electrodes, several techniques have been used. These include casting, dissection, histological sectioning, videofluoroscopy, µCT imaging, cone-beam computed tomography (CBCT), magnetic resonance microscopy (MRM or µMR), CT and MRI.

Cochlear casts are made using several materials such as metal alloys and plastic. The casts are photographed and gross measurements are taken with a calliper. The casts allow for the evaluation of gross morphological variations (Dimopoulos and Muren, 1990, Erixon *et al.*, 2009) and are valuable, as they provide a method to visualise the insertion path and position of the electrode array *in situ* (Rebscher *et al.*, 1996). The disadvantages of this method are that it is very time-consuming and small integrate structures cannot be delineated; shrinkage of the cochlea has been reported when casting methods are used.

Physical dissection can be used to investigate the integrate anatomy of the cochlea. Precise data for use in surgical cochlear implantation can be obtained and the rotation of the SL can

be determined (Tóth *et al.*, 2006). Small, fragile structures such as the RM cannot be measured, as they are damaged during dissection and are too small to view with the naked eye (Fernández, 1952).

Histological sectioning provides detailed information on the soft tissue structures of the cochlea. The temporal bone is decalcified, dehydrated, embedded, sectioned and stained. The sections are viewed using light microscopy and digitised into a workstation connected to the light microscope. The method provides excellent visualisation of the cochlear fine structures. However, the process is destructive and the dehydration process causes the cochlear structures to shrink, providing inaccurate parametric data. Histological sectioning of cadaver temporal bones after electrode implantation provides information on electrode position (Frijns *et al.*, 2001b) and the degree of insertion trauma (Rebscher *et al.*, 2008).

MRM or µMRI renders images with a voxel size of 25 µm. It is an excellent imaging method for the quantification of the cochlear fluid spaces and delineation of small structures (Salt *et al.*, 1995, Thorne *et al.*, 1999). µCT imaging provides high resolution that enables the visualisation of the fine bony labyrinth. Poznyakovskiy *et al.* (2011) used µCT with a resolution of 8.41 µm. µCT imaging with a voxel size of 0.062 to 0.109 mm^3 has been applied in a semi-landmark 3D geomorphometric approach to shape analysis to study the phylogeny of different species by Gunz *et al.* (2012). µCT images of human temporal bones have added value to the investigation of cochlear anatomy and electrode behaviour, as the high-resolution technique can delineate fine cochlear structures not visible in lower resolution studies (Postnov *et al.*, 2006, Poznyakovskiy *et al.*, 2008{Adunka, 2004 #121, Braun *et al.*, 2012, Shin *et al.*, 2013, Avci *et al.*, 2014, Van der Marel *et al.*, 2014, Avci *et al.*, 2017, Pietsch *et al.*, 2017).

Although µCT, µMRI and histology provide an accurate methodology, they are not always practical or possible (Gunz *et al.*, 2012). These techniques are not viable for *in vivo* measurements of cochlear structures. CT and MRI are much faster and widely acceptable alternatives, as long as reduced image quality is taken into account (Gunz *et al.*, 2012).

Medical CT of the cochlea is a widely accepted technique. It is used for the detection and quantification of variations in cochlear anatomy, 3D reconstructions of the cochlea, geometric modelling and postoperatively to assess implant placement and electrode position (Ketten *et al.*, 1998, Skinner *et al.*, 2002, Fatterpekar *et al.*, 2006, Connor *et al.*, 2009, Martinez-Monedero *et al.*, 2011, Connor *et al.*, 2012). Cochlear structures that can be delineated with CT include the bony labyrinth, OSL and modiolus (Martinez-Monedero *et al.*, 2011).

When using imaging techniques, the cochlea is orientated in a manner called the cochlear view. The cochlear view was developed to determine the electrode position postoperatively by measuring the longitudinal and angular positions of the electrodes on radiographic images (Cohen *et al.*, 1996, Xu *et al.*, 2000). Many modifications of this view exist, but all are based on the method described by researchers (Cohen *et al.*, 1996, Xu *et al.*, 2000, Verbist *et al.*, 2009, Verbist *et al.*, 2010). Reconstructions of the images are performed through software, which converts the raw projections into tiff image stacks of two-dimensional (2D) cross-sections for each sample cochlea. The slices are then stacked to produce a virtual voxel volume that represents the sample in three dimensions. Software is used for the rendering, segmentation and visualisation of the reconstructed data. Distances can then be measured by integrating the information provided by the 3D image in the orthogonal planes (Johnson *et al.*, 2012). In accordance with international consensus, all cochlear measurements should take place on the coordinate system, as described by Verbist *et al.* (2010).

In the 3D coordinate system, the basal turn of the cochlea is used as the x- and y-axes and the centre of the modiolus as the z-axis. The 0^0-landmark is defined as the most lateral point of the horizontal semicircular canal. Reference lines can be drawn using this coordinate system. According to this method, the RW lies on a reference line that passes through the centre of the spiral at an angle of 10^0 to the horizontal plane (x-axis) (Biedron *et al.*, 2010). Using this method, all positions in the cochlear spiral can be described by using the reference line drawn through the beginning of the RW and the centre of the cochlear spiral (Biedron *et al.*, 2009, Biedron *et al.*, 2010, Verbist *et al.*, 2010, Johnson *et al.*, 2012). This method is in line with cochleostomy surgery as performed at the RWM (Adunka *et al.*, 2007).

2.4 HUMAN COCHLEAR TAXONOMY

Variation in cochlear size and shape has prompted researchers to classify cochleae according to the length of the ST and the total height of the cochlea. This is done by unrolling the ST and plotting the z-coordinates of the largest diameter of the ST (height) against the lateral wall distance of the cochlea, in other words, the height of the cochlea relative to the cochlea versus angular position. A cochlea is defined as having a rollercoaster, sloping or intermediate profile according to three critical anatomical features in the ST profile. A rollercoaster profile presents with a dip seen as a local minimum, followed by an increase in the vertical trajectory before the end of the first turn. A peak, seen as a local maximum followed by a vertical jump before the end of the first turn, defines a sloping profile. Cochleae with an intermediate ST profile present with a vertical jump (sudden increase in the vertical trajectory of the ST), followed by a dip before the end of the first turn (Avci *et al.*, 2014, Demarcy *et al.*, 2016, Pietsch *et al.*, 2017).

2.5 IMAGING IN LIVE PATIENTS

Computed tomography provides images of both the implanted array and the cochlea and has the advantage of providing aligned, sectional data that facilitate 3D reconstruction and cochlear measurements. Spiral CT provides better longitudinal resolution and allows retrospective slice reconstruction at multiple thicknesses from a single CT data set. Cochlear and array details can be measured rapidly *in vivo* at a resolution sufficient for calculating individual frequency distributions (Ketten *et al.*, 1998). Cochlear structures that can be delineated with CT include the bony labyrinth, SL and modiolus (Martinez-Monedero *et al.*, 2011). Computed tomography measures include cochlear size variability (Pelliccia *et al.*, 2014), cochlear length (Krombach *et al.*, 2005, Escudé *et al.*, 2006b, Connor *et al.*, 2009, Martinez-Monedero *et al.*, 2011), mean transverse diameter or width of the basal turn (Escudé *et al.*, 2006a, Martinez-Monedero *et al.*, 2011), total cochlear height and height of the basal turn (Krombach *et al.*, 2005).

Magnetic resonance imaging is a useful tool to investigate the intra-cochlear fine structure, as it provides improved image resolution at higher field strengths and has extended multi-planar imaging capabilities (Gibson *et al.*, 2012). Magnetic resonance imaging of the inner ear provides a non-invasive demonstration of the structures of the inner ear and cochlea pre-operatively. The modiolus is seen as a low signal intensity structure (Naganawa *et al.*, 1999, Ludman, 2000). Perilymph of the ST can be distinguished separated from perilymph and endolymph within the SV and SM by the low signal of the bony spiral lamina. These fluid-filled spaces have a bright signal that can be extracted and their length and volume can be calculated (Melhem *et al.*, 1998). Bony structures such as the SL appear as a small line in cochlear turns (Arnold *et al.*, 1996) with little signal. MRI is practical and efficacious in gathering pre-operative data from large populations without a radiation penalty (Gibson *et al.*, 2012). Another advantage is the ability to apply virtual endoscopic techniques to MRI data, enabling examination of the normal anatomy of the inner ear (Dimopoulos and Muren, 1990).

Anatomically based MRI studies can establish normative values for these variations derived from a large population (Gibson *et al.*, 2012). Magnetic resonance imaging is used to determine modiolar area and volume (Naganawa *et al.*, 1999, Kendi *et al.*, 2004a) and volume of labyrinth (Kendi *et al.*, 2004a), cochlear nerve preservation (Ketten *et al.*, 1998, Lane *et al.*, 2007), inner ear volumetric measurements (Melhem *et al.*, 1998, Neri *et al.*, 2000) and length of the cochlea (Pochini Sobrinho *et al.*, 2009).

Recently a high-resolution method CBCT has been used to assess cochlear length in a clinical setting (Wurfel *et al.*, 2014). Cone beam computed tomography provides a significantly lower radiation dose and increased spatial relationship when compared to CT (Vaid and Vaid, 2014). Cone beam computed tomography is a low-dose technique with fewer artefacts in postoperative imaging (Ruivo *et al.*, 2009).

Preoperative imaging modalities aid in diagnosing inner ear malformations, development of normative values, assessment of cochlear anatomy, delineation of surgical access and pathology using CT (Arnold *et al.*, 1996, Nair *et al.*, 2000, Veillon *et al.*, 2001, Rodt *et al.*,

2002b, Gleeson *et al.*, 2003, Purcell *et al.*, 2003, Karino *et al.*, 2004, Krombach *et al.*, 2005, Chaturvedi *et al.*, 2006, Fatterpekar *et al.*, 2006, Lutz *et al.*, 2007, Fishman, 2012, Vaid and Vaid, 2014, Taha *et al.*, 2015) and MRI (Arnold *et al.*, 1996, Held *et al.*, 1997, Davidson *et al.*, 1999, Diamantopoulos *et al.*, 1999, Hans *et al.*, 1999, Ludman, 2000, Schick *et al.*, 2001, Veillon *et al.*, 2001, Gleeson *et al.*, 2003, Chaturvedi *et al.*, 2006, Ishida *et al.*, 2007, Meng *et al.*, 2007, Fishman, 2012, Taha *et al.*, 2015). Magnetic resonance imaging is used especially for evaluating the luminal ossification and inner ear patency before CI (Murugasu *et al.*, 1999, Seitz *et al.*, 2001, Chaturvedi *et al.*, 2006, Fishman, 2012, Vaid and Vaid, 2014, Taha *et al.*, 2015).

Postoperative evaluation of CI is used to establish electrode position using radiography and CT (Ketten, 1994, Cohen *et al.*, 1996, Ketten *et al.*, 1998, Lawson *et al.*, 1998, Gstoettner *et al.*, 1999, Xu *et al.*, 2000, Skinner *et al.*, 2002, Bettman *et al.*, 2003, Copeland *et al.*, 2004, Verbist *et al.*, 2005, Wardrop *et al.*, 2005, Escudé *et al.*, 2006a, van Wermeskerken *et al.*, 2007, van Wermeskerken *et al.*, 2009, Verbist *et al.*, 2010, Zaghloul *et al.*, 2011, Connor *et al.*, 2012, Kong *et al.*, 2012, Van der Marel *et al.*, 2014) and advancement of electrode array during CI (Huttenbrink *et al.*, 2002). Recently CBCT has been used as a postoperative method (Zou *et al.*, 2015a).

Many authors compare different types of imaging modalities in radiological diagnostics (Sennaroglu *et al.*, 2002, Jäger *et al.*, 2005, Chaturvedi *et al.*, 2006) and co-register imaging modalities (Neri *et al.*, 2000). However, studies comparing the accuracy with which cochlear landmarks are visible on low-resolution versus high-resolution data are lacking. A method to quantify the effect of low-resolution scanning, such as blurriness and a low signal-to-noise ratio and the effect of a soft tissue interface, is needed when planning CI.

2.6 THE ORIGIN AND ROLE OF INTERPERSON VARIANCE IN CI PERFORMANCE

Patients suffering from sensorineural hearing loss have distorted sound perception, resulting in a reduction in sensitivity, development of intensity sensation, reduction in frequency selection, and reduction in the temporal resolution of sound (Oxenham and Bacon, 2003). From the literature, it is clear that variability in speech and auditory performance has been attributed to the characteristics of the peripheral and central auditory systems, resulting from the impact of sensorineural hearing loss on the afferent neural structures (Tong *et al.*, 1988, Summerfield and Marshall, 1995, Blamey *et al.*, 1996, Rubinstein *et al.*, 1999, Leung *et al.*, 2005, Finley *et al.*, 2008, Wanna *et al.*, 2011, Meneses *et al.*, 2014). Identification of the mechanisms responsible for this wide range of performance could lead to directed efforts at overcoming the fundamental factors limiting speech reception and performance (Khan *et al.*, 2005).

Mapping or programming of the CI helps to optimise the CI user's access to sound by adjusting the current input to the electrodes on the array that is implanted into the cochlea. Several psychophysical precepts are measured to determine device performance and patient outcomes, and to validate computational models of the cochlea (Khan *et al.*, 2005, Yifang and Collins, 2005, Cohen, 2009, Nicoletti *et al.*, 2013). The softest sounds the user can detect, or threshold (T-levels), and the loudness levels, or comfort level (C- or M-level), for each electrode is set according to the levels tolerable for the user. These are expressed as numeric values that designate the amount of current delivered by each electrode. The dynamic range (DR) for each electrode is derived from the T- and C-values. The psychophysical parameters T-level, maximum C-level and DR are correlated to speech perception ability (Blamey *et al.*, 1996), and to each other (Kawano *et al.*, 1998). T- and C-levels increase or decrease in parallel, with DR being more closely related to C-levels than to T-levels (Kawano *et al.*, 1998). These need to be optimised for speech and hearing perception. As with all surgical processes, fibrous or scar tissue is a natural physiological process that occurs around the electrode contacts. This process causes a change in the resistive properties around the electrode contact, known as impedance. Increased impedance

over time after CI has been reported to cause an increase in electrode modiolar distance (Tykocinski *et al.*, 2001, Husstedt, 2002, Cohen *et al.*, 2006, Micco and Richter, 2006, Malherbe *et al.*, 2015), which in turn will affect the excitation profile of the auditory neurons (Malherbe *et al.*, 2015). Higher resistivities of the surrounding bone structures shield a larger component of the stimulating current into the lower resistivities' cochlear spread, causing wider spread, while lower resistivities allow more current to leak from the cochlear structures, with resulting narrower current spread, a narrower electric field and neural excitation processes (Micco and Richter, 2006, Malherbe *et al.*, 2015).

Objective and psychometric measures illustrate that there is considerable variability in the auditory performance of CI users (Meneses *et al.*, 2014), which has been noted in both speech and non-speech sounds (Peterson *et al.*, 2010). This has been attributed to the characteristics of the peripheral and central auditory systems, resulting from the impact of sensorineural hearing loss on the afferent neural structures (Tong *et al.*, 1988, Summerfield and Marshall, 1995, Blamey *et al.*, 1996, Rubinstein *et al.*, 1999, Leung *et al.*, 2005, Finley *et al.*, 2008, Wanna *et al.*, 2011, Meneses *et al.*, 2014).

Variation in performance has been found since the implantation of the earliest CI devices, and has persisted in the newer generations of CIs, even when using similar devices. Such variability between CI users makes predicting individual outcomes very difficult (Peterson *et al.*, 2010), and has prompted many investigations into the reasons why variations exist, in the hope of finding possible solutions to improve hearing restoration optimally (Khan *et al.*, 2005). Factors such as unusual or variable cochlear anatomy, insertion depth of the electrode array, proximity of the array to the modiolus and atraumatic insertion of the array may influence electrode introduction and electrode location and ultimately the performance of the CI at the peripheral neural electrode interface (Briggs *et al.*, 2005, Rebscher *et al.*, 2008, Erixon *et al.*, 2009, Martinez-Monedero *et al.*, 2011, Gibson *et al.*, 2012)

Although not all factors leading to hearing loss or undesirable outcomes are known, the extensive anatomic variations of cochlear anatomy are most likely to play an important role (Erixon *et al.*, 2009). Of these factors, the anatomical inter-individual variations are a

fundamental reason for the great variability in outcomes seen with CI surgery (Skinner *et al.*, 2002, Escudé *et al.*, 2006a, Erixon *et al.*, 2009, Biedron *et al.*, 2010, Martinez-Monedero *et al.*, 2011, Braun *et al.*, 2012, Eshraghi *et al.*, 2012, Shin *et al.*, 2013, Malherbe *et al.*, 2015, Malherbe *et al.*, 2016, Avci *et al.*, 2017). Variations in cochlear anatomy have been widely reported by many researchers (Dimopoulos and Muren, 1990, Ketten *et al.*, 1998, Escudé *et al.*, 2006a, Erixon *et al.*, 2009, Biedron *et al.*, 2010, Martinez-Monedero *et al.*, 2011, Avci *et al.*, 2014, Van der Marel *et al.*, 2014, Wurfel *et al.*, 2014). These variations have important consequences for CI surgery, as individual variations ideally need to be addressed both pre- and postoperatively, to ensure the best possible hearing outcome for the patient (Khan *et al.*, 2005). These cochlear variations influence the location of CI arrays and affect the potential of hearing preservation surgery and in turn the speech and hearing outcomes (Rubinstein *et al.*, 1999, Adunka *et al.*, 2004, Gstoettner *et al.*, 2004, Cosetti and Waltzman, 2012, Zohdi *et al.*, 2014, Brant and Ruckenstein, 2016, Khoza-Shangase and Gautschi-Mills, 2019). This is intuitive when it is realised that the exact location of the electrode contacts within the cochlea dictates the spread of neural excitation, and thus the perception that may be elicited through electrical stimulation (Hanekom and Hanekom, 2016).

The interrelation between cochlear anatomy, electrode design and surgical approach is intuitive, as the anatomical interindividual variations influence the final position of the electrode carrier, the approach to CI and electrode design (Erixon *et al.*, 2009, Rask-Andersen *et al.*, 2012, Avci *et al.*, 2014, Avci *et al.*, 2017, Pietsch *et al.*, 2017). The type of and location of the electrode array, i.e. the proximity of the electrodes from the modiolar wall, have important psychoacoustic implications (Frijns *et al.*, 2001a, Balkany *et al.*, 2002, Husstedt, 2002, Saunders *et al.*, 2002, Hughes and Abbas, 2006, Stickney *et al.*, 2006, Adunka *et al.*, 2007, Rebscher *et al.*, 2007, Rebscher *et al.*, 2008, Connor *et al.*, 2009, Biedron *et al.*, 2010, Kalkman *et al.*, 2014, Kang *et al.*, 2015, Brant and Ruckenstein, 2016, Kalkman *et al.*, 2016, Büchner *et al.*, 2017, Dhanasingh and Jolly, 2017). Electrode array position is necessary for the creation of 3D volume conduction computational modelling (Finley *et al.*, 1990, Briaire and Frijns, 2000b, Frijns *et al.*, 2001a, Frijns *et al.*, 2001b, Skinner *et al.*, 2002, Li *et al.*, 2006, Van der Marel *et al.*, 2014, Malherbe *et al.*, 2015). Various types of electrode arrays from different manufacturers are available for CI. The

electrode carriers differ in size, length, number of electrode contacts and material characteristics (Brant and Ruckenstein, 2016, Dhanasingh and Jolly, 2017).

Studies on the location of the electrode array, i.e. the proximity of the electrodes from the modiolar wall and its psychoacoustic implications, have been conducted in animal studies (Shepherd *et al.*, 1993, Cords *et al.*, 2000)., and computational modelling (Finley *et al.*, 1990, Briaire and Frijns, 2000a, Briaire and Frijns, 2000b, Skinner *et al.*, 2002, Li *et al.*, 2006, Abdel Salam *et al.*, 2013, Kalkman *et al.*, 2014, Van der Marel *et al.*, 2014, Malherbe *et al.*, 2015, Hanekom and Hanekom, 2016, Malherbe *et al.*, 2016). Perimodiolar arrays, where the electrodes lie closer to the modiolar wall and target ganglion cells, have been found to elicit lower T- and C-levels than straight arrays, which lie closer to the outer wall (Kawano *et al.*, 1998, Saunders *et al.*, 2002, Zou *et al.*, 2015b). This has been extended to clinical trials, where improvement in T- and C-levels was found with perimodiolar arrays (Tykocinski *et al.*, 2001, Parkinson *et al.*, 2002, Pasanisi *et al.*, 2002, Cohen *et al.*, 2006, Hughes and Abbas, 2006). In contrast, researchers report that lateral wall electrode designs with longer electrode arrays and deeper insertion angles improved outcomes after CI surgery (Abdel Salam *et al.*, 2013, Büchner *et al.*, 2017, Dhanasingh and Jolly, 2017, O'Connell *et al.*, 2017, Timm *et al.*, 2018). Shorter electrodes may improve both short- and long-term hearing preservation, but randomised trials of short and standard-length electrodes are recommended (Abdel Salam *et al.*, 2013, Brant and Ruckenstein, 2016, Dhanasingh and Jolly, 2017). It is not yet clear what cochlear coverage achieves the best possible speech perception, in other words, if electrode contacts stimulate the neural fibre endings at the OoC or the SGCs directly (Timm *et al.*, 2018). Better frequency-to-place alignment in human cochleae may lead to improved stimulating strategies and help develop individually shaped CIs (Biedron *et al.*, 2010). Because of inter-individual variations that may affect neural excitation patterns (Malherbe *et al.*, 2013) and the goal of residual hearing preservation (Rebscher *et al.*, 2008), an electrode array ideally needs to be tailored to the individual implantee (Biedron *et al.*, 2009, Avci *et al.*, 2014).

Other than the anatomical factors and type of electrode array inserted, the surgical approach to CIs also influences psychometric outcomes. A surgical approach, i.e. cochleostomy versus

RW insertion, as well as surgical techniques, influences the final location of the electrode array and incidence of intracochlear trauma (Briggs *et al.*, 2005, Wardrop *et al.*, 2005, Tóth *et al.*, 2006, Martinez-Monedero *et al.*, 2011, Avci *et al.*, 2017). The insertion angle of the electrode array characterises the frequency-position function or tonotrophy of the cochlea better than the insertion depth of the electrode array (Biedron *et al.*, 2010, Avci *et al.*, 2017). The insertion angle is a function of the surgical approach taken by the implant surgeon. Recently, Avci *et al.* (2017) studied the dynamics of electrode carrier insertion. The authors determined that the insertion force profile is dependent on individual geometry and insertion trauma. The direction of insertion forces predicted the probability of intracochlear trauma and was not always correlated with higher force amplitudes. This means that the insertion angle and cochlear geometry play a significant role in CI forces and insertion trauma.

Other factors that have been investigated to affect excitation profiles, psychometric measures and speech and language outcomes are briefly discussed. Factors such as age, chemical composition of bone, sex and aetiology i.e. diseases that may cause hearing loss, affect bone tissue and therefore its resistive properties (Bozorg Grayeli *et al.*, 2005). Duration of hearing loss, time span after CI, prelingual status of the user, age at implantation, sex of the patient, education level, aetiology of hearing loss, level of residual hearing, use of personal amplification device (hearing aid) before CI, choice of electrode coupling (Peterson *et al.*, 2010, Cosetti and Waltzman, 2012), choice of processing algorithm or coding strategies, speech materials and evaluation environment, and surgical, audiological and rehabilitative procedures have all proven to contribute to variable speech and language outcomes (Blamey *et al.*, 1996). However, the biggest contributions to variability in psychoacoustic measures in CI have been attributed to individual cochlear anatomy and electrode position (Avci *et al.*, 2014, Van der Marel *et al.*, 2014, Malherbe *et al.*, 2015, Malherbe *et al.*, 2016, Avci *et al.*, 2017, Pietsch *et al.*, 2017).

2.7 METHODS TO DETERMINE ELECTRODE LOCATION

As discussed above, the final position of the electrode array and electrode contacts is determined by various factors. To determine the surgically applicable position of the

electrode carrier array postoperatively from the CT, CBCT, X-ray or CBCT scans of live implant users and high-resolution scans of temporal bones, the cochlear view was developed and modified by Cohen *et al.* (1996) and Xu *et al.* (2000). A 3D cylindrical coordinate system is introduced using the basal turn of the cochlea as the x and y planes and the centre of the modiolus as the z-axis. The 0º angle is defined by the most lateral point of the horizontal semicircular canal (Cohen *et al.*, 1996, Xu *et al.*, 2000, Verbist *et al.*, 2005, Verbist *et al.*, 2010). Several applications of this approach have been developed. Cohen *et al.* (1996) determined a spiral template function that approximates the shape of a radiographic image of the array. A template spiral was fitted to the radiographic array after approximating the centre position of the modiolus. Angles were measured from this point to the electrode. The cochlear view was used to measure the distance between the electrode contacts and modiolus (Tykocinski *et al.*, 2001, Balkany *et al.*, 2002, Skinner *et al.*, 2002, Kós *et al.*, 2005, Verbist *et al.*, 2005, Escudé *et al.*, 2006a, Connor *et al.*, 2009, Verbist *et al.*, 2010).

Other mathematical methods to determine the trajectory and electrode position have since been used. Researchers such as Ketten *et al.* (1998) and Skinner *et al.* (2002) used mathematical algorithms approximating 3D spiral functions to determine postoperative electrode insertion depth and location. Since small structures such as the BM, OoC and RM are not resolvable on CT images, their positions have to be estimated using known geometric data of the cochlea. This was conducted in a study of the human cochlea by Skinner *et al.* (2002), where the position of these structures was estimated using data obtained by Ketten *et al.* (1998). Mathematical equations have also been used to correlate histologic and radiographic reconstruction of intracochlear electrode position. Statistical models of intracochlear anatomy have been applied to an active shape model optimisation approach to identify the ST and SV. Array position is estimated by identifying its midline trajectory on the post-intervention scan and superimposing it onto the pre-intervention images using rigid registration (Noble *et al.*, 2011, Wanna *et al.*, 2015).

Reformatted images have been used to measure linear insertion depth by unfolding the electrode array using a curvilinear reformatting method followed by direct linear

measurement on the reformatted image, while angular insertion depth can be directly measured on the oblique coronal reformat (Abdel Salam *et al.*, 2013). Insertion depth angle is thought to be a better reference for the position of CI electrodes than the insertion length of the electrode (Escudé *et al.*, 2006a). The correlation between insertion angle, as established by (Xu *et al.*, 2000), and the insertion depth of the electrode is influenced by the size of the basal turn of the cochlea. Although only a small part of the whole cochlear duct is taken in by the apical turn, that is, 11 to 13% as stated by Hardy (1938) and Escudé *et al.* (2006a), it may have considerable importance for cochlear implantation, as it influences the correlation between insertion angle and electrode alignment to neural elements in the most apical parts of the cochlea (Biedron *et al.*, 2010).

Insertion depth has also been determined by counting the number of electrodes projecting medially to the cochlear promontory. Electrode position was compared using radiography and CT by evaluating the number of intra- and extracochlear electrodes (Zaghloul *et al.*, 2011). Insertion depth can be calculated by determining the linear depth in millimetres. Each electrode is outlined from the most apical electrode contact to a platinum marker placed at the RW using Canvase software. A grid is constructed around the electrode path to estimate angular insertion depth (Wardrop *et al.*, 2005).

Visual inspection of electrode array assesses the position at different locations within the basal turn of the cochlea such as mid-inferior segment, ascending segment, mid-superior segment and descending segment (Connor *et al.*, 2012). Scalar localisation is determined by the position of the array in reference to the SL, i.e. whether it is located below the BM in ST or above it in the combined space of the SV and SM (Finley *et al.*, 2008, Zou *et al.*, 2015a, Zou *et al.*, 2015b).

2.8 MODELLING IN CI

Anatomic and neural variations cannot be accurately measured by external observations. Even patients who have equal components inserted do not necessarily have equal intracochlear coverage or frequency distribution (Ketten *et al.*, 1998). Reliable measures of

intracochlear anatomy and intracochlear array position are needed for the generation of person-specific computational models and to provide a search field for landmark-based automated computational modelling of the cochlea. To create 3D volume conduction computational models with higher geometric accuracy, detailed parameters that describe the cochlea need to be assessed.

Volume conduction (VC) computational models were designed as a method to provide insight into the underlying mechanisms of cochlear stimulation without performing impractical or impossible *in vivo* experiments in CI users (Kalkman *et al.*, 2016). Volume conduction models of the cochlear structures and the surrounding soft tissue that describe the current distributions inside the cochlea are used to predict neural excitation characteristics. In the past, generic computational models that predicted general trends were used.

Computational modelling provides a quantitative, scientific method to facilitate a user-specific approach to cochlear implantation and subsequent management of an individual's hearing. The viability of such a modelling approach relies on a precise method of cochlear reconstruction that incorporates user-specific characteristics of the cochlea. User-specific computational modelling, which relies on accurate morphologic data, is a state-of-the-art approach to study the biophysical interface between the electrode array and the neural components. These person-specific computational models are now widely used and offer improved prediction of user-specific outcomes when compared to generic models (Frijns *et al.*, 2001a, Hanekom, 2001, Poznyakovskiy *et al.*, 2008, Malherbe, 2009, Kalkman *et al.*, 2014, Tran *et al.*, 2015, Hanekom and Hanekom, 2016, Kalkman *et al.*, 2016, Nogueira *et al.*, 2016, Wong *et al.*, 2016, Pietsch *et al.*, 2017). The development of these models is driven by a translational research approach that aims to apply these in the form of clinical tools to predict and maximise the final outcome of CI surgery (Kikidis and Bibas, 2014, Hanekom and Hanekom, 2016, Pietsch *et al.*, 2017).

While user-specific modelling is a better approach than those based on generic human or guinea pig cochlear shapes, the incorporation of more landmarks, and a level of detail that describes cochlear shape and size better, especially those of the inner structures that could

validate these computational models better, would be of even greater benefit. Refinement of these models to include user-specific traits may shed light on the factors that underlie interperson variation. This is especially important in a clinical setting and in cases of low-resolution scans. Clinicians may be able to gain insight into the workings of a user's electrically stimulated cochlea described by a user-specific 3D computational model. While high-precision reconstruction of a specific cochlea may offer the option to individualise the design of an electrode array for a user, it may also support the approach to implant surgery for standard electrode arrays. Detailed morphometric studies of cochlear anatomy can guide the approach to the cochleostomy and electrode array insertion to minimise insertion trauma, optimise neuronal and hair cell preservation and ultimately present a method to control electrode location within the ST (Martinez-Monedero *et al.*, 2011). For this reason, there has been a strong focus in current research in the field to develop novel approaches to improve the restoration of hearing with CIs that would consider person-specific anatomical and clinical data.

3D computational modelling forms an integral part of modern-day research in CIs and relies on parameters that include the spatial dimensionality of the cochlea (Hanekom and Hanekom, 2016). The landmarks that are derived for the creation of such user-specific models are either extracted from low-resolution scans or only include a limited number of landmarks (Briaire and Frijns, 2000a, Frijns *et al.*, 2001a, Choi and Hsu, 2009, Malherbe, 2009, Malherbe *et al.*, 2013, Choi and Wang, 2014, Kalkman *et al.*, 2014, Dang *et al.*, 2015, Malherbe *et al.*, 2016, Pietsch *et al.*, 2017).

2.9 LANDMARK BASED METHODS TO MEASURE COCHLEAR PARAMETERS

Anatomic and neural variations cannot be accurately measured by external observations. Even patients who have equal components inserted do not necessarily have equal intracochlear coverage or frequency distribution (Ketten *et al.*, 1998). Reliable measures of intracochlear anatomy and intracochlear array position are needed for the generation of person-specific computational models and to provide a search field for landmark-based

automated computational modelling of the cochlea. To create 3D volume conduction computational models with higher geometric accuracy, detailed parameters that describe the cochlea need to be assessed.

Volume conduction (VC) computational models were designed as a method to provide insight into the underlying mechanisms of cochlear stimulation without performing impractical or impossible *in vivo* experiments in CI users (Kalkman *et al.*, 2016). VC models of the cochlear structures and the surrounding soft tissue that describe the current distributions inside the cochlea are used to predict neural excitation characteristics. In the past, generic computational models that predicted general trends were used. Several VC models have been developed and include lumped parameter models (Suesserman and Spelman, 1993, Jolly *et al.*, 1996), boundary element models (Frijns *et al.*, 1995, Frijns *et al.*, 2000, Briaire and Frijns, 2000a, Frijns *et al.*, 2001b), finite element models (Hanekom, 2001, Lim *et al.*, 2005) and finite difference models (Steele and Taber, 1979). These models vary in detail and are based on the generic geometry of guinea pig and human cochleae, which only predict generalised trends that may not be viable for all individuals. Generalised models do not account for inter-subject variability in cochlear anatomy, electrode location, neural survival patterns and insertion damage. To address the limitations of the generic cochlear VC model, a need for the design of person-specific cochlear models that accurately describe the cochlear geometry arose.

Computational modelling provides a quantitative, scientific method to facilitate a user-specific approach to cochlear implantation and subsequent management of an individual's hearing. The viability of such a modelling approach relies on a precise method of cochlear reconstruction that incorporates user-specific characteristics of the cochlea. User-specific computational modelling, which relies on accurate morphologic data, is a state-of-the-art approach to study the biophysical interface between the electrode array and the neural components. These person-specific computational models are now widely used and offer improved prediction of user-specific outcomes when compared to generic models (Frijns *et al.*, 2001a, Hanekom, 2001, Poznyakovskiy *et al.*, 2008, Malherbe, 2009, Kalkman *et al.*, 2014, Tran *et al.*, 2015, Hanekom and Hanekom, 2016, Kalkman *et al.*, 2016, Nogueira *et*

al., 2016, Wong *et al.*, 2016, Pietsch *et al.*, 2017). The development of these models is driven by a translational research approach that aims to apply these in the form of clinical tools to predict and maximise the final outcome of CI surgery (Kikidis and Bibas, 2014, Hanekom and Hanekom, 2016, Pietsch *et al.*, 2017).

While user-specific modelling is a better approach than approaches based on generic human or guinea pig cochlear shapes, the incorporation of more landmarks, and a level of detail that describes cochlear shape and size better, especially those of the inner structures that could validate these computational models better, would be of even greater benefit. Refinement of these models to include user-specific traits may shed light on the factors that underlie interperson variance. This is especially important in a clinical setting and in cases of low-resolution scans. Clinicians may be able to gain insight into the workings of a user's electrically stimulated cochlea described by a user-specific 3D computational model. While high-precision reconstruction of a specific cochlea may offer the option to individualise the design of an electrode array for a user, it may also support the approach to implant surgery for standard electrode arrays. Detailed morphometric studies of cochlear anatomy can guide the approach to the cochleostomy and electrode array insertion to minimise insertion trauma, optimise neuronal and hair cell preservation and ultimately present a method to control electrode location within the ST (Martinez-Monedero *et al.*, 2011). For this reason, there has been a strong focus in current research in the field to develop novel approaches to improve the restoration of hearing with CIs that would consider person-specific anatomical and clinical data.

3D computational modelling forms an integral part of modern-day research in CIs and relies on parameters that include the spatial dimensionality of the cochlea (Hanekom and Hanekom, 2016). The landmarks that are derived for the creation of such user-specific models are either extracted from low-resolution scans or only include a limited number of landmarks (Briaire and Frijns, 2000a, Frijns *et al.*, 2001a, Choi and Hsu, 2009, Malherbe, 2009, Malherbe *et al.*, 2013, Choi and Wang, 2014, Kalkman *et al.*, 2014, Dang *et al.*, 2015, Malherbe *et al.*, 2016, Pietsch *et al.*, 2017).

2.10 CONSTRUCTION OF THREE-DIMENSIONAL COMPUTATIONAL MODELS OF THE COCHLEA

Construction of landmark-based 3D computational cochlear models reported in the literature rely on a few basic landmarks, such as the lateral-most point on the cochlear wall, lateral-most and medial-most points on the SL, and the points that define the cochlear inlet (Frijns *et al.*, 1995, Frijns *et al.*, 1996, Kral *et al.*, 1998, Briaire and Frijns, 2000a, Briaire and Frijns, 2000b, Frijns *et al.*, 2001a, Hanekom, 2001, Givelberg and Bunn, 2003, Hanekom, 2005, Cohen, 2009, Malherbe, 2009, Gunz *et al.*, 2012, Choi and Wang, 2014, Kalkman *et al.*, 2014, Dang *et al.*, 2015, Malherbe *et al.*, 2016). Further landmarks that have been measured are described in section 2.9.

Givelberg and Bunn (2003) used the position of the centre line of the BM, its width and cross-sectional area of the scalae to create a geometric model of the cochlear anatomy, while Connor *et al.* (2009) constructed their model from the most distal boundary of the cochlear wall and most superior boundary of the cochlear duct. Several authors employed segmentation techniques to create 3D cochlear models by identifying the anatomical structures that make up the cochlea (Seemann *et al.*, 1999, Rodt *et al.*, 2002a, Li *et al.*, 2007, Poznyakovskiy *et al.*, 2011, Rau *et al.*, 2011, Kang *et al.*, 2015, Tran *et al.*, 2015, Wong *et al.*, 2016). The anatomical structures are selected using the colour or greyscale value of the specific structures that make up the cochlea. Segmentation techniques can be manual (Voie and Spelman, 1995, Wada *et al.*, 1998, Seemann *et al.*, 1999, Ghiz *et al.*, 2001, Li *et al.*, 2006, Liu *et al.*, 2007, Hofman *et al.*, 2009), semi-automatic (Yoo *et al.*, 2001, Xianfen *et al.*, 2005, Wang *et al.*, 2006, Lee *et al.*, 2010, Meshik *et al.*, 2010, Tran *et al.*, 2015) or automatic (Noble *et al.*, 2011, Reda *et al.*, 2014). Structures that are segmented include the ossicles, vestibulocochlear organ with cochlear aquaduct, CNVII, vestibulocochlear nerve (CNVIII) (Seemann *et al.*, 1999, Wang *et al.*, 2006), ST (Noble *et al.*, 2011, Poznyakovskiy *et al.*, 2011), SV (Noble *et al.*, 2011), tympanic membrane, middle ear muscles and internal carotid artery (Wang *et al.*, 2006). Some researchers based their segmentation of the ST, SV and spiral ganglion on a previously active cochlear shape model using eigen analysis where a reference model of the labyrinth is created manually, training volumes are registered to the

reference model and the surfaces produced are manually adjusted, i.e the model-created segmentation is smoothed out to correct any errors that may have occurred during the segmentation process (Reda *et al.*, 2014). Tran *et al.* (2015) created a cadaver head model using specialised software to segment the perilymph, grey matter, white matter, cerebellum, brainstem, spinal cord, CNII, CNVII, CNVIII, cerebrospinal fluid, bone, scalp, blood, eyes and sinuses. The cochlear apparatus with implanted CI could then be extracted from the head model.

Landmark-based geometric studies are used to summarise shape, using landmarks that offer immediate visualisation of the shape and the morphological description of variation and change in a structure. These landmarks are a multidimensional constellation of discrete anatomical loci described by Cartesian coordinates and are points of correspondence on each specimen that match between and within a population that is distinguishable in all specimens in the study. These geometric parameters contain information on the spatial relationship among landmarks in a specific organism (Bookstein, 1986, Bookstein, 1997, Gunz *et al.*, 2012). It is important to remember that landmarks should be digitised in the same order for all specimens and that missing landmarks should be kept track of. Missing data i.e landmarks that cannot be measured, cannot be included in an analysis involving that landmark. Extraction of landmark coordinates is associated with some degree of measurement error, which may result from inconsistent tilting of the specimen, non-coplanarity of landmarks or difficulty in pinpointing the landmark locus. In other words, it should be possible to apply the measurement protocol employed to a range of imaging methods (Gunz *et al.*, 2012).
For 3D cochlear reconstruction, landmark-based techniques have a number of advantages over segmentation-based techniques:

i. Landmark-based techniques can accommodate small anatomical variations in morphology and resulting shape deformation, especially those in small anatomical structures such as the cochlea (Bookstein, 1986, Bookstein, 1997, Polly *et al.*, 2016). In contrast, segmentation techniques rely on knowledge of a set of pixels and voxels of an average or generic structure of the organ in question and do not accommodate variation in morphology (Noble *et al.*, 2011)

ii. Landmarks offer a description of the spatial relationship between structures and provide improved localisation over edge-based segmentation techniques (Kaur and Kaur, 2014) and registration, while edge-detection algorithms used in segmentation procedures may often fail to mark real edge points or produce distorted duplicate and/or unconnected edges for the object boundary (Poznyakovskiy *et al.*, 2008, Poznyakovskiy *et al.*, 2011). Segmentation techniques using region growing (Yoo *et al.*, 2000), active contours (Yoo *et al.*, 2001), level-sets (Xianfen *et al.*, 2005) or principle flow filter algorithms (Baker and Barnes, 2004) result in segmentation of the bony labyrinth as a whole, with no differentiation between the scalae, thereby masking the inner details of the cochlear channels. Segmentation of cross-sections by Poznyakovskiy *et al.* (2008) worked well in the medial cochlear region, but failed in the basal and apical regions owing to the oblique angle of the image plane relative to the borders of the scalae, again distorting the geometry.

iii. Landmark-based techniques rely on landmarks that are easy to detect, stable and have characteristics that do not alter to a great extent in the presence of abnormalities (Bookstein, 1986, Bookstein, 1997). In comparison, segmentation can be especially difficult in structures that appear homogenous, lack clear boundaries, have a sufficient presence of noise, partial-volume effects and limitation of imaging techniques (Pal and Pal, 1993, Kaur and Kaur, 2014). Furthermore, segmentation techniques rely on prior knowledge of the expected size, shape, position and texture of the organ in question.

iv. Segmentation techniques have a high computational cost (Pal and Pal, 1993, Kaur and Kaur, 2014) and require heavy user interaction, as highlighted by previous studies (Voie and Spelman, 1995, Wada *et al.*, 1998, Seemann *et al.*, 1999, Parthasarathi *et al.*, 2000, Yoo *et al.*, 2000, Ghiz *et al.*, 2001, Yoo *et al.*, 2001, Rodt *et al.*, 2002a, Baker and Barnes, 2004, Xianfen *et al.*, 2005, Li *et al.*, 2006, Wang *et al.*, 2006, Poznyakovskiy *et al.*, 2008, Hofman *et al.*, 2009, Lee *et al.*, 2010, Poznyakovskiy *et al.*, 2011, Reda *et al.*, 2014, Tran *et al.*, 2015, Rivas *et al.*, 2017), while landmark-based methods may offer more efficient reconstruction algorithms that account for anatomical variability (Gunz *et al.*, 2012).

v. Another challenge for cochlear reconstruction via segmentation is the speckled nature of tomography noise, which decreases the precision of cross-section segmentations and contributes to the jitter of localisation centres. This can destabilise the centreline estimation of the tangent vector, which causes poor image plane definition and destabilises the whole algorithm (Poznyakovskiy *et al.*, 2008). These distortions can be smoothed out by applying additional filters (Poznyakovskiy *et al.*, 2011), which in turn adds to increased computational time and less efficient reconstruction.

Landmark-based studies provide an alternative approach whereby anatomical structures can be delineated by creating a wire framework that outlines the surfaces of each structure. Most authors have created 3D computational models using only one mid-modiolar slice instead of following these landmarks throughout the full rotations of the cochlea. Digitisation of detailed landmarks on mid-modiolar slices measured at interval degree slices is needed to provide a more detailed spiral trajectory of the landmarks and will prove more insightful on capturing small anatomical variations. These authors use a limited set of parameters, making it difficult to define the exact cochlear shape. Mathematically, the cochlear shape has been approximated by different spiral functions based in Archimedean or logarithmic spirals (Ketten *et al.*, 1998, Yoo *et al.*, 2000), which require elaborate post-processing procedures. Landmark-based reconstruction of the cochlea thus provides a means to create a reconstruction methodology that adapts the level of detail to the resolution of the available source.

For these reasons, a landmark-based approach to cochlear reconstruction is followed in this study, with the objective to define a standardised set of landmarks to serve as a reference for 3D model construction. Both higher-resolution µCT scans and low-resolution CT scans are used to determine the relevant subsets of landmarks that may be reliably identified for a specific image modality.

2.11 LANDMARK-BASED AUTOMATIC COMPUTATIONAL MODELLING APPROACHES

Currently user-specific models are used as a primary research tool. The development of 3D computational models with high accuracy, which include detailed anatomical structures, is a time-consuming process (Wang *et al.*, 2006, Malherbe, 2009, Tran *et al.*, 2015). The generation of such models is important to provide accurate search fields needed for the development of rapid landmark-based automated models that can be translated into a clinical tool for the maintenance of these models. Studies focus on the outcomes of 3D computational models rather than the development of the model (Yoo *et al.*, 2000, Yoo *et al.*, 2001, Rodt *et al.*, 2002a, Wang *et al.*, 2006, Malherbe *et al.*, 2016).

The development of user-specific computational models of the cochlea based on knowledge-based landmark detection are of the highest accuracy (90.33%) as reported by Gupta *et al.* (2015). Automated development of user-specific computational modelling based on knowledge-based landmark detection uses pre-defined or pre-agreed definitions of anatomical landmarks that describe cochlear shape and size. Therefore, this study focused on the definition of such landmarks, quantification of the characteristics of landmark points, definition of smaller, more accurately located search fields and derivation of obscured landmarks from consistently present landmarks for use in automated landmark-based user-specific model development. The landmarks were also used for the classification of the cochlea and its correlation with psycho-acoustic outcomes of CI users.

2.12 METHODS TO DETERMINE OBSCURED LANDMARKS

In order to create models of greater accuracy, the relation among landmarks as a possible means to derive important landmarks that may not be visible on low-resolution scans or scans that contain artefacts from an implanted electrode array, movement artefacts or a soft tissue interface needs to be addressed. A minimal set of landmarks that is required for the calculation of obscured landmarks is needed. In this way provision for the improvement of the integrity of the dimensional characteristics of computational modelling is made while actively accommodating low-resolution data, thereby still generating models of great detail.

It is intuitive that the presence of more visible landmarks can be used to derive obscured landmarks and will generate more detailed cochlea. Literature on the calculation of obscured landmarks in the field of cochlear research is lacking. Detection of anatomical landmarks and obscured landmarks is well recognised in a wide range of medical image analyses (Alansary *et al.*, 2019), as well as anthropometry studies (Douglas, 2004, Lagravère *et al.*, 2010, Le-Tien and Pham-Chi, 2014). Normative data for landmark location and algorithms for the extraction of obscured landmarks in terms of image processing are lacking when measuring a specific feature or landmark.

2.13 MODIOLAR CORRECTION METHODS

Misalignment of the modiolar axis may cause non-reproducible measurements and results. A modiolar correction method is needed for the exact extraction and interpretation of measured landmarks on the cochlea. A standard method, the cochlear view (as described in section 2.6), provides a standard and unambiguous reference system for anatomical studies of the cochleae. The method used by Verbist *et al.* (2010) in itself presents with interobserver errors, as there are two main alternatives for choosing the origin of the modiolar axis (z-axis), i.e orientating the z-axis from the helicotrema/apex to the base of the cochlea or choosing the base as the origin and the apex as the endpoint. Other methods used to define the modiolar axis include manually adjusted multiplanar reconstruction (Van der Marel *et al.*, 2014) or setting two points (Poznyakovskiy *et al.*, 2008, Verbist *et al.*, 2009), maximisation of the dark pixel area using minimum intensity projection (Escudé *et al.*, 2006a) or using three nonlinear least square minimisation based algorithms (Yoo *et al.*, 2000). Demarcy *et al.* (2016) used a method based on the intrinsic geometrical properties of the cochlear centreline. The researchers based their equations on the logarithmic description of the cochlear spiral and computed the modiolar axis by performing robust principal component analysis using an extension of the expectation maximisation algorithm. The procedure involves the calculation of the Student's t-distribution, a maximisation step where the mean and variance are updated by computing a weighted sum of the data, construction of a cylindrical coordinate system based on the method proposed by Verbist *et al.* (2010) and extraction of the centrelines for the tympanic and vestibular membranes (Demarcy *et*

al., 2016). The method by Demarcy *et al.* (2016) is, however, not applicable to noisy images. Recently, kinematic motion (natural growth) modelling of the spiral shape of the cochlea was performed with the modiolar axis being extracted as the rotation component (Wimmer *et al.*, 2019).

2.14 CHAPTER SUMMARY

The literature discussed in the previous sections provided foundational anatomical, data-processing and computational modelling techniques needed for the study. The overview of the literature identified critical research gaps needed for the developmental stages of 3D computational modelling of the cochlea by addressing cochlear morphing using different approaches. Furthermore, the literature identified gaps in the translational approach to cochlear modelling, which were investigated in this thesis.

CHAPTER 3 PREDICTION OF THE TRAJECTORY OF OBSCURED COCHLEAR SPIRALS FOR THE DEVELOPMENT OF THREE-DIMENSIONAL COMPUTATIONAL MODELLING

3.1 CHAPTER OBJECTIVES

The objectives of this chapter are to define a set of landmarks that describe the cochlear geometry, develop a workflow for the extraction of the cochlear geometry from the predefined landmark set, classify cochleae according to taxonomy and describe the spirals that constitute the cochlea. The chapter further describes each cochlea using analytical equations and determines the absolute error with which cochlear spirals can be predicted from the reference spirals derived from a set of high-resolution µCT scans. These data are used to construct a CSRF that comprises a normalised description of the cochlear spirals, the standard deviation for each spiral and a set of predictors for obscured spirals. The CSRF contains frameworks for a pooled dataset, as well as datasets for different classes of cochleae as classified according to the vertical trajectory of the cochlea spiral.

3.2 ABSTRACT

The variability and uniqueness of the dimensions of the human cochlea among individuals require a regular approach to describe the anatomy mathematically for inclusion in 3D computational models of the auditory periphery. Cochlear shape variability was confirmed by two findings that the vertical profiles of a cochlea can be classed into rollercoaster, intermediate and sloping cochleae, based on landmarks placed on the lateral wall of the cochlear spiral. Identification of landmarks on images of live cochleae is limited by the low resolution of scans. A CSRF that describes each spiral for each cochlear class is needed to serve as a reference for the derivation of spirals that may be obscured when constructing computational cochlear models from clinically available scans. Therefore, the objective of this study is to derive an analytical description of each spiral trajectory from high-resolution data to develop a CSRF that provides equations enabling the prediction of obscured cochlear spirals. This CSRF could serve as a reference for, and support the development of, person-specific computational models of the cochlea. For this purpose, µCT scans of 31 cochleae from dry skulls and temporal bones were collected. The images were reconstructed by placing landmarks at 5° intervals on each mid-modiolar section for each cochlea (1800 landmarks per cochlea). These included landmarks that described the superior, inferior, lateral, medial, superolateral, inferolateral, lateral spiral lamina and medial spiral lamina spirals. Polynomial functions for each cochlear spiral and each cochlea were calculated using custom algorithms programmed in Matlab (Mathworks)[1]. The normalised mean absolute error (NMAE) was used as a measure to determine which spiral was the best predictor of an obscured spiral. Predictions were validated against the measured data.

3.2 INTRODUCTION

The uniqueness of the human cochlea's shape and variability in its dimensions (Dimopoulos and Muren, 1990, Ketten *et al.*, 1998, Escudé *et al.*, 2006c, Biedron *et al.*, 2009, Erixon *et al.*, 2009, Martinez-Monedero *et al.*, 2011, Avci *et al.*, 2014, Van der Marel *et al.*, 2014, Wurfel *et al.*, 2014, Pietsch *et al.*, 2017) emphasises the need for methods to describe the cochlear morphology in great detail if person-specificity needs to be accounted for when

[1] www.mathworks.cm

constructing 3D computational models of the cochlea (Erixon *et al.*, 2009, Rask-Andersen *et al.*, 2012, Shin *et al.*, 2013, Avci *et al.*, 2014, Van der Marel *et al.*, 2014, Avci *et al.*, 2017). In a review by Ni *et al.* (2014), it is clear that one of the objectives of 3D computational models of the cochlea is to predict speech and language outcomes.. The authors state that cochlear models need to be refined as assumptions and data fitting used in modelling of the cochlea is largely empirical and difficult to validate.

Recently the vertical trajectory of the ST against the vertical height has been used to classify variations in cochlear anatomy. The taxonomy of the human cochlea consists of three classes according to three critical anatomical features in the vertical trajectory of the ST (dips, jumps and peaks). Rollercoaster cochleae are characterised by a dip followed by an upward course; sloping cochleae follow an upward trajectory without significant downward trends, while intermediate cochleae are characterised by a vertical jump in the vertical trajectory of the ST (Avci *et al.*, 2017). Rollercoaster cochlea would appear to push the first and second turn closer together. The study considered the first 720^0 of the cochleae, as this is the area of interest in CI surgery and 3D computational modelling of the cochlea. This study was further expanded by Pietsch *et al.* (2017), who described cochlear shape mathematically from 3D reconstructions of 108 cochlear casts and 30 µCT scans of cochleae. The authors digitised the lateral spirals of the cochleae using 120 parameters and used polynomial and logarithmic equations to describe the variation in the cochleae to show that polynomial equations are a better fit, i.e. describe cochlear shape better. The authors classified human cochlea according to shape, i.e. either having a rollercoaster or sloping profile, but did not address cochleae of the intermediate class. The authors mathematically analysed which type of geometrical spiral the cochlea really follows and indicated that one cochlea is not simply a blueprint or scaled version of another. The method included only a small set of landmarks (120) measured on the lateral spiral and did not indicateon the selection of landmarks required for more detailed user-specific cochlear modelling or provide a method by which landmarks can be placed on low-resolution scanning. These critical features are important for the development of more accurate 3D computational models of a CI user.

Currently, construction of landmark-based 3D computational cochlear models reported in the literature (Frijns *et al.*, 1995, Frijns *et al.*, 1996, Briaire and Frijns, 2000a, Briaire and Frijns, 2000b, Frijns *et al.*, 2001a, Hanekom, 2001, Hanekom, 2005, Choi and Hsu, 2009,

Malherbe *et al.*, 2013, Choi and Wang, 2014, Kalkman *et al.*, 2014, Dang *et al.*, 2015, Malherbe *et al.*, 2015, Pietsch *et al.*, 2017) rely on a few basic landmarks, such as the lateral-most point on the cochlear wall, lateral-most and medial-most points on the SL, and the points that define the cochlear inlet (Hanekom and Hanekom, 2016). Computational models of the cochlea should typically include the perilymph (location of ST and SV), endolymph (located in the SM), BM and spiral ganglion, as these affect current spread (Frijns *et al.*, 1995, Hanekom, 2001, Hanekom, 2005). Other structures that are important are RM, the *stria vascularis* and very importantly, an accurate representation of the enveloping bone, as the resistive properties of the bone in which the cochlea is embedded are one of the most important computational modelling parameters (Malherbe *et al.*, 2015). High-fidelity model generation for live implant users remains a challenge, as the available imaging data are of low resolution and thus need to be augmented with existing knowledge of the typical trends and variations observed in cochlear morphological data (Malherbe *et al.*, 2013, Malherbe *et al.*, 2016). Studies thus far do not make provision for the derivation of obscured landmarks from visible landmarks and a standard set of prediction polynomial equations in the form of a CSRF is much needed.

In this study, knowledge-based landmark techniques were chosen for 3D cochlear reconstruction to describe the spiralling nature of the cochlea and the possibility of determining obscured spirals from visible landmarks. Landmark-based techniques rely on features that are easy to detect and remain stable, which can accommodate small anatomical variations in morphology and resulting shape deformation, especially those in small anatomical structures such as the cochlea (Bookstein, 1986, Bookstein, 1997, Gunz *et al.*, 2012, Polly *et al.*, 2016). Landmarks offer a description of the spatial relationship between structures, provide improved localisation and image registration and do not rely on prior knowledge of the expected size, shape, position and texture of the organ in question (Pal and Pal, 1993, Kaur and Kaur, 2014). With segmentation techniques, it may be difficult to differentiate between the scalae, thus masking the inner details of the cochlea (Yoo *et al.*, 2000, Yoo *et al.*, 2001, Baker and Barnes, 2004). This can destabilise the centreline estimation of the tangent vector, which causes poor image plane definition and destabilises the whole algorithm (Poznyakovskiy *et al.*, 2008). While these distortions can be smoothed out by applying additional filters (Poznyakovskiy *et al.*, 2011), this adds to increased computational time and therefore causes less efficient reconstruction (Yoo *et al.*, 2000, Ghiz

et al., 2001, Yoo *et al.*, 2001, Baker and Barnes, 2004, Poznyakovskiy *et al.*, 2008, Reda *et al.*, 2014, Tran *et al.*, 2015).

Although histological sections are the most reliable way to visualise cochlear anatomy, these sections cannot be sliced in a mid-modiolar way. µCT scans offer a solution, as the images are of high quality and sufficient to view the cochlear structures with the possibility of distinguishing fine mid-modiolar sections. Therefore, µCT scans were used to determine the relevant subsets of landmarks (refer to figure 3.1) that define the different spirals, i.e. lateral spiral (LS), medial spiral (MS), superior spiral (SS), inferior spiral (IS), superolateral spiral (SLS), inferolateral spiral (ILS), lateral spiral lamina (LSL) and medial spiral lamina (MSL). A workflow was developed to reconstruct each cochlea from the measured landmark data and to provide cochlear dimensions, polynomial coefficients and cylindrical data points for each cochlea.

The study investigated the relation among landmarks as a possible means to derive important spiral trajectories that may be obscured on low-resolution scans. In this way, the study makes provision for the improvement of the fidelity of the geometrical characteristics available for computational modelling with improving imaging technology, while actively accommodating low-resolution data in an attempt to allow the generation of models of great detail, irrespective of the data source.

3.3 MATERIALS AND METHODS

Landmarks that define the cochlear walls, SL, and cochlear turns that could serve as a reference for the analytical description of obscured landmarks on clinically available *in vivo* imaging modalities were identified and measured on µCT scans. To validate the predicted spirals, percentage normalised mean standardised error (PNMAE) was applied to determine the error between experimental (measured) data and the reconstructed spiral data.

3.3.1 Materials

Twenty-seven cochleae from dry temporal bones and skulls were scanned at NECSA (South African Nuclear Energy Corporation), which houses the Nikon XTH 225 ST micro-focuses

X-ray tomography scanner (MIXRAD), according to the procedure of Hoffman and De Beer (2012). The samples were placed in a polystyrene mould to ensure that each sample remained stable. Because of the size of the samples in this study, a spatial resolution of 90 – 120 microns was achieved. Each of the 2D digitised radiographs per specimen, taken at different angles, consisted of an array of 2048 x 2048-pixel elements (maximum for the current detector at the µCT system) and each element with a different grey scale (up to 65536 grey levels). Scanning parameters for the µCT scans were as follows: 33.33 min exposure time, 2 s rotation time, 100 kV tube voltage, 100 effective mAs, resolution of 120 µm.

3.3.2 Methods

3.3.2.1 Imaging

The volume files from the µCT scans were imported into VGStudioMAX-2.2 visualisation software (Volume Graphics GmbH, Heidelberg, Germany) for the 3D rendering, segmentation and visualisation of the reconstructed volume data (Volume Graphics, 2010)[1].

3.3.2.2 Identification of landmark points for model reconstruction

The choice of landmarks was informed by the typical landmarks employed to construct 3D models of the cochlea. For reconstruction of live cochlea, the choice landmarks are limited by the anatomical features that are visible on clinical images. However, for the reconstruction of the inner structures, model development still relies on a generic template of a section through a cochlear spiral. A user-specific inner structure can potentially improve the predictions from the models, as it would afford a better description of the location of the electrode array relative to the anatomical structures. The only visible internal structure on µCT is the SL, which could be used to adapt the inner structure template of the cochlea to reflect person-specificity of the internal structures. The chosen landmarks inherently reflect gross anatomical variations that have been observed and are located such that information on the structures not visible on low-resolution scans can be derived. Most of the landmarks describe the spiralling nature of the cochlear structures and may thus serve as a framework to construct a computational description of the cochlear anatomy. These include the lateral-

[1] www.volumegraphics.com

most, medial-most, superior-most, inferior-most, superolateral, inferolateral, superomedial and inferomedial landmarks of each turn. As mentioned the lateral- and medial-most points of the SL were measured, as this gives an indication of the internal structure of the cochlea. The medial-most point of the cochlear wall was measured, as it gives an indication of the location of the modiolar wall and in cases were an electrode array is inserted, it can be used to determine the distance between the array and the modiolar wall. The inferior-most points of the apical turn give an indication of the extent of the modiolus. The set of landmarks that was identified also defines specific dimensions (i.e. metric length, width and base of each turn, total cochlear height, length of the spiral lamina) of the cochlea for validation against the literature. The landmarks that define the eight spirals of the cochlea, as well as polynomial predictors for obscured spirals (MS, LSL, SSL) and spirals that are not necessarily measured on low-resolution images but improve the fidelity of the reconstruction (SLS and ILS), were chosen.

Table 3.1 provides a description of each of the landmarks selected for the 3D model reconstruction framework, while Figure 3.1 shows the location of the landmarks on mid-modiolar sections through the cochlea.

Given the coordinates of the landmarks in Table 3.1, as the cochlea is a rotational structure, it follows that landmarks need to be digitised on 36 complete mid-modiolar sections only, separated by 5º and corresponding to a rotation of 180º to obtain data to describe the full trajectory of a point along the length of the cochlea. The 5^0-measurement interval was somewhat arbitrarily decided upon, as the change in location of landmarks is subtle; measuring landmarks on smaller intervals is labour-intensive and does not show clear changes in landmarks' location, while measurements on larger spaced degree intervals could miss local variations.

If one considers the lateral-most point on the right basal turn (point 1), it can be seen that as the angle is increased, this point meets the lateral-most point on the left basal turn (point 8) at 180º. Likewise, point 8 will meet the lateral-most point on the right middle turn (point 2) at 360º (0º). The sequences of landmarks that describe specific spirals are given in Table 3.2.

Table 3.1. List of landmarks placed on each mid-modiolar section at 5° intervals

Landmark	Area of placement
1	Lateral-most point on right basal turn
2	Lateral-most point on right middle turn
3	Lateral-most point on right apical turn
4	Lateral-most point on right apical turn (furthest from point 3)
5	Lateral-most point on left apical turn
6	Lateral-most point on left apical turn (furthest point from point 5)
7	Lateral-most point on left middle turn
8	Lateral-most point on left basal turn
9	Modiolar inlet on left
10	Modiolar inlet on right
11	Superior-most point on right basal turn
12	Superior-most point on right middle turn
13	Superior-most point on right apical turn (Between 3 and 4)
14	Superior-most point on left apical turn (Between 5 and 6)
15	Superior-most point on left middle turn
16	Superior-most point on left basal turn
17	Inferior-most point on right basal turn
18	Inferior-most point on right middle turn
19	Inferior-most point on right apical turn
20	Inferior-most point on left apical turn
21	Inferior-most point on left middle turn
22	Inferior-most point on left basal turn
23	Medial-most point on right basal turn
24	Medial-most point on right middle turn
25	Highest point on modiolius
26	Medial-most point on right apical turn
27	Medial-most point on left middle turn
28	Medial-most point on left basal turn
29	Lateral-most point on SL on right basal turn
30	Lateral-most point on SL on right middle turn
31	Lateral-most point on SL on right apical turn
32	Lateral-most point on SL on left apical turn
33	Lateral-most point on SL on left middle turn
34	Lateral-most point on SL on left basal turn
35	Medial-most point on SL on right basal turn

36	Medial-most point on SL on right middle turn
37	Medial-most point on the SL on right apical turn
38	Medial-most point on SL on left apical turn
39	Medial-most point on SL on left middle turn
40	Medial-most point on SL on left basal turn
41	Between 1 and 11
42	Between 2 and 12
43	Between 7 and 15
44	Between 16 and 8
45	Between 1 and 17
46	Between 2 and 18
47	Between 7 and 21
48	Between 8 and 22
49	Between 9 and 22
50	Between 10 and 18

Table 3.2. Landmark sequences that form each spiral

Spiral	**Landmarks**
Lateral spiral (LS) (Lateral-most points)	1,8,2,7,3,6
Medial spiral (MS) (Medial-most points)	23,28,24,27,4,5
Superior spiral (SS) (Superior-most points)	11,16,12,15,13,14
Inferior spiral (IS) (Inferior-most points)	17,22,18,21,19,20
Lateral spiral lamina (LSL) spiral (Lateral-most point)	29,34,30,33,31,32
Medial spiral lamina (MSL) spiral (Medial-most point)	35,40,36,39,37,38
Superolateral spiral (SLS)	41,44,42,43
Inferolateral spiral (ILS)	45,48,46,47

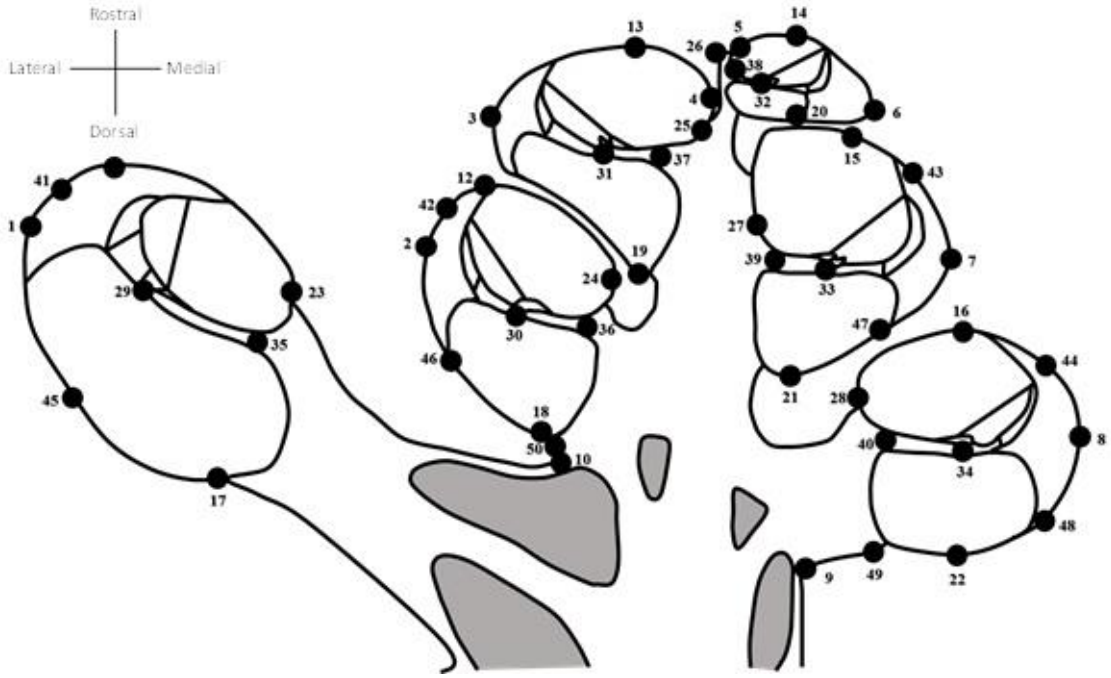

Figure 3.1. Illustration of the location of the complete set of landmarks on a schematic representation of a mid-modiolar section through the cochlea.

3.3.2.3 Orientation of image data and manual digitization of landmarks

Each cochlea was orientated in the cochlear view according to the method described by (Verbist *et al.*, 2010). Landmarks were mapped on the mid-modiolar sections of each cochlea at 5° intervals using the multipoint measuring tool in Image J[1]. Figure 3.2 shows the placement of visible landmarks on µCT images.

To create a high-definition representation of the cochlear morphology, specifically the LS, MS, SS, IS, SLS, ILS, LSL and MSL, the objective was to identify all the visible landmarks in the set, as a reduced set of landmarks compromises the level of geometric detail that can be included in the cochlear computational modelling and the accuracy with which predicted spirals can be calculated. Figure 3.3 below illustrates this principle, where a sparser set of landmarks is visible in Figure 3.3a and a more complete set in Figure 3.3b.

[1] https://imagej.nih.gov/ij/

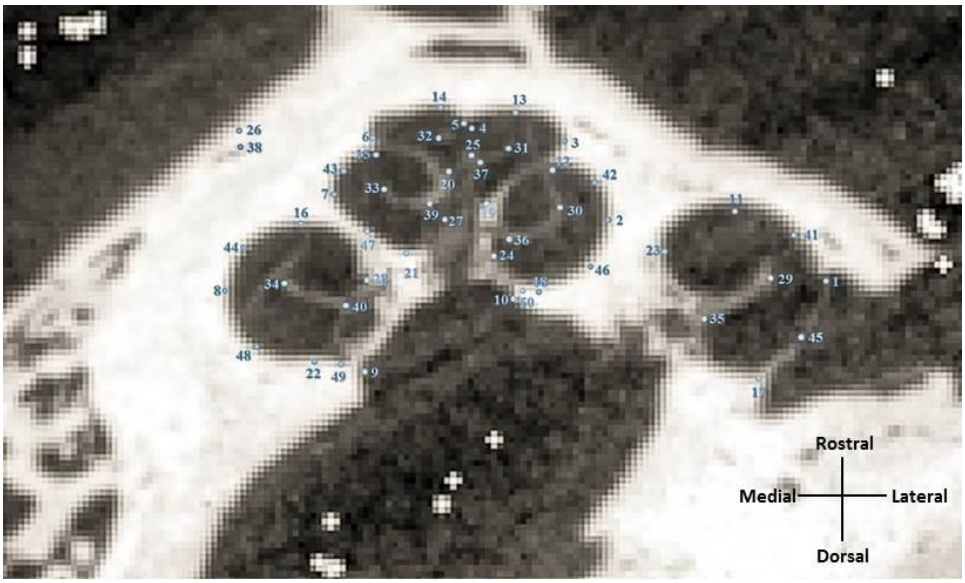

Figure 3.2. The identification and placement of the landmarks are shown on a µCT scan. Landmarks that were not visible on the scan were placed outside the frame of the scan.

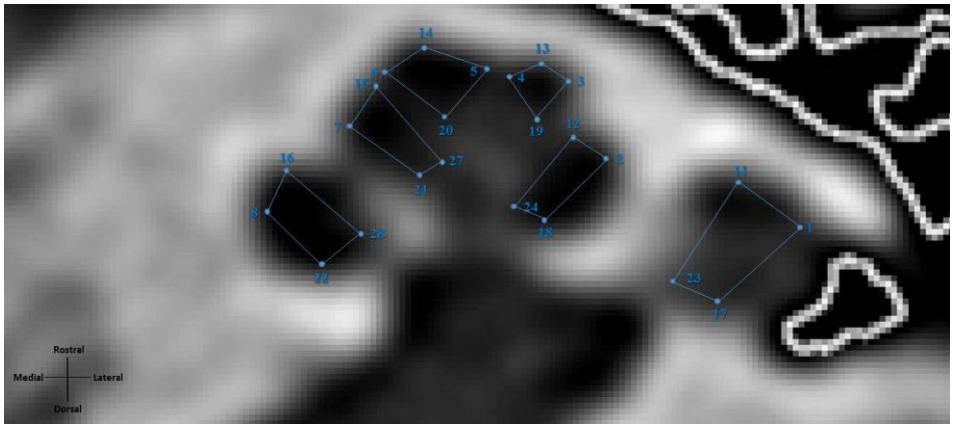

a.)

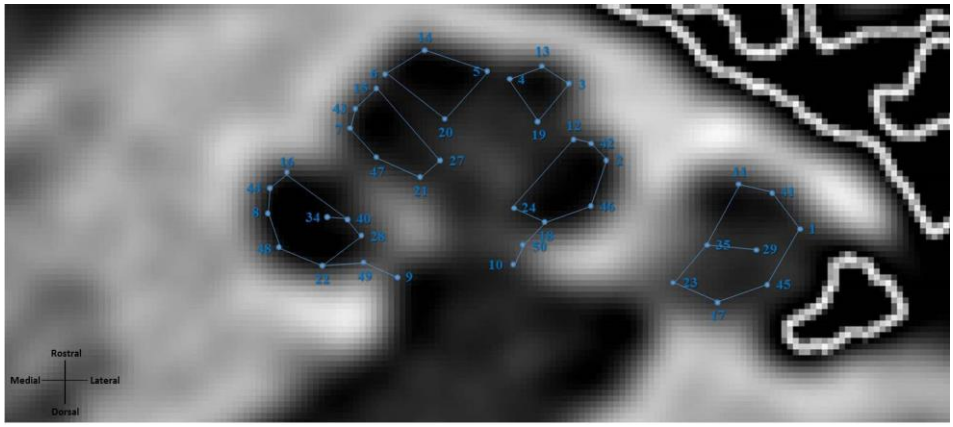

b.)

Figure 3.3. A CT scan with (a) a sparser and (b) larger set of landmarks shows that more landmarks describe form better.

3.3.2.4 Determination of angular lengths

VGStudioMAX-2.2 visualization software (Volume Graphics GmbH, Heidelberg, Germany)[1] was used for the 3D reconstruction of the µCT and CT scans. The angular length (AL) i.e. the number of turn was determined using the method of Shin *et al.* (2013) where the angle (yellow) is determined by drawing a line from the RW (purple) to the terminal point of the cochlea (demonstrated by the blue line) and another line from the central axis cochlea to the helicotrema (demonstrated by the green line) is determined as demonstrated in Figure 3.4.

VGStudioMAX-2.2 visualisation software (Volume Graphics GmbH, Heidelberg, Germany)[2] was used for the 3D reconstruction of the µCT and CT scans. The angular length (AL), i.e. the number of turns, was determined using the method of Shin *et al.* (2013), where the angle (yellow) is determined by drawing a line from the RW (purple) to the terminal point of the cochlea (demonstrated by the blue line) and another line from the central axis cochlea to the helicotrema (demonstrated by the green line) is determined, as demonstrated in Figure 3.4.

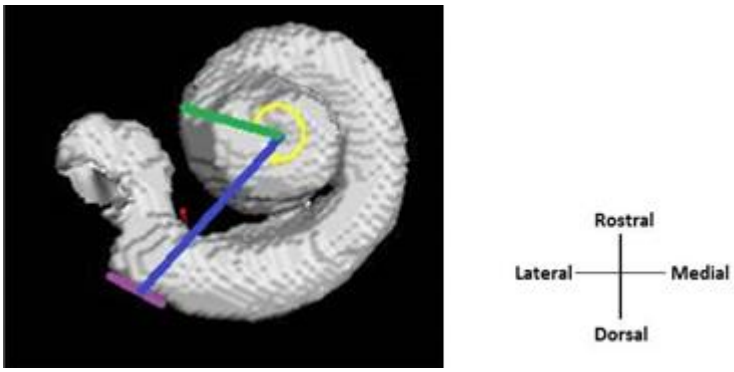

Figure 3.4. Method for determination of the angular length

3.3.2.5 Data processing and analysis

Data processing was performed by a custom script that extracted the radius, height and angular location of landmarks initiated by importing the landmarks (the radius, height and

[1] www.volumegraphics.com
[2] www.volumegraphics.com

angular location) into Matlab[1] (Mathworks). A script `UPCochlea.m` was initialised through custom-made Matlab[2] (Mathworks) scripts and functions for the extraction of data points, classification of cochleae, polynomial equations and cylindrical data points that describe the cochlear geometry. Data processing was initiated by importing the raw landmark data into a custom Matlab[3] (Mathworks) script for subsequent processing.

The first step involves importing the raw measured data, and defining the image scale factor and angular extent of the measured cochlea into the `UPCochlea.m`[4] script. Plots for the visualisation of the raw radial and raw height data of each spiral and up to where each spiral was detected were generated. The script allows the data to be flipped to ensure that the orientation of the cochleae all correspond. Such a standard convention is required so that the spirals can be visually compared among cochleae. Furthermore, outliers (if any) can be identified in the graphs and manually excluded. The cochlea is a rotational structure and data points were measured up to 180^0 on both sides of the modiolar axis. To align the landmarks for each spiral, modiolar stitching was needed for continuity of the measured landmarks. The location of the modiolus was algorithmically detected and the data were offset along this axis to provide a continuous radial trajectory. The height data were continuous as measured as these data are measured along the modiolar axis.

Modiolar correction was based on an LMS fit of the radial data of the LS with an exponential fit through this dataset. The entire dataset was iteratively rotated in the YZ and XZ directions to optimise the LMS cost function. The data were padded to account for missing landmarks that could not be measured. A moving average interpolation was used to fill missing internal points, while the nearest-neighbour method was used to extrapolate missing data points at the apical end of the spiral. Data alignment and modiolar axis correction are necessary for

[1] www.mathworks.com
[2] https://www.mathworks.com/
[3] https://www.mathworks.com/
[4] The `UPCochlea.m` script is used to prepare and standardize data of an individual cochlea for inclusion in the CSRF.

the classification of cochleae as rollercoaster, sloping or intermediate taxonomy, depending on the location of dips, peaks and vertical jumps in the vertical profile of the cochlea. To construct each cochlear spiral, a sixth order polynomial function was fitted on the radius (R) as well as the height (Z) data[1] over an AL of 900^0. The polynomial fit was performed against a scaled abscissa coordinate, i.e. (angle-mu1)/mu2 where mu1 is the mean of the angle over which the polynomial was fitted and mu2 is the standard deviation of the angle over which the polynomial was fitted[2]. Sixth order polynomial equations corresponded well with the radial and height trajectories of the spirals.

The final steps involved the visualisation of data by plotting each data set three-dimensionally as a wire framework that outlines each of the anatomical structures. The conversion of each data matrix into cylindrical polynomial coordinates and polynomial coefficients that describe each spiral of each cochleae was exported for further processing. The process is summarised in Figure 3.5.

The processing performed by the script (`UPCochlea.m`) comprise extraction of data points, classification of cochleae, polynomial equations and cylindrical data points that describe the cochlear geometry.

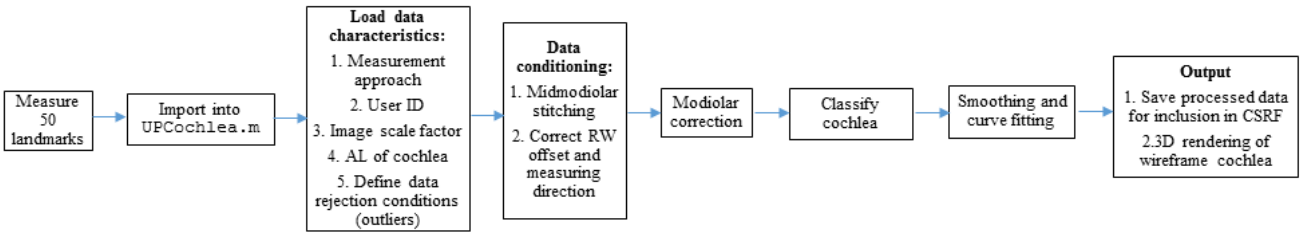

Figure 3.5. Summary of the `UPCochlea.m` workflow

3.3.2.6 Obscured landmarks

In cases where some of the landmarks or cochlear structures are not visible because of poor resolution or because of invisibility to the imaging modality, the study aimed to investigate

[1] The `UPCochlea.m` script allows for the user to choose any polynomial fit order.
[2] https://www.mathworks.com/help/Matlab/ref/polyfit.html

the viability of deriving the location of these obscured landmarks from visible landmarks. The output data from the `UPCochlea.m` script, comprising the sixth order polynomial fits to the radial and height data that describe the trajectory of the LS, MS, SS, IS, SLS, ILS, MSL and LSL of each cochlea were pooled to derive the CSRF using a second custom Matlab[1] script (`Obscured.m`).

First, the radius and height data of each spiral for each cochlea were calculated from the polynomial coefficients derived in `UPCochlea.m`. The mean and standard deviation of each of the spirals for each of the 31 cochleae in the reference µCT image set were calculated. To obtain a polynomial description of the mean of each spiral, the mean of the coefficients that describe the spiral over the cochleae in the dataset is calculated. To obtain a polynomial description of the standard deviation of each spiral, a sixth order polynomial was fitted to the standard deviation as a function of AL to conform with the sixth order fits on the spiral data. This was done for the pooled data set as well as for each cochlear class. Because there is variation in the dimensions of the cochlea among individuals, it is necessary to normalise the mean polynomial description of the spirals relative to a measure that is visible on clinical images. CL was chosen as the normalisation factor for radial data and the height of the LS over 720^0 (LSH) was chosen as the normalisation factor over height. The resulting normalised means and standard deviations form the core of the CSRF.

The predictor portion of the CSRF through which obscured spirals may be predicted was constructed by calculating polynomial equations that describe the location of an obscured spiral relative to a reference spiral. These predictor polynomials are normalised by default since the data from which they were derived were normalised. The predictors, therefore, need to be denormalised when applied to predict an obscured spiral for a specific cochlea, as given in (3.1) and (3.2). Denormalisation factors need to be calculated for a specific cochlea, i.e. CL for radius and LSH for height.

$$Coeff_R = CoeffR_{ref} - ReconCoeffR_{obscured} \times CL \quad (3.1)$$

$$Coeff_Z = CoeffZ_{ref} - ReconCoeffZ_{obscured} \times LSH \quad (3.2)$$

[1] https://www.mathworks.com/

where $Coeff_r$ is the sixth order reconstruction coefficients for the radius, $CoeffR_{ref}$ is the sixth order polynomial fit on the reference spiral data (assumed to be measurable), $ReconCoeffR_{obscured}$ is the normalised predictor coefficients relative to the reference spiral radius and CL is the denormalisation factor for the predictor coefficients. Similarly, $Coeff_z$ is the sixth order reconstruction coefficients for the height, $CoeffZ_{ref}$ is the sixth order polynomial fit on the reference spiral data (assumed to be measurable), $ReconCoeffZ_{obscured}$ is the normalised predictor coefficients relative the reference spiral height and LSH is the denormalisation factor for the predictor coefficients.

The PNMAE between the polynomial fit on the original raw data and the prediction from the CSRF was used to rank the reference spirals according to the accuracy with which they can predict an obscured spiral, as given in (3.3). The error is normalised against CL alone to make the error for radius and height comparable. The PNMAE ranking, as well as the coefficients for the predictor spirals, are presented in Table A.2.

$$PNMAE = \frac{\sum_n \left(\frac{measured - predicted}{CL} \times 100\right)}{n} \tag{3.3}$$

Lastly, a mean template was derived as a function of AL to adjust the relative offset of a predicted spiral, should the spiral prove to be located outside its expected range. All radii in the template were calculated as a fraction of the LS radius using (3.4), while height was quantified as a fraction of the height between the SS and IS, using (3.6).

$$k = \frac{\sum_n^{Rn} \left(\frac{R_{LSL}}{R_{LS}}\right)}{n} \tag{3.4}$$

Therefore, the location of an obscured spiral (of which the shape was predicted through the predictor coefficients as discussed above) relative to the LS can be estimated by (3.5):

$$R_{LSL} = R_{LS} * k\ . \tag{3.5}$$

Template matching for the height data was performed by calculating the average relation between the height of an obscured landmark relative to the height of the IS and the height of the SS relative to the height of the IS, using (3.6):

$$k_Z = \frac{\sum_n^{Zn}\left(\frac{Z_{obs}-Z_{IS}}{Z_{SS}-Z_{IS}}\right)}{n}. \quad (3.6)$$

Thus, an estimate of the location of the height of an obscured spiral relative to locations of the heights of the SS and IS, using (3.7):

$$Z_{LSL} = k(Z_{SS} - Z_{IS}) + Z_{IS} \quad (3.7)$$

The predictors were integrated into the `UPCochlea.m` script to allow prediction of obscured spirals alongside processing of measured data. All the predictors are included and reconstruction of obscured spirals is done in rank order of the prediction accuracy according to the available measured spirals. If, for example, the reference spiral that provides the best prediction was not measured, e.g. ILS, the second-best reference spirals will be used for reconstruction.

3.4 RESULTS

3.4.1 Validation of polynomial fitted data

To validate the dimensions of the analytically described cochleae, a number of measures were derived to allow a comparison with similar measures reported in the literature. This comparison is presented in Table 3.3 below. All measures were derived at the 0° section, i.e. the section that crosses through the RW.

Table 3.3 Comparison of cochlea dimensions in present study (italics) with reported literature

Dimension	Researcher	Method	Population group	N	Results [Mean ± SD (Range)]
Cochlear length	Avci *et al.* (2014)	µCT	German	16	9.20 ± 0.40 mm
	Avci *et al.* (2017)	µCT	German	10	9.35 ± 0.31 mm (9.00 – 10.03 mm)
	Dimopoulos and Muren (1990)	Casts	Swedish	95	8.58 ± 0.45 mm (7.00 - 9.80 mm)
	Erixon *et al.* (2009)	Casts	Swedish	51	9.30 mm
	Escudé *et al.* (2006c)	CT	French	42	9.23 ± 0.53 mm (7.9 - 10.8 mm)
	Fernando *et al.* (2011)	CT	Filipino	38 8	R = 7.55 mm L = 7.60 mm
	Krombach *et al.* (2005)	CT	German	12 0	R = 9.12 ± 0.60 mm (8.10-10.40 mm) L = 9.11 ± 0.60 mm (8.00-10.10 mm)
	Martinez-Monedero *et al.* (2011)	CT	American	12 4	6.80 - 10.30 ± 1.41 mm
	Pietsch *et al.* (2017)	µCT Casts	German	10 8 30	9.30 ± 0.30 mm 9.20 ± 0.40 mm
	Shin *et al.* (2013)	µCT	Korean	39	9.70 mm

	Current study	*µCT temporal bones*	*South African*	*27*	*8.03 ± 1.47 (5.48 – 10.16 mm)*
Width of the basal turn	Avci *et al.* (2014)	µCT	German	16	7.00 ± 0.30 mm
	Avci *et al.* (2017)	µCT	German	10	7.04 ± 0.34 mm (6.71 – 7.63 mm)
	Braun *et al.* (2012)	µCT	German	1	7.70 mm
	Dimopoulos and Muren (1990)	Casts	Swedish	95	6.77 ± 0.35 mm (6.00 - 7.50 mm)
	Erixon *et al.* (2009)	Casts	Swedish	73	6.80 ± 0.46 mm (5.60 - 8.20 mm)
	Escudé *et al.* (2006c)	CT	French	42	6.99 ± 0.37 mm
	Martinez-Monedero *et al.* (2011)	CT	American	124	5.20 -7.80 ± 1.13 mm
	Pietsch *et al.* (2017)	µCT Casts	German	108 30	7.00 ± 0.30 mm 6.80 ± 0.40 mm
	Shin *et al.* (2013)	µCT	Korean	39	7.00 mm
	Current study	*µCT temporal bones*	*South African*	*27*	*6.16 ± 1.09 mm (4.38 – 8.13 mm)*
Width of the middle turn	Braun *et al.* (2012)	µCT	German	1	4.35 mm
	Erixon *et al.* (2009)	Casts	Swedish	73	3.80 ± 0.25 mm (3.30 -4.30 mm)
	Shin *et al.* (2013)	µCT	Korean	39	3.90 mm
	Current study	*µCT temporal bones*	*South African*	*27*	*3.80 ± 0.63 mm (2.61 – 4.80 mm)*
Total cochlear height	Avci *et al.* (2014)	µCT	German	16	4.40 ± 0.30 mm
	Braun *et al.* (2012)	µCT	German	1	4.06 mm
	Dimopoulos and Muren (1990)	Casts	Swedish	95	3.93 ± 0.40 mm (3.10 -5.00 mm)
	Erixon *et al.* (2009)	Casts	Swedish	73	3.90 ± 0.37 mm (3.30 - 4.80 mm)
	Fernando *et al.* (2011)	CT	Filipino	388	R = 4.36 mm (3.30 - 5.10 mm) L = 4.34 mm (3.40-5.20 mm)
	Pietsch *et al.* (2017)	µCT Casts	German	108 30	4.40 ± 0.40 mm 4.00 ± 0.20 mm
	Shin *et al.* (2013)	µCT	Korean	39	3.80 mm
	Current study	*µCT temporal bones*	*South African*	*27*	*5.01 ± 1.01 mm (2.82 – 6.93 mm)*
Height of the basal turn	Braun *et al.* (2012)	µCT	German	1	1.90 mm
	Erixon *et al.* (2009)	Casts	Swedish	73	2.10 ± 0.20 mm (1.60 -2.60 mm)
	Krombach *et al.* (2005)	CT	German	120	1.76 ± 0.03 mm (0.90 -2.20 mm)
	Shin *et al.* (2013)	µCT	Korean	39	1.90 mm
	Current study	*µCT temporal bones*	*South African*	*27*	*R = 3.64 ± 0.55 mm (2.24 – 4.64 mm)* *L = 2.65 ± 0.51 mm (1.53 – 3.92 mm)*
Height of the middle turn	Braun *et al.* (2012)	µCT	German	1	1.30 mm
	Erixon *et al.* (2009)	Casts	Swedish	73	1.20 ± 0.17 mm (0.80 - 1.60 mm)
	Shin *et al.* (2013)	µCT	Korean	39	1.80 mm
	Current study	*µCT temporal bones*	*South African*	*27*	*R = 2.49 ± 0.44 mm (1.57 – 3.65 mm)* *L = 1.94 ± 0.44 mm (1.02 – 3.10 mm)*
Metric length	Erixon *et al.* (2009)	Casts	Swedish	58	42.00 ± 1.96 mm (38.60 – 45.60 mm)
	Erixon and Rask-Andersen (2013)	Casts	Swedish	51	41.20 ± 1.86 mm (37.60 – 44.90 mm)
	Escudé *et al.* (2006c)	CT	French	42	34.40 ± 2.20 mm (30.76 – 37.41 mm)
	Kawano *et al.* (1996)	Histology	Japanese	8	40.81 ± 1.97 mm (37.93 – 43.81 mm)
	Pietsch *et al.* (2017)	Casts and µCT	German	138	36.00 – 46.00 mm
	Sato *et al.* (1991)	Histology	American	18	38.64 ± 3.19 mm (32.70 – 43.20 mm)
	Wurfel *et al.* (2014)	CBCT	German	436	37.90 ± 1.98 mm (30.80 – 43.20 mm)
	Current study	*µCT temporal bones*	*South African*	*27*	*31.40 ± 4.83 mm (23.29 – 39.33 mm)*
Modiolar inlet diameter	Martinez-Monedero *et al.* (2011)	CT	American	124	3.67 ± 0.14 mm (3.42 – 3.82)
	Current study	*µCT temporal bones*	*South African*	*27*	*1.92 ± 0.72 mm (0.79 – 3.17 mm)*
Angular length	Biedron *et al.* (2009)	Histology	German	157	2 < 2.50 54 = 2.50 84 > 2.50 and < 2.75 17 > 2.50 and < 3.00
	Erixon *et al.* (2009)	Casts	Swedish	73	2.60 turns (2.20 – 2.90 turns) /929° (774° – 1 037°)

	Fernando *et al.* (2011)	CT	Filipino	19 4	179 = 2.5 turns 15 = 2.75 turns
	Kawano *et al.* (1996)	Histology	Japanese	84	2.69 ± 0.11 turns
	Pietsch *et al.* (2017)	Casts µCT	German	10 8 30	965.00 ± 40.00º 976.00 ± 45.00º
	Shin *et al.* (2013)	µCT	Korean	39	2.54 ± 0.09 turns (2.36 – 2.80 turns) / 850.70° (916.20° - 1 007.70°)
	Tian *et al.* (2006)	Histology		9	6 = 2.5 3 = 3
	Current study	*µCT temporal bones*	*South African*	*27*	*991.48 ± 44.20º (912.00 – 1078.00º)*

n: Sample size SD: Standard deviation µCT: Micro Computed Tomography CT: Computed Tomography
R: Right L: Left

3.4.2 Cochlear reference spiral framework: mean spirals and standard deviations

Table 3.4 shows the frequency of a particular cochlear class within the dataset used to construct the CSRF. Figure 3.6 shows the a.) radius and b.) height of the LS for the pooled data as well as for data pooled over the different classes. Note the characteristic trajectories that the mean height curves (red) display, which distinguish the different classes from one another.

Table 3.4. Distribution of cochleae (n = 27) among classes

	Rollercoaster	**Intermediate**	**Sloping**
Frequency	13	10	4

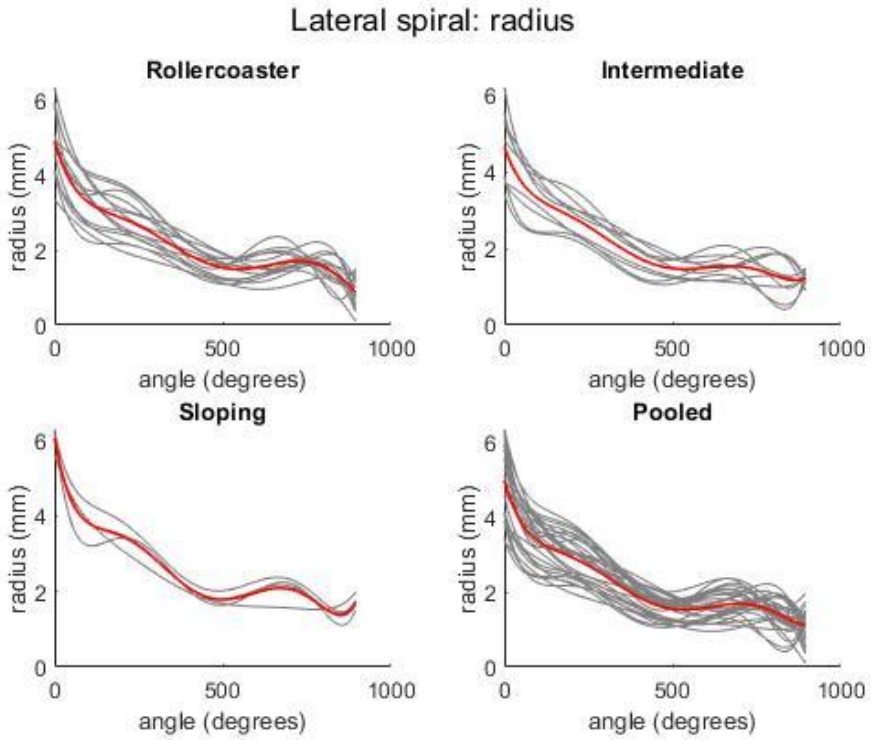

a.)

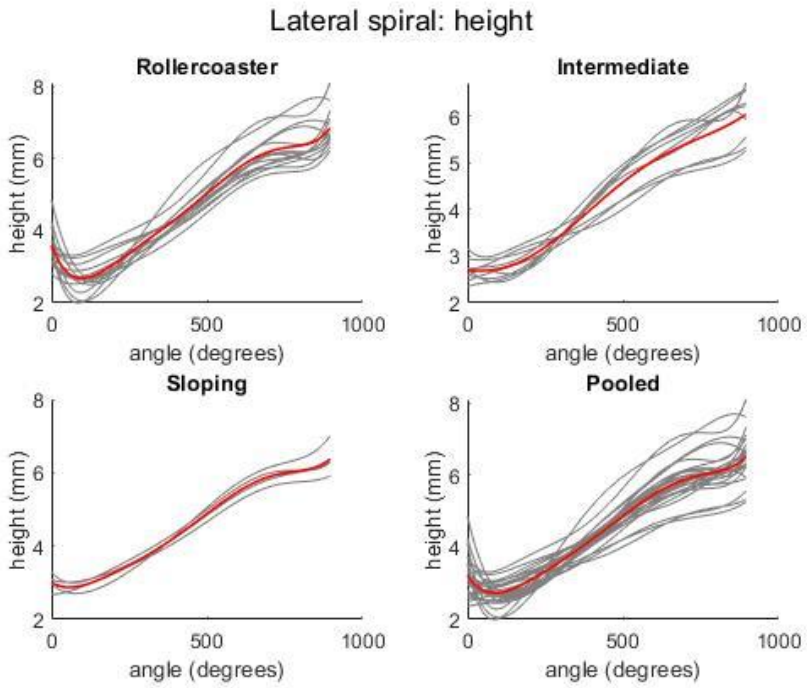

b.)

Figure 3.6. The graphs represent the polynomial fits for the measured LSL of the a.) radius and b.) height for each cochlear class and the pooled data. The red line represents the mean.

Examples of 3D wireframes based on the polynomial equations that were fitted to the raw measurement data are presented in Figure 3.7.

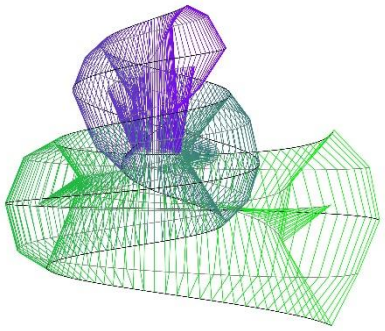

a.)

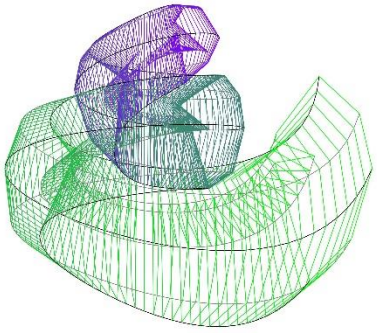

b.)

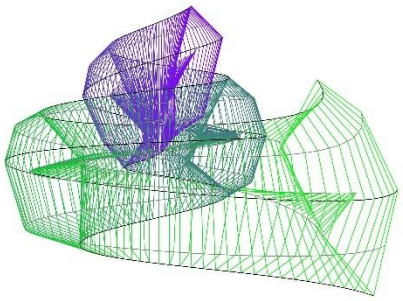

c.)

Figure 3.7. Examples of the 3D generated wireframe representations of a.) sloping, b.) rollercoaster and c.) intermediate cochleae.

Table A.1 presents the polynomial coefficients that describe each mean normalised spiral, as well as the standard deviation for the pooled, roller coaster, intermediate and sloping datasets. The pooled reference data would be applicable if the taxonomy of the cochlea is unknown, while the classified references may provide a better framework for cochleae where *a priori* knowledge of the characteristics of the vertical trajectory of a cochlea is available. The angular positions of critical changes in the vertical profile of the ST need to be recognised in 3D cochlear modelling, as sudden dips and peaks in the ST profile are likely to influence the position of the electrode array and may lead to insertion trauma if not accounted for. The polynomial plots that describe the radius and height of each spiral are shown in Figure 3.8, with the mean spiral data calculated for the pooled dataset

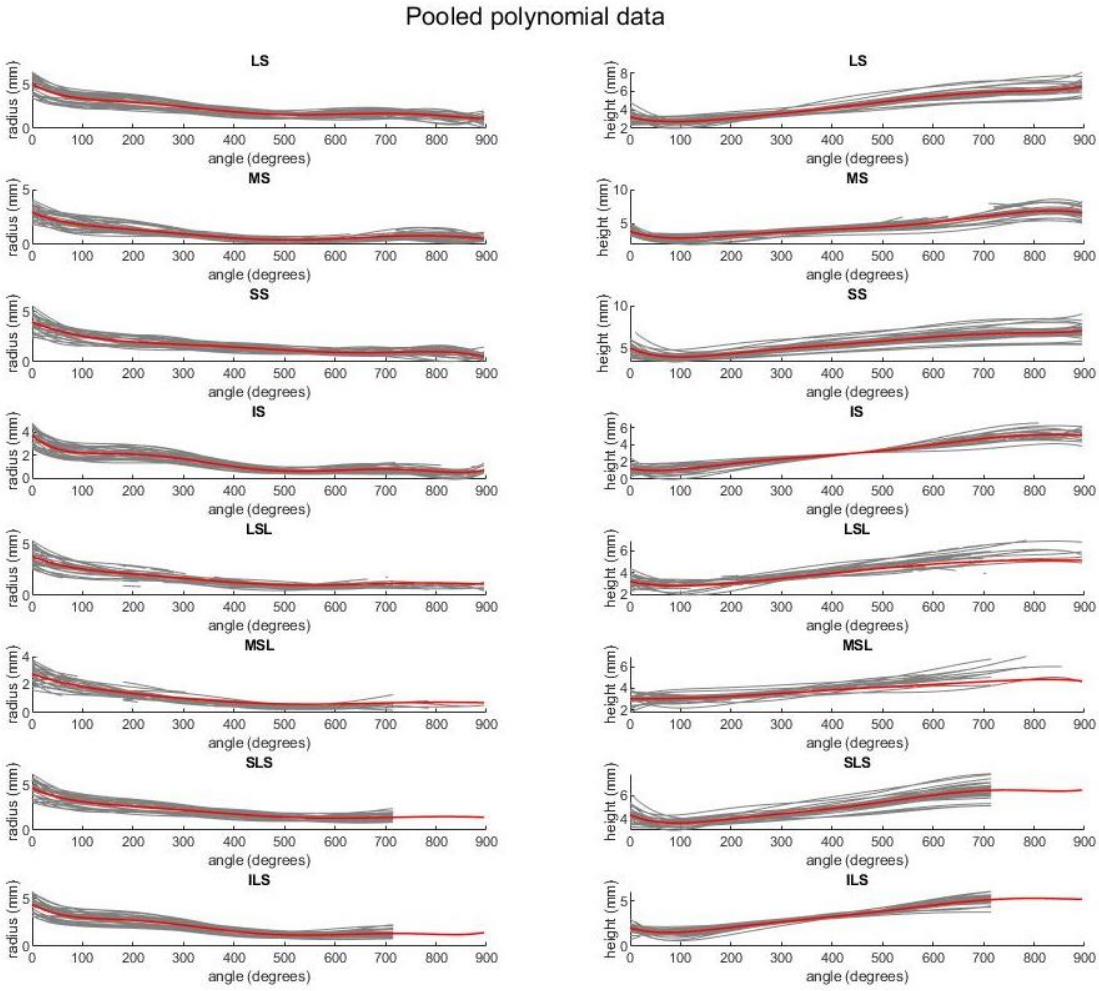

Figure 3.8. Graphs of polynomial equations of the radius and height of the all measured spirals for all the cochleae (n = 27). These spirals were used as reference spirals. The red curve represents the mean of each spiral.

3.4.3 Cochlear reference spiral framework: normalised predictor coefficients for obscured spirals

Polynomial predictor equations for the obscured spirals for each cochlear class and the pooled data from the reference spirals were ranked according to the PNMAE, with a smaller PNMAE suggesting a better prediction. The PNMAE values, rankings and polynomial equations calculated for the first 720º of each cochlea for each class, as well as the pooled data, are presented in Table A.2. Figure 3.9 shows an example of the predicted spirals from the different reference spirals. The thicker plot lines represent points where the original landmarks were measured, while the thinner lines represent angles where the specific spiral could not be measured, i.e. thicker lines indicate the presence of actual measured data that underlie the fitted polynomials and predictions at these angles.

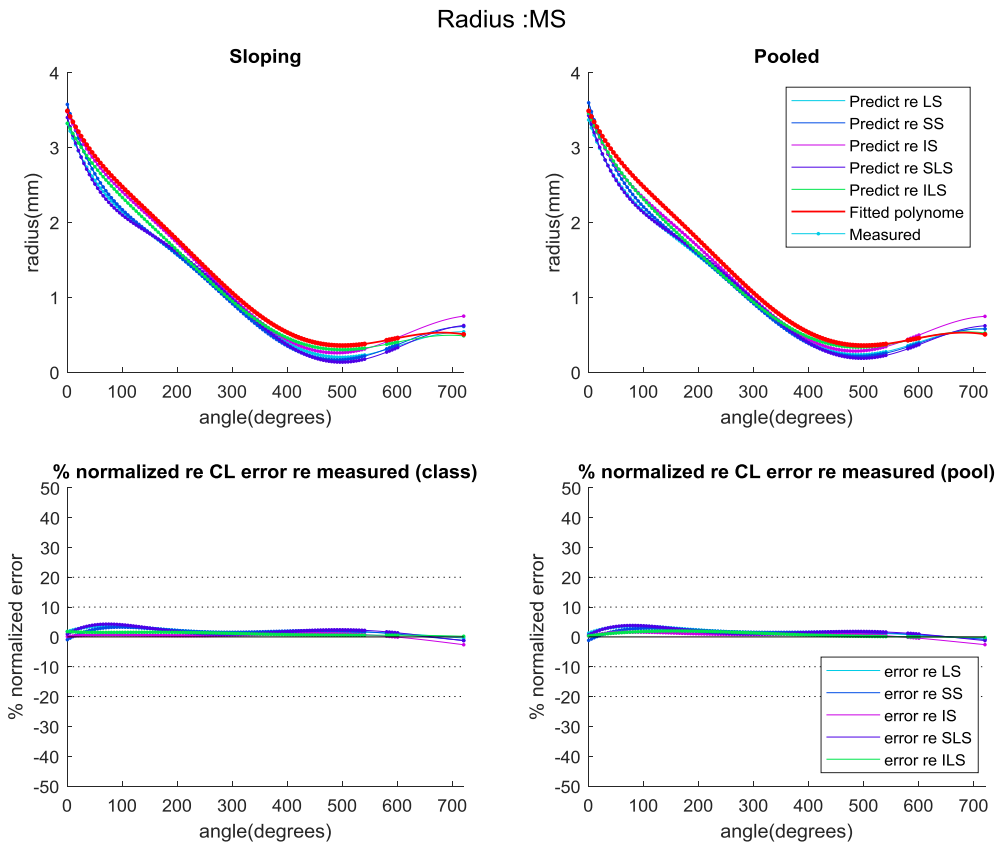

a.)

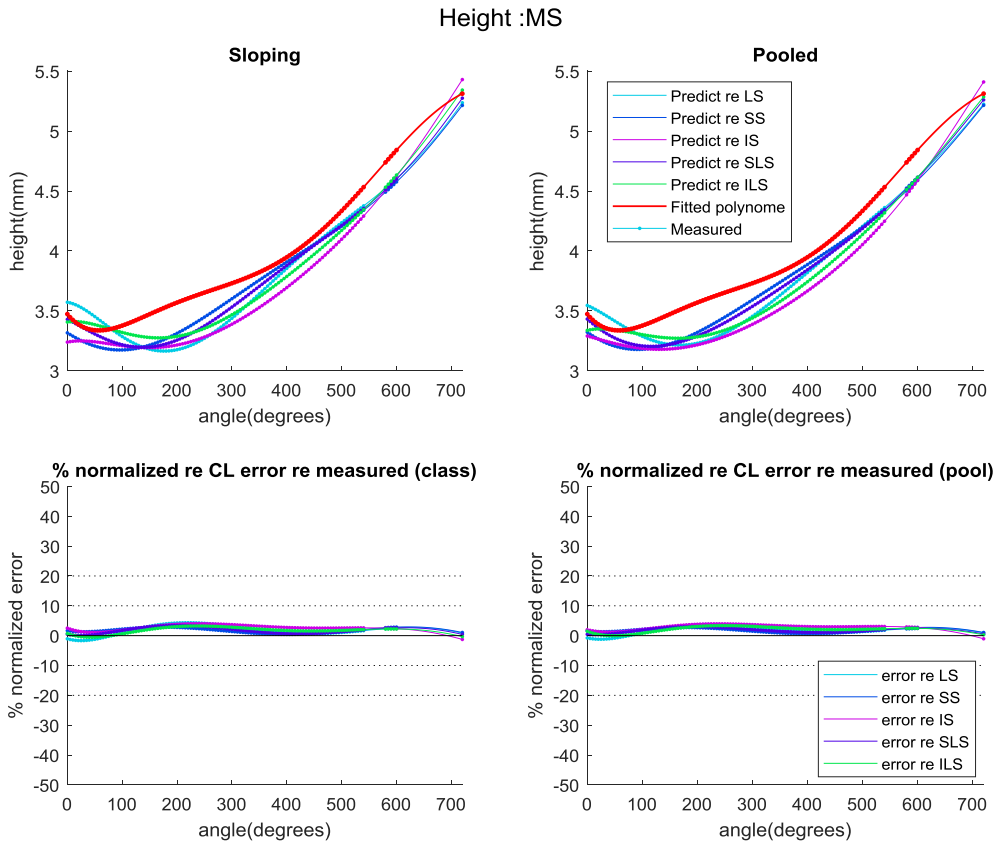

b.)

Figure 3.9. Predicted spirals for the MS for a sloping cochlea a.) radius and b.) height also showing the percentage normalized error (PNE) in the bottom panes.

The PNMAE was calculated by taking the mean of the absolute value of the PNE for each cochlea and calculating the percentage relative to the CL.

3.5 DISCUSSION

This chapter described the construction of CSRF for the reconstruction of cochlear geometry on a user-specific basis for application in 3D computational cochlear models. This study made use of mid-modiolar views of the cochlea to measure a total of 1800 landmarks to describe the cochlear structures. Measured landmarks from µCT scans were used to fit sixth order polynomial curves using a custom Matlab[1] script. Although histological sections

[1] https://www.mathworks.com/

would provide better resolution, mid-modiolar sectioning of a single cochlea at 5º intervals is not possible. µCT scans provide a suitable alternative as the images, next to those of histological sections, are of high resolution.

The method accommodated the inclusion of obscured landmarks that are needed for the development of more detailed 3D computational models of the cochlea by providing a reference framework against which obscured spirals could be predicted. All the cochleae were mirrored or flipped, as proposed by Avci *et al.* (2014), to represent right cochleae for easier alignment and comparison of dimensions. This mirroring procedure does not impose any significant bias on the data (Avci *et al.*, 2014), as previous studies have shown that the dimensional differences between the right and left ears are not significant (Hardy, 1938, Miller, 2007). Cochlear dimensions were derived to compare and validate the method with the available literature (as summarised in Table 3.2.)

3.5.1 Validation of source data

The basic dimensions of the cochlea describe its base width and length and their intersection by the modiolus, as well as angular and metric length and total height (Pietsch *et al.*, 2017). These parameters, which are observable on µCT images, can be used to predict the spiralling trajectory of individual cochleae through parametric models (Frijns *et al.*, 2001b, Hanekom, 2001, Malherbe *et al.*, 2013, Kikidis and Bibas, 2014, Tran *et al.*, 2015, Hanekom and Hanekom, 2016, Kalkman *et al.*, 2016, Malherbe *et al.*, 2016, Wong *et al.*, 2016). The basic cochlear dimensions determined in this study were similar to those reported in the literature (Dimopoulos and Muren, 1990, Kawano *et al.*, 1996, Skinner *et al.*, 2002, Escudé *et al.*, 2006a, Erixon *et al.*, 2009, Martinez-Monedero *et al.*, 2011, Shin *et al.*, 2013, Avci *et al.*, 2014), thus validating the methodology of `UPCochlea.m`.

3.5.2 Visible landmarks

Parametric models of the cochlea, such as the Pietsch *et al.* (2017) model, frequently approximate the cochlear duct with a generic shape, such as a circle. However, a detailed 3D representation of a specific person's cochlear geometry for the purpose of predicting current distributions and the consequent neural excitation characteristics would require an accurate

description of the shape of the cochlear canals. This would include the height profiles of the individual turns, as well as the division of the cochlear duct into the ST and the SV. To translate models into a clinical setting, the algorithms that describe the calculation of obscured landmarks are of great significance.

In clinical settings, landmarks needed for model construction are often obscured, as scans are either of low resolution or contain movement and electrode array artefacts with an additional soft tissue interface that needs to be accounted for. The present study included the parameters that define the medial and lateral-most point of the SL. Superolateral and inferolateral points of the first two turns of the cochleae were also measured to give a better indication of the shape of the outer wall. All landmarks needed to create the LS, MS, SS, SLS, IS, ILS, LSL and MSL were visible on the µCT scans. The `UPCochlea.m` script allowed for the generation of each spiral and therefore the generation of 3D wireframe works of each cochlear geometry.

3.5.3 Taxonomy of the cochlea

The available space that can be occupied by the cochlea is influenced by embryological development, as the cochlear spaces differentiate according to the nervous structures that are present in and around the petrous part of the temporal bone (Raft *et al.*, 2004, Wu and Kelley, 2012). This causes cochleae to have different vertical trajectories owing to the close relation of other structures, i.e. facial nerve, internal carotid artery, internal jugular vein, stapedius and tensor tympani in the petrous part of the temporal bone (Pietsch *et al.*, 2017).

In a study by Avci *et al.* (2014), the vertical profile of 16 µCT scans was calculated. Seven cochleae fell within the rollercoaster class, seven within the sloping and two within the intermediate class. A second study by Pietsch *et al.* (2017) reported that almost half of the cochleae had a rollercoaster profile. The study did not define cochleae of the intermediate class. The authors used fourth order polynomial equations for the radial and third order polynomial fits for the height trajectories of the LS of each cochlea and more robust definitions of cochlear class. The researcher in this project, however, used polynomial fits order to the power of six for both radius and height data, with very precise definitions of cochlear class. This allowed determination of the best fit (especially in the height data) for

each cochlea, in order words the polynomial equations fitted the manually measured data points for each spiral better. This study found eight rollercoaster, ten intermediate and 12 sloping profile cochleae. The scalae in the rollercoaster category had clear dips near the start of the second turn, were smaller in size but taller and more tightly wrapped. Rollercoaster cochleae tended to be prone to cochlear damage, as the CI in such cases would first need be orientated downward and then upward at the point where the cochlea turns to the side, as the sudden dip followed by a vertical jump tends to push the CI toward the BM. Cochleostomies in such cochleae should not be placed too far anteriorly from the RW and deep insertions should be avoided. In cochleae of intermediate and rollercoaster types, there are vertical jumps at the point where the first and second turns are close together and the ST deflects upward, which may cause the electrode array tip to buckle or translocate. In scalae of the sloping category, the cochleae were larger and flatter, and in such cases the electrode array needs to follow the vertical trajectory of the scalae to avoid damage to the BM (Avci *et al.*, 2014, Avci *et al.*, 2017, Pietsch *et al.*, 2017). This needs to be considered when constructing these models and when predictions from the models are interpreted. This is consistent with findings in a study by Pietsch *et al.* (2017), who found that cochlea wrapping is consistent with spatial constraints in the petrous bone.

The PNMAE between the reference spirals and the predicted spirals in this study is low (refer to Table A.1). This indicates that the researcher's predictions are valid. When considering the best reference spirals (according to the rankings given in Table A.2), one can deduce that different reference spirals predict obscured spirals better. This can be ascribed to the fact that cochlear anatomy is variable (Dimopoulos and Muren, 1990, Ketten *et al.*, 1998, Escudé *et al.*, 2006c, Biedron *et al.*, 2009, Erixon *et al.*, 2009, Martinez-Monedero *et al.*, 2011, Avci *et al.*, 2014, Van der Marel *et al.*, 2014, Wurfel *et al.*, 2014, Pietsch *et al.*, 2017).

When referring to cochlear anatomy, one can see that the reference spirals that best predict the geometry of the rollercoaster class follow the dip and peak present in the vertical trajectory of LS. The radius of the rollercoaster category as predictor may be a result of the shorter basal turn and the dip followed by a peak in this class. The distal end of the LSL seems to be angulated inferolaterally, while the medial end or MSL leans in a superolateral fashion. The spirals that predict the spirals of the intermediate class follow the clear vertical jump in the profile of this class. The LSL is angulated superiorly, while the MSL lies

superolaterally. Reference spirals for the sloping class follow a more lateral course, indicating the long basal turn in this class with the turns loosely wrapped. In this class the LSL is angulated inferiolaterally and the MSL trajecting laterally. This has great translational importance in the construction of 3D models, indicating that the MSL changes its course when moving further from the RW.

The polynomial predictions for the height coordinates of each cochlear spiral were less fitted, as can be seen in Figure 3.9. This is intuitive, as the scans are taken in an axial direction while measurements are made in an oblique sagittal view, thus obscuring the landmarks taken in a vertical direction.

3.5.4 Prediction of obscured landmarks

The present study used mid-modiolar sections with a sequence of thin, consecutive orthogonal slices at 50 intervals, which allowed for detailed placement of landmarks. More accurate landmarks could be placed and derived from the µCT images of the dry skulls, as the cochlear boundaries could be better delineated because of less interference from the soft tissue interface and as a result of better image resolution (Hanekom and Hanekom, 2016). Avci *et al.* (2014) showed that µCT allows for higher precision measurements. The cochlear parameters derived from CTs are, however, clinically important, as these are often (other than CBCT and MRI) the only available data from which computational models may be constructed for live CI users. The effectiveness with which the models may be translated to clinical application thus depends on the integrity of such data. Clinically, cochlear dimensions tend to be underestimated by 1.15 mm (Rivas *et al.*, 2017) to 2.34 mm (Demarcy *et al.*, 2016) when deriving the dimensions from CT images.

Algorithms were calculated to derive polynomial equations that describe the trajectories of LS, MS. SS, IS, SLS, ILS, LSL and MSL when only a few parameters are available. It is intuitive that cochleae with obscured landmarks derived from only one visible landmark will generate less user-specific cochleae. It is beneficial to have more measured landmarks available for any measure spiral to account for and correct any offset between the measured spiral and the predicted spiral. Predictions of the cochlear spirals was performed up to 720º,

as CI insertion depth rarely reaches beyond this point and 3D computational cochlear models are constructed up to the degrees mentioned on interest.

Template-fitting of the measured radius and height data of each cochlear spiral resulted in the morphing of the inner structures as well. This provided reference frameworks for the construction of the inner cochlear structures from measured data. Such morphing is important in the context of the refinement of user-specific 3D cochlear modelling, as well as application in the development of clinically available knowledge-based automated landmark models. Template fitting was applied for radial data (R-values) at 0º and for height data (z-values) at 180º. These angles were arbitrarily decided upon to visualise a better fit between the reference and obscured data at the beginning of the cochlear spirals. The `Obscured.m` code does allow for the use of other template angles. Template fitting was used to check whether the predictions were in bound if large PNMAEs were present. In such cases template fitting could be applied to move the reference spiral to the template point.

The position of the inner structures of the cochleae is important in the context of 3D computational modelling of the cochlea. Landmarks that could provide a description of the internal structure of the cochlea, i.e. the separation of the cochlear canal into the SV and ST, and the profile of the medial wall of each turn, are the SL landmarks and the medial-most landmarks of each turn. Even in user-specific cochlear models, a generic template for the determination of the inner cochlear spirals is used and the model outcomes do not explain the variability in psychoacoustic outcomes. By including the inner structures, neural survival patterns and the location of electrode relative to the basement membrane, the DR of CI users can be predicted better. Predictions of the spiral trajectories of each cochlear class are important to include in cochlear modelling, as the occurrence of BM damage and electrode translocation will affect modelling outcomes. This can give one a better understanding of the variability seen between model outcomes and patient outcomes (Ni *et al.*, 2014). Sakellarios *et al.* (2017) presented a methodology to validate the 3D reconstruction of cochlear anatomy, but found similar accuracies to those reported in the literature. The errors reported between model predictions and reality in the literature (Steele and Taber, 1979, Finley *et al.*, 1990, Frijns *et al.*, 2000, Frijns *et al.*, 2001b, Givelberg and Bunn, 2003, Li *et al.*, 2006, Poznyakovskiy *et al.*, 2008, Malherbe, 2009, Noble *et al.*, 2011, Agrawal and Newbold, 2012, Braun *et al.*, 2012, Malherbe *et al.*, 2013, Ni *et al.*, 2014, Aneja *et al.*, 2015, Kang *et*

al., 2015, Malherbe *et al.*, 2015, Hanekom and Hanekom, 2016, Kalkman *et al.*, 2016, Malherbe *et al.*, 2016, Seeber and Bruce, 2016) are larger than those found in this study.

The location of the SL is important, as it gives an indication of the partitions of the cochlear canals. In this study the SL on mid-modiolar sections was mostly seen in the basal and middle turns of the cochlea. In low-resolution scans or obscured scans, which are often found when an electrode array is implanted, the point of the SL can be used to estimate the length of the BM (Erixon *et al.*, 2009, Erixon and Rask-Andersen, 2013, Koch *et al.*, 2017). The width of the BM has been well documented in the literature (Wada *et al.*, 1998, Agrawal *et al.*, 2018). Since cochlear duct length gives an indication of the length of the BM, the measure has important implications for the prediction of place pitch. In the absence of a more proximal measure, such as the distal point of the SL, cochlear duct length may thus be used to estimate the tonotopic coordinates along the length of the cochlea through the Greenwood equation. It is important to note that the terminology used by Pietsch *et al.* (2017) for ML or length along the outer lateral wall does not reflect the length of the OoC or BM when compared to other studies (Kawano *et al.*, 1996). In this study the prediction of the LSL can be extrapolated to that of the known width of the BM from the literature to predict the position of the *stria vascularis*. The position of the RM, which indicates the separation of the SM and SV, can be derived from the lateral-most point of the SL and the superolateral-most point of each turn. The lateral-most points on the SL, together with the lateral-most and superomost points of the turns to describe the size, location and cross-sectional area of the SM and the endolymph as it effects current spread. neural elements relative to the other cochlear structures.

The superior-most, superolateral, medial-most and lateral-most points of each turn with the lateral-most point of the SL give an indication of the size and position of the SV and can be used to derive the cross-sectional area of the SV and the location of the perilymph, as it affects current spread, while the inferior-most, lateral-most and inferolateral-most points of each turn together with the lateral-most and medial-most points of the SL give an indication of the size and position of the ST and can be used to drive the cross-sectional area of the ST and locate the perilymph as it effects current spread. This may lead to more information on cross-turn stimulation leading to perceptual difficulties (Frijns *et al.*, 2001b).

The predictions for the MS were variable for all cochlear classes, as seen in Table 5. The reason for this is that the definition of the medial-most point of the turn did not make provision for placement of this point at the medial edge of the SV and ST. In other words, the landmarks were placed merely where the wall of the turn was medial-most. The medial-most points of each turn give the location of the modiolar wall and thus the location of the surviving neural elements. Medial-most points of the basal and middle turns will provide important information on the location of the modiolus, which is used to determine the distance of the current source from the modiolus.

The PNMAE error for each spiral that was calculated becomes larger as one moves towards the cochlear apex. This can be explained by the fact that fewer landmarks are placed (or placed with difficulty) in the apical turns, as they are small, even on high-resolution data. Fewer landmarks are thus available in this region to extrapolate the spirals from. This may lead one to place a landmark on the edge of the SV or ST. This landmark needs to be investigated, as it is important for the determination of the modiolar wall.

The prediction algorithms for pooled data (i.e. where one does not classify the cochlea) remain valid, as the PNMAE remains small, although data may be skewed as the distribution of each class among the cochleae differs. To improve the reference spirals used for the predictions of an obscured spiral, a more even spread of cochleae between classes is recommended.

The details of the apical turns are not yet a noteworthy consideration in user-specific 3D computational modelling of the cochleae, as the electrode array will not reach the apical turn. Furthermore, the modiolus in the apical regions consists mostly of dendrites, which are often not present in hearing-impaired individuals. When the ILS is obscured, PMAE is high and the researcher suggests that the parameters that describe the ILS be measured manually wherever possible.

Research has also shown that as one moves along the length of the cochlea toward the apex, the cochlear inner structures tend to rotate inwards, towards the centre of the cochlea (Gibson *et al.*, 2012). When using all the landmark spirals, rather than only one, to scale and rotate the template models, details such as the rotation of the cochlear structures along the length of the cochlea become more visible.

3.6 CONCLUSION

A standard set of landmarks was defined and measured on µCT scans, reconstructed into 3D polynomial models using polynomial equations to the power of 6 for both height and radius, and each spiral was normalised and fitted to the same size for comparison. This serves as a CSRF for the prediction of spirals that may obscured. The PMAE values for each spiral were calculated and used to predict obscured spirals from visible landmarks. A standard set of polynomial equations that can be used to determine obscured landmarks in cases of low-resolution scans or owing to blurring caused by an implanted electrode array and that may inform the development of 3D computational cochlear models was proposed. Although cochlear variations and studies on the cochlear shape are well noted, this is the first study of its kind to quantify polynomial equations for each spiral for each type of cochlea and to propose a CSRF that may be used to predict obscured spirals (including an error range). The proposed landmark-based method reduces the complexity required to digitise a specific user's cochlear morphology. It is translational for the *in vivo* reconstruction of human cochleae where only low-resolution images are available, 3D computational model development that includes the inner bony structures of the cochlea, and validation of cochlear models.

CHAPTER 4 WORKFLOW FOR VALIDATING 3D COMPUTATIONAL COCHLEAR MODEL INTEGRITY

4.1 CHAPTER OBJECTIVES

The objectives of this chapter are to apply the CSRF as a tool to quantify the fidelity of either a single user-specific 3D cochlear model or to extend this application to quantify a 3D cochlear model generation workflow or algorithm. The proposed CI model validation workflow (CIMVW) is applied to three variations of a first-generation automated model generation tool, developed at Bioengineering@UP. It is shown that the quality of a model may be quantified according to user-defined criteria. Default criteria are proposed as a standard reference according to which 3D CI models may be rated. This is an important contribution to efforts in 3D modelling of CIs as the CIMVW, firstly, provides a reference to compare the quality of various approaches to generate models and secondly, may also point out strong and weak areas of the model generation strategy.

4.2 ABSTRACT

Automated landmark-based 3D computational models of the cochlea provide an innovative approach to the laboursome process of measuring geometric parameters. The development

of automated model generators is important for the translation of user-specific modelling tools to a clinical setting, as rapid reconstruction of computational CI models is required to service users on demand and outside the scope of a research study. However, automated model generators suffer the same major limitation as manual model construction workflows: low-resolution source image data. Construction of these models is based on a few cochlear landmarks, thus causing lack of morphologic detail. Furthermore, the robustness and subsequent performance of a model generator will depend on the underlying strategy that is employed to extract the geometric information from the image stack. A method that can validate both the approach and individual models that are produced by a model generator could thus be a valuable tool in the development of such models.

Currently, studies on the standardised validation of such models of the cochlea are lacking. The objectives of this chapter are to develop a CIMVW based on the CSRF presented in Chapter 3 and to apply this workflow to a first-generation 3D CI AMG to determine criteria that may be used to quantify the fidelity of a cochlear model and to rate the performance of the model generator through which it was produced. The ability of the CIMVW to inform subsequent improvements to the AMG is investigated. The study employs both µCT and CT scans to analyse the performance of the CIMVW.

4.3 INTRODUCTION

Knowledge-based automated landmark computational modelling of the cochlea is a rapid technique based on pre-defined definitions of anatomical landmarks that are integrated into an algorithm to detect the landmarks automatically. These models need to be accurate and rapidly translated to be of clinical importance and to inform the design, maintenance and troubleshooting of CIs. Currently, studies focus on the results, rather than the design of such automated 3D computational models (Yoo *et al.*, 2000, Yoo *et al.*, 2001, Rodt *et al.*, 2002a, Wang *et al.*, 2006, Hanekom and Hanekom, 2016).

In the literature, automation techniques have been based on selected portions of the cochlea (Rodt *et al.*, 2002a, Wang *et al.*, 2006, Erixon *et al.*, 2009, Noble *et al.*, 2011, Agrawal and

Newbold, 2012, Reda *et al.*, 2014, Aneja *et al.*, 2015, Tran *et al.*, 2015, Hanekom and Hanekom, 2016, Malherbe *et al.*, 2016), not the cochlea as a whole. The reason for this could be the time-consuming nature of the model-generation workflow that relies on various levels of automation and manual techniques to convert anatomical data into 3D geometric entities for simulation purposes (Wang *et al.*, 2006, Malherbe, 2009, Tran *et al.*, 2015).

Although several automation techniques have been published, knowledge-based landmark detection uses predefined or pre-agreed definitions of the landmarks that are integrated into an algorithm. The method is more accurate than other automation methods as proved in a study done by Gupta *et al.* (2015) and Aneja *et al.* (2015), who applied the method to cranio-cephalic landmarks and mouse mandibles, respectively. An accuracy of 90.33% was achieved by Gupta *et al.* (2015). A study by Crous *et al.* (2018) employed a knowledge-based landmark detection technique in the development of a first-generation CI AMG. This AMG was shown to perform reasonably well on a few image stacks that were used to develop the landmark-detection algorithms when compared to manual measurements. However, the generalisation of this AMG has not been investigated and furthermore, there was no method that could be used to quantify the AMG's performance on determining the trajectories of unmeasured (SLS, ILS) or obscured (MS, LSL, MSL) landmarks.

Quantitative studies, which may form the basis for an assessment of model integrity, mostly employ basic linear measurements and angles (Hardy, 1938, Fernández, 1952, Zrunek and Lischka, 1981, Walby, 1985, Ketten *et al.*, 1998, Diamantopoulos *et al.*, 1999, Wysocki, 1999, Skinner *et al.*, 2002, Krombach *et al.*, 2005, Escudé *et al.*, 2006a, Miller, 2007, Connor *et al.*, 2009, Erixon *et al.*, 2009, Biedron *et al.*, 2010, Fernando *et al.*, 2011, Martinez-Monedero *et al.*, 2011, Gunz *et al.*, 2012, Erixon and Rask-Andersen, 2013, Wurfel *et al.*, 2014). These include studies based on high-quality datasets such as µCT scans. A few more advanced analytical methods have been developed to date (Gunz *et al.*, 2012, Johnson *et al.*, 2012, Abdel Salam *et al.*, 2013, Pietsch *et al.*, 2017); however, they are limited in the type and number of landmarks used to describe the complex shape of the inner ear apparatus (Gunz *et al.*, 2012). Extraction of landmark coordinates is associated with some degree of measurement error, which may result from inconsistent tilting of the specimen, non-coplanarity of landmarks or difficulty in pinpointing the landmark locus (Webster and

Sheets, 2010). The measurement error may also be affected by characteristics of the imaging method, e.g. low-resolution CT vs high-resolution µCT images. Absolute measurements may also vary among imaging modalities, e.g. it may be noted for the dimensions reported in Table 3.3 that measurements from CT images tend to be smaller than dimensions measured from µCT images. This is of particular interest in construction of 3D models of live cochleae (cochleae from live CI users), since it might be difficult to gauge the measurement error especially when the scale of the measurements is affected by the imaging modality (Avci *et al.*, 2014, Iyaniwura *et al.*, 2018).

This chapter will aim to develop a CIMVW that will then be applied to a first-generation AMG to provide criteria that would qualify a model or model generator as "good" or "poor".

4.4 MATERIALS AND METHODS

4.4.1 Sample description, orientation and scanning procedures

Twenty-seven dry temporal bones were obtained from the Department of Anatomy, University of Pretoria under the auspices of the National Health Act 61 of 2003. Ethical clearance was obtained from the Ethics Committee of the Faculty of Health Sciences, University of Pretoria (protocol number 174-2013). CT scans were retrospectively collected from seven live cochleae.

4.4.2 µCT of dry skulls and temporal bones and CT of live cochleae

The scanning protocol of the temporal bone samples was discussed in Chapter 3.

CT scans of the live cochleae were retrospectively collected. All the scans were taken at the same facility using a Siemens sensation 64 CT scanner (Siemens, Munich, Germany). The scanning parameters for the live cochleae were acquisition 12 x 0.6 mm, rotation time 1s, pitch 0.8, 120 kV tube voltage. Reconstruction parameters were 0.3 mm reconstruction increment, 90 mm reconstruction FOV and U90u kernel.

4.4.3 Image processing, digitisation of parameters and segmentation

The CT scans were processed in the same way as the µCT scans for Chapter 3 to obtain a set of landmark measurements describing their 3D geometry. The main difference in the outcome was the number of landmarks that could typically be digitised as a result of the poor resolution of the CT images relative to that of the µCT scans. In most cases the MS, LSL and MSL were obscured, especially for cochleae that were implanted with an electrode array. The artefacts caused by the metal electrode contacts frequently obscure most of the internal landmarks and sometimes also distort the location of landmarks that may be routinely visible on pre-operative CTs.

The CT scans were processed in the same way as the µCT scans for Chapter 3 to obtain a set of landmark measurements describing their 3D geometry. The main difference in the outcome was the number of landmarks that could typically be digitised as a result of the poor resolution of the CT images relative to that of the µCT scans. In most cases the MS, LSL and MSL were obscured, especially for cochleae that were implanted with an electrode array. The artefacts caused by the metal electrode contacts frequently obscure most of the internal landmarks and sometimes also distort the location of landmarks that may be routinely visible on pre-operative CTs.

Manual data refinement was necessary, as the image resolution of the CT data was low. Manual data refinement allowed for the reconstruction of high levels of anatomical details as opposed to an automatic approach (Malherbe *et al.*, 2015). Image data of low resolution introduces a significant amount of noise, which may make landmark placement troublesome (Malherbe, 2009, Hanekom and Hanekom, 2016) and may lead to measurement error (Webster and Sheets, 2010). For instance, structures parallel to the modiolar axis were noisy in the direction parallel to the axis, while structures were more easily resolved in a direction perpendicular to the axis. This led to ambiguity in the measurement dimension, necessitating data refinement. Curve fitting on the measurements was employed to correct this ambiguity. In this way the trajectory of a specific landmark along the cochlear spiral can be described. The application of reference spirals on the CT scans without and with an electrode insertion

predicted the trajectory of the obscured inner bony landmarks of the cochlea. In this way the spiral trajectories of the inner spirals could be predicted.

4.4.4 Construction of the CI model validation workflow

The CSRF constructed in Chapter 3 serves as the core of the CIMVW. The first data sets that are constructed for the development of the CIMVW are three variations of the AMG. The AMG searches for the location of the LS, SS and IS on mid-modiolar CT images of a cochlea. It uses a custom-developed pixel-based search algorithm to identify landmarks in a predefined search box. The location of the search box is derived from a knowledge base that contains a template search trajectory for the radius and height of a particular spiral. The mean spiral information captured in the CSRF could serve as this reference. The size of the search box is determined by the standard deviation of the dataset from which the knowledge based CSRF was derived. The standard deviation as a function of CL as captured for each spiral in the CSRF could serve as this reference. The AMG uses pixel values to search for the cochlea and automatically places the SS, IS and LS.

The first-generation AMG (Crous *et al.*, 2018) used a knowledge base that was constructed from a selection of the 31 µCT image stacks that were used to construct the CSRF. This original implementation of the AMG is henceforth denoted AMGO. The complete knowledge base as pooled over the 31 cochleae in the µCT sample (and the basis for the CSRF) was used to create the second variation of the AMG, which is henceforth referred to as AMGP. The third variation was implemented using pre-knowledge of the class of cochlea in the µCT data set and the class parameters from the CSRF were used as the knowledge base to construct the search fields. This version of the AMG is called AMGC.

To create the CIMVW, the main aim was to test how well the AMG data performed against the CSRF. The output of the CIMVW gives a prediction or estimation of how well the AMG model performs.

The CIMVW is broken down into six steps, as described below.

Step 1: Generate spiral data from the model generator or model generation workflow that conforms with the format of the CSRF

The AMG outputs spiral data in Cartesian coordinates. These data must be converted to cylindrical coordinates, i.e. to the radius (R) and height (Z) of each spiral. Furthermore, the spatial sampling resolution of the test and reference datasets needs to be aligned. The AMG outputs 444 data points over 720 degrees. In this study the AMG data were interpolated to values at 5° intervals and the CSRF data were also calculated at 5° intervals.

Step 2: Construct a reference cochlea from the CSRF

The CSRF was constructed over 900°, but was only valid over 720° owing to scarcity of measured data beyond 720°. The reconstructed reference framework for each cochlea over 900° (mu1, mu2) was truncated at 720°. An ideal cochlear reference for each cochlea was reconstructed by:

1) de-normalising the radius of the mean spirals in the CSRF with the CL as determined from the AMG data
2) de-normalizing the height of the mean spirals in the CSRF with the LSH as determined from the AMG data.

If the cochlear class is unknown, the pooled reference spirals from the CSRF are used for reconstruction; if the cochlear class is known, the reference spirals from the CSRF are used for reconstruction.

Step 3: Test the integrity of AMG auto-measured spiral output

The integrity of the AMG spirals can only be tested against measured data in a research setting, i.e. in clinical application manual measurements would normally not be available. In this step the AMG spirals are tested against the reference constructed in Step 2. The percentage of data points that fall within 2σ of the reference spiral is used to discriminate between a “good” and a “poor” outcome. If the AMG auto-measured spirals (LS, SS and IS) pass the integrity test, proceed to Step 4.

Step 4: Generate predicted data for obscured spirals for AMG measurements

Use the "measured" AMG data from step 1 (LS-SS and IS) and process through `UPCochlea.m` script to obtain the predicted values of obscured spirals. Thus, predicted AMG data are obtained.

Step 5: Determine whether predicted obscured spirals from step 4 comply with the reference cochlea criteria; if not, step 3 on the predicted spirals should be repeated. If they do, accept them as the reference to test against for obscured points. If not, retain reference cochlea as reference.

Step 6: Test the AMG-generated obscured spirals against the reference chosen in step 5, i.e. against the CSRF reference spirals or predicted spirals. If the AMG-generated obscured spirals fall within two standard deviations of the reference spirals, the model is valid.

4.4.5 Validation of CIMVW

To validate the CIMVW, the outcome of the AMG was compared to the original measured data. This tested how well the AMG preformed against the measured data.

4.5 RESULTS

The results of the CIMVW are discussed in Sections 4.5.1 to 4.5.6.

4.5.1 AMG performance and integrity (Step 1)

One weakness of the first-generation AMG is that its performance depends on the starting points of the three spirals (LS, SS and IS). These starting points need to be manually placed before the landmark identification algorithm is started. In the present study no optimisation of the starting values of the AMG was performed, i.e. the AMG's performance is assessed without manual intervention to improve its output models. Several cochleae could not be generated from the AMG in this study. Examples of cochleae that could be generated and of

cochleae that could not be reconstructed are given below. This is done to explain the recommended steps for the CIMVW.

Figure 4.1 shows the correspondence of the AMS detected trajectory for the LS, SS and IS (radius and height) with the manually measured data, as explained in step 1. For this particular cochlea, the mean error between the AMG data and the polynomial fit to the manually measured data calculated as a percentage of the CL as determined from the AMG's data is -2.39%, -2.60% and -2.41% for the LS radius for the AMGO, AMGC and AMGP respectively. For the SS radius the mean errors are -2.42%, -3.14% and -2.41% and for the IS radius the mean errors are -4.76%, -5.13% and -4.80% for the AMGO, AMGC and AMGP respectively. For the heights, the errors are -3.87%, -3.26% and -3.96% for the LS, -1.77%, -1.06% and -1.87% for the SS and 0% for three models for the IS. The zero error for the IS is the result of removing the height offset between the measured dataset and the AMG data sets by aligning the mean values of the IS among the data sets. From these predictions, the AMGO and AMGP perform similarly on radius, with the AMGC performing slightly worse, while the AMGC performs better than the other two on the height. This is to be expected, as the class of a cochlea is determined by the height trajectory of the vertical profile of the LS.

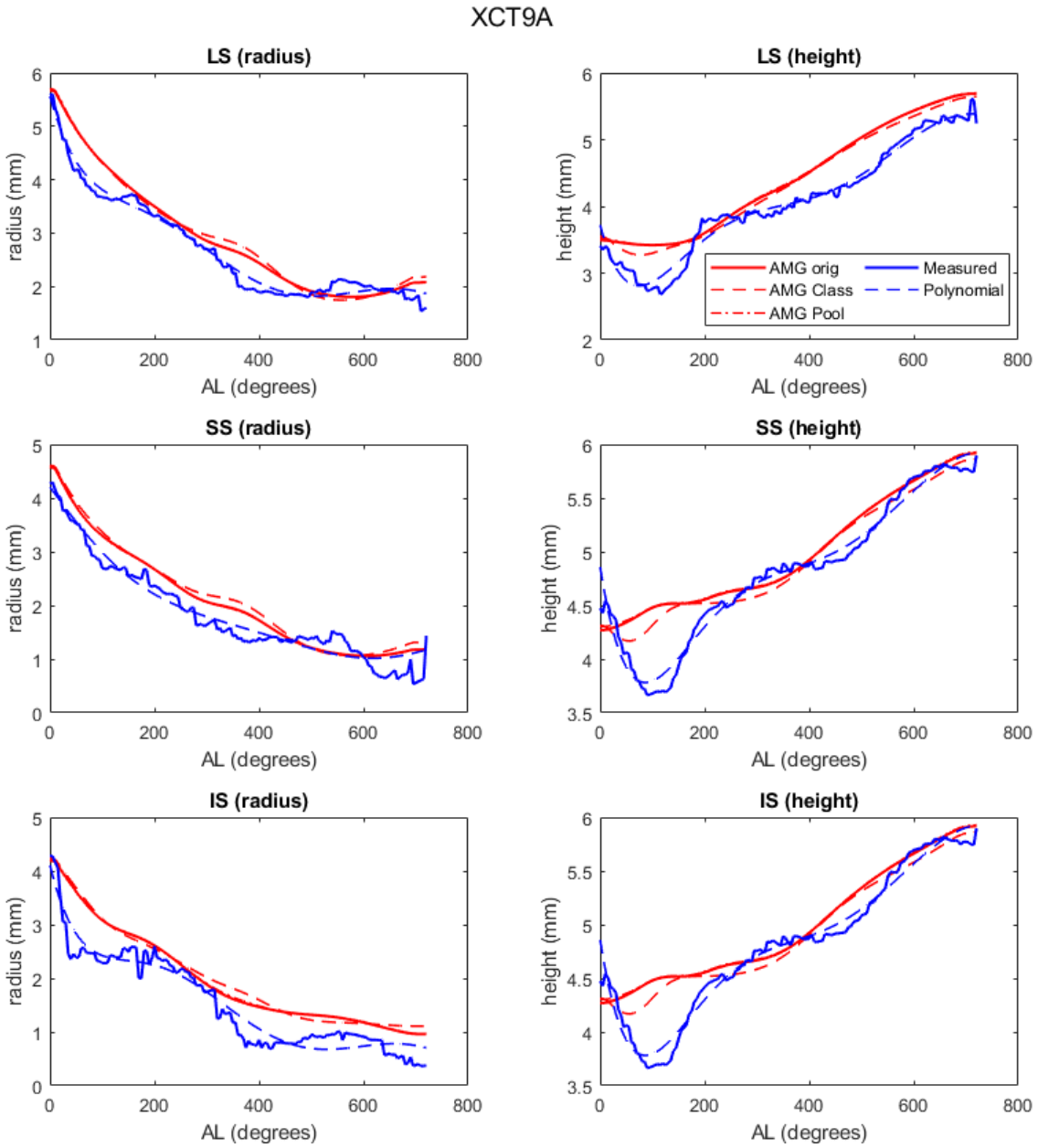

Figure 4.1. Reconstructed spirals for cochlea XCT9A that was successfully reconstructed by the AMG and compared with the manually measured spiral trajectories

Figure 4.2 shows the AMG and measured data for a model that exhibits a scaling problem; the data are given to inform the development of model generators. For this model the errors for the LS height are -10.3%, -14.79% and -15.73% for the three models respectively, while the radius errors for this spiral are -14.62%, -17.83% and -18.58% for the different versions

of the AMG. Figure 4.3 gives an example of a CT scan of a cochlea with a scaling and rotation problem.

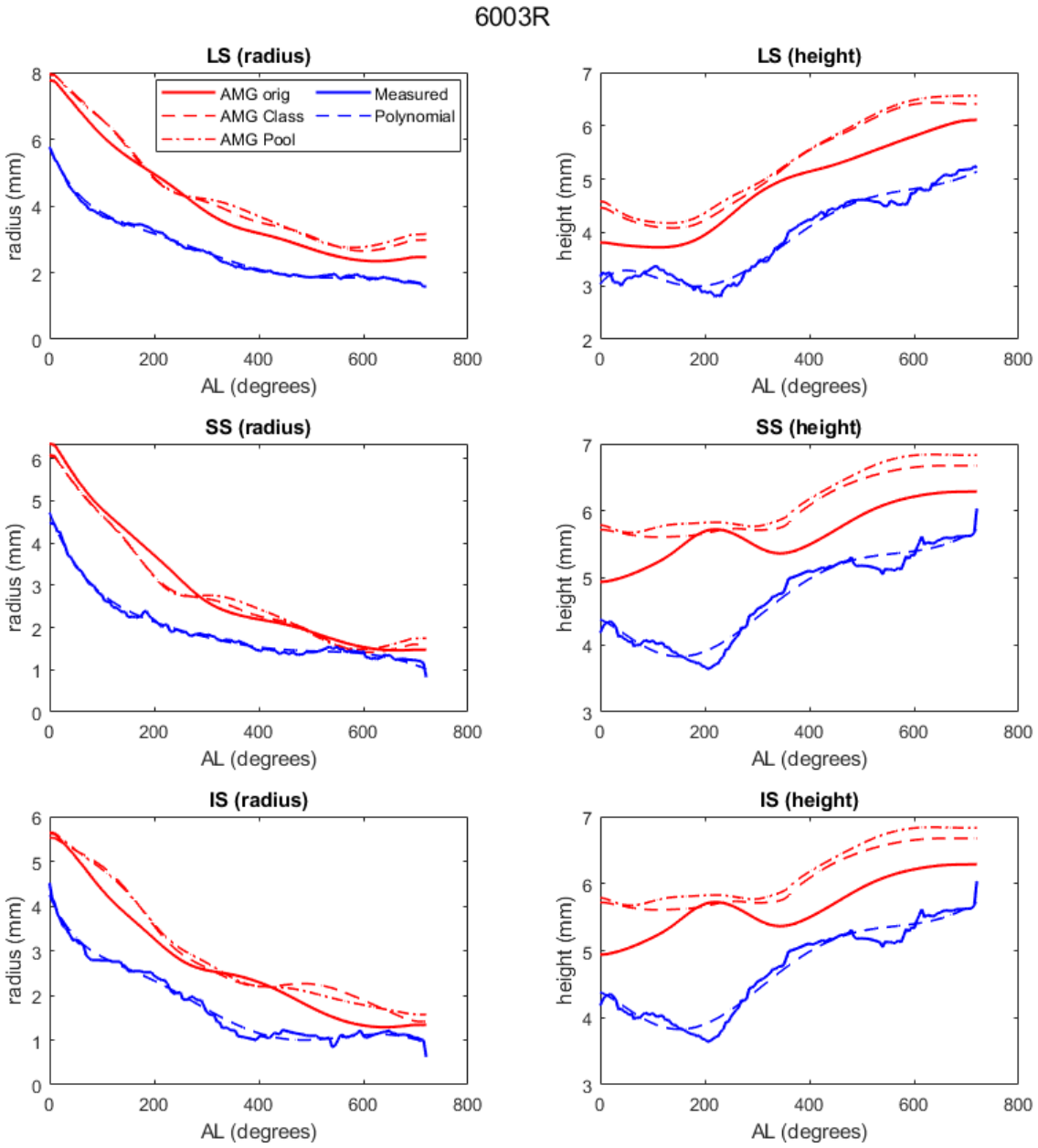

Figure 4.2 Reconstructed spirals for cochlea 6003L plotted with the manually measured spiral trajectories that exhibit a scaling problem

4.5.2 Reconstruction of a reference dataset for a cochlea (Step 2)

The CSRF reference spirals were compared to the AMG to evaluate the fidelity of the LS, SS and SS of the AMG. By doing this, it could determine that the percentage of landmarks

for the radial and height data of the LS, SS and IS fell within 2σ of the reference spirals. Therefore, 95.4% of the landmarks should fall within 2σ of the reference spirals if the cochlea is normal. A plot for each spiral was constructed to determine where the AMG data were erroneous. Figure 4.3 shows an example of a reconstructed CSRF cochlea where the AMG generated data can be seen relative to the reference spirals.

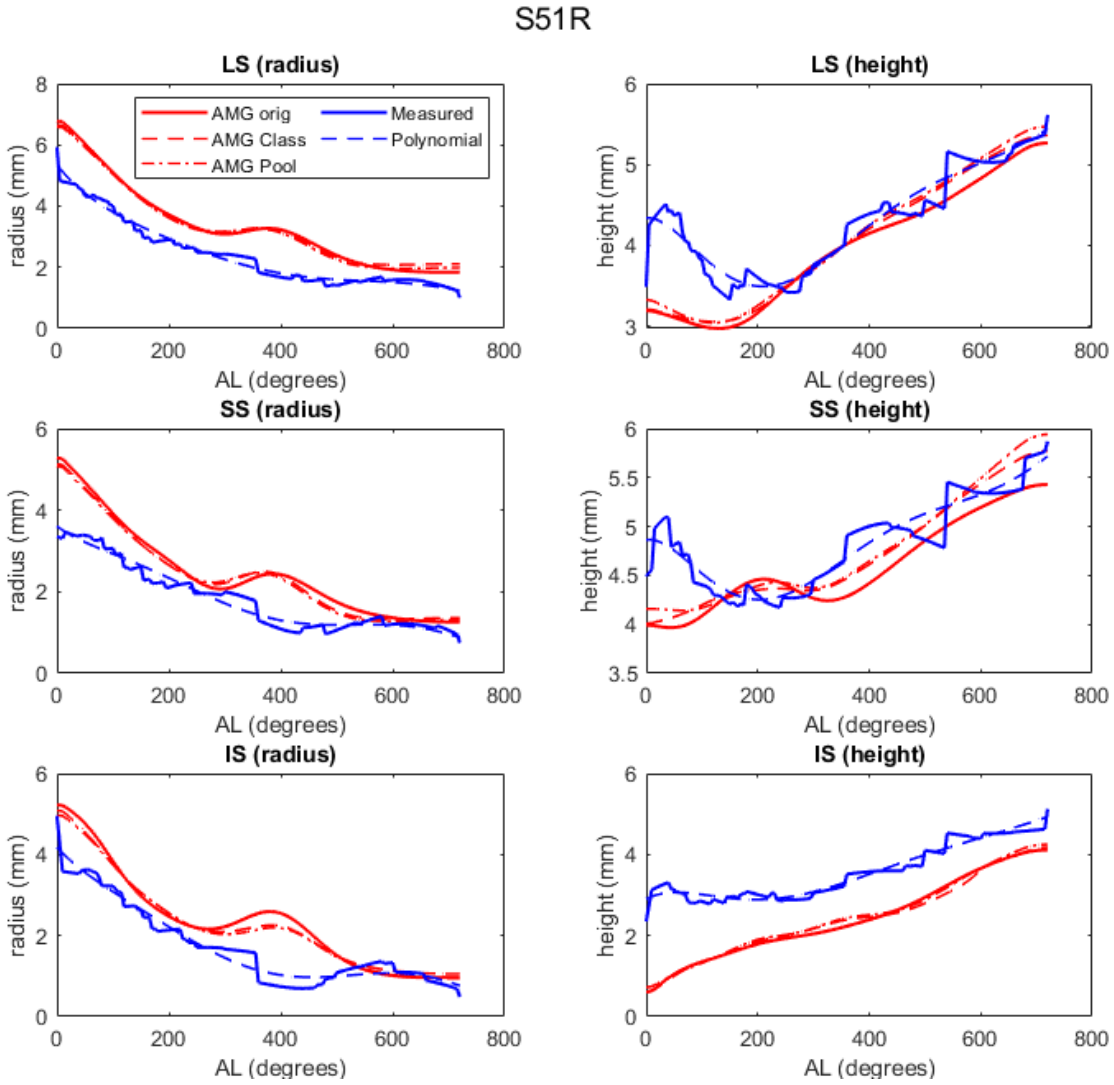

Figure 4.3. Reconstructed spirals for cochlea S51 plotted with the manually measured spiral trajectories

Figure 4.4 demonstrates an example of a reconstructed CSRF cochlea where the AMG generated data did not comply with the CIMVW. Figure 4.5 and 4.6 demonstrates an

example of a reconstructed CSRF of a CT scan of a cochlea where only some of the spirals i.e. LS generated by the AMG generated data complied with the CIMVW.

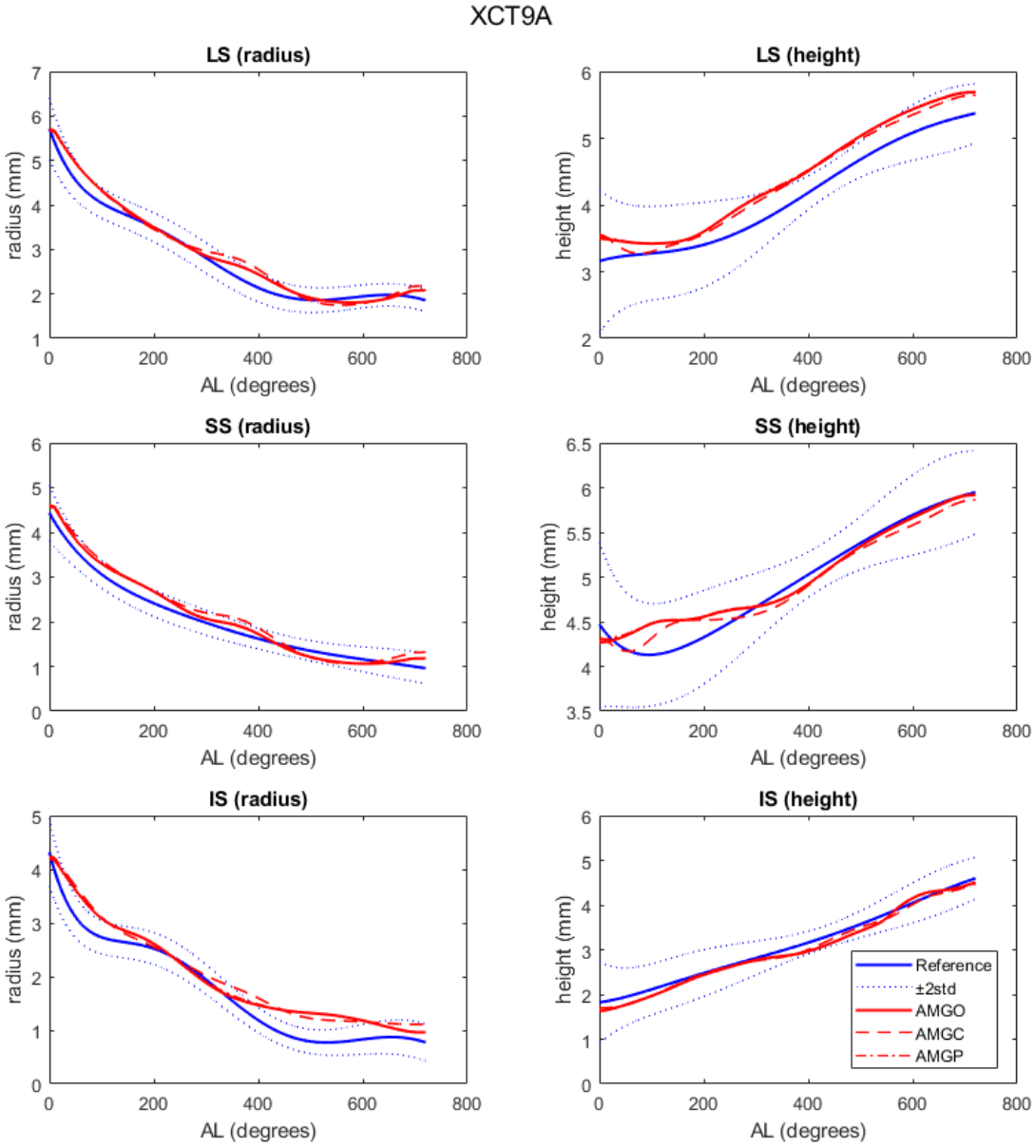

Figure 4.4. Reconstructed CSRF spirals for cochlea XCT9A with 2σ indicated as dotted lines. The AMG measured data are shown relative to the reference.

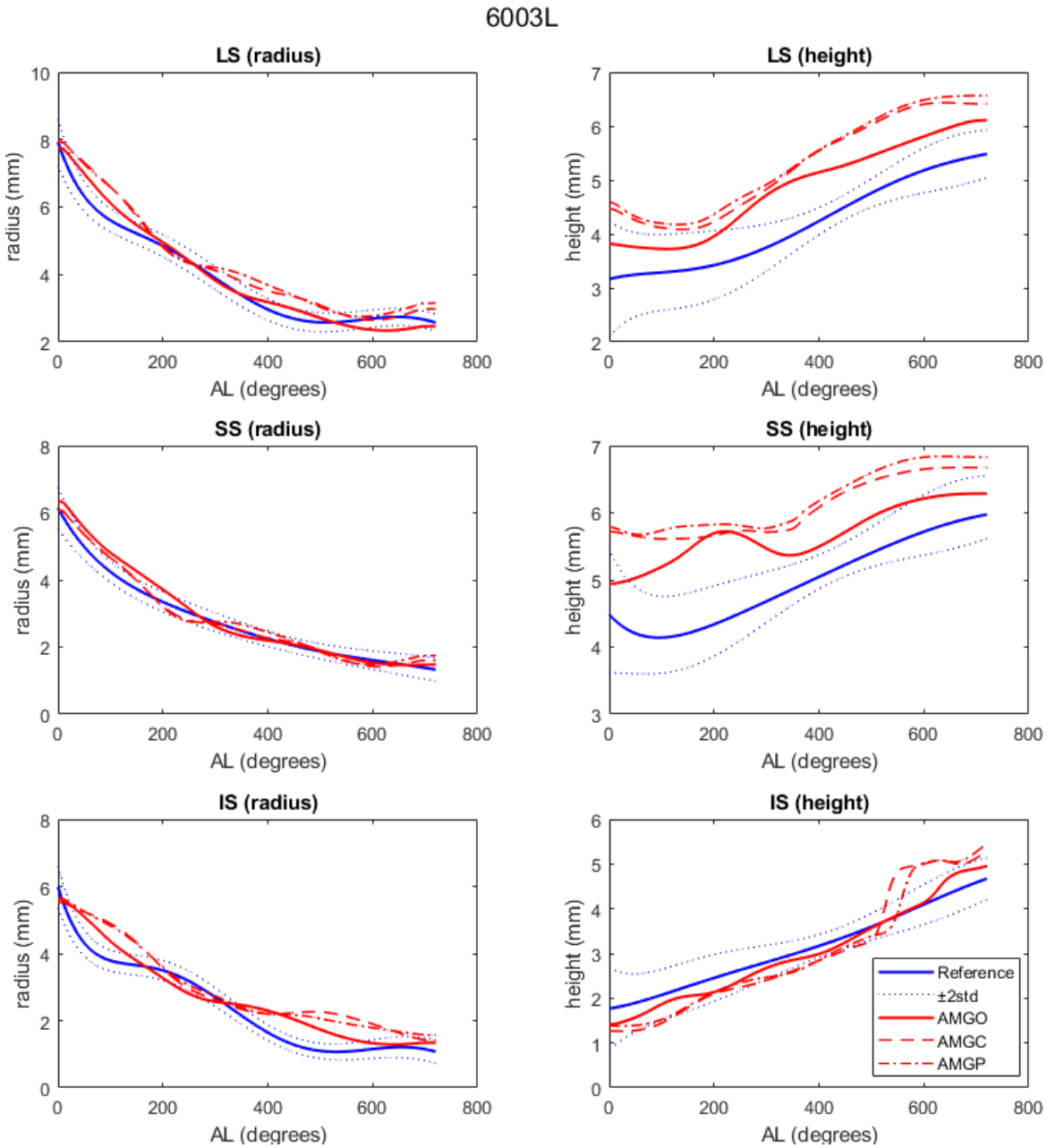

Figure 4.5. Reconstructed CSRF spirals for cochlea 6003L with 2σ indicated as dotted lines. The AMG measured data are shown relative to the reference.

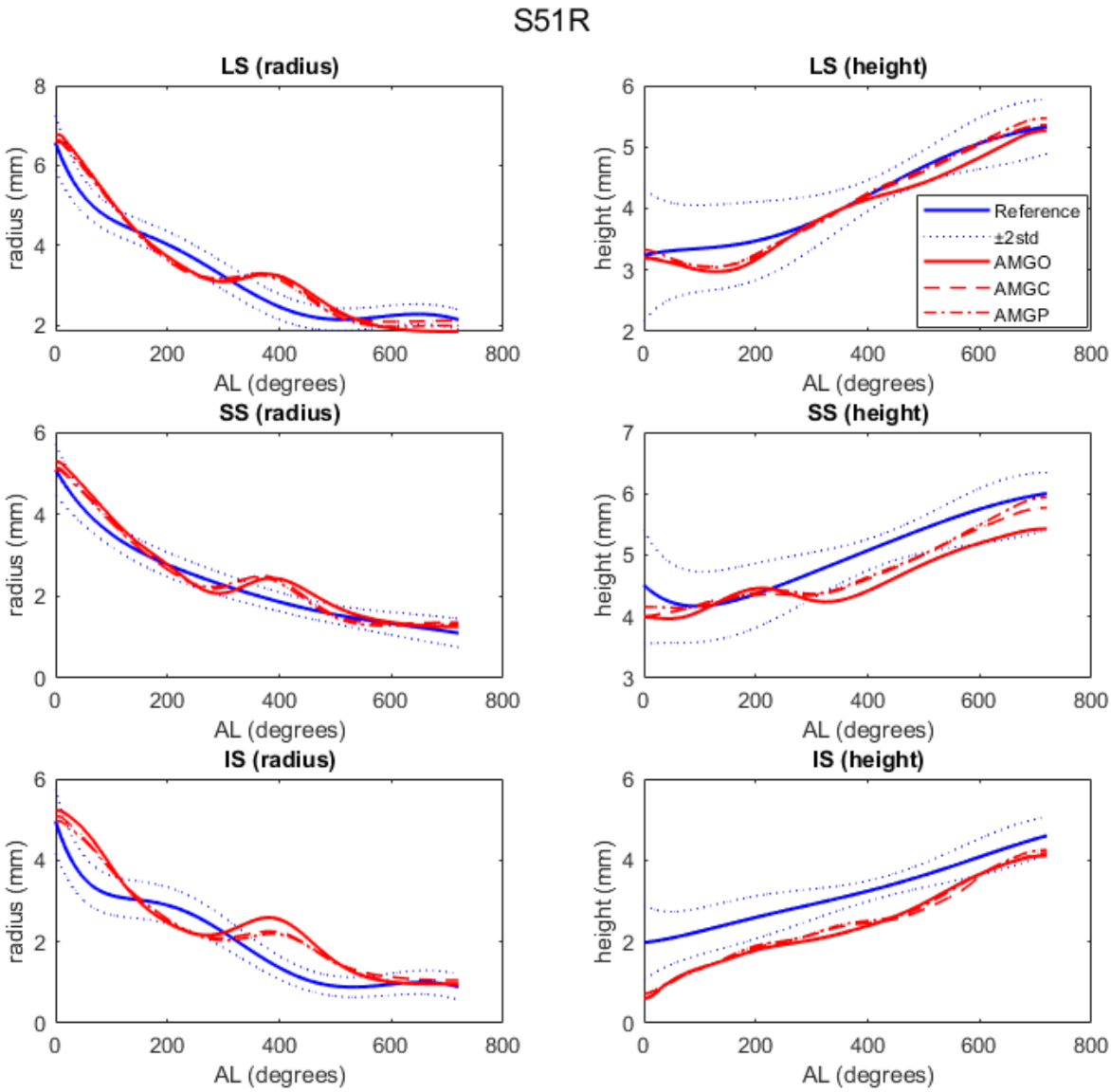

Figure 4.6. Reconstructed CSRF spirals for cochlea CT51L with 2σ indicated as dotted lines. The AMG measured data are shown relative to the reference.

4.5.3 Integrity of the AMG auto-measured spiral output and validation of the CIMVW

The percentage of LS-SS-IS data points of a specific model (AMGO, AMGC, AMGP) that fall within 2σ of the reference spiral used to discriminate between a "good" and a "poor" outcome is given in Table 4.1. This indicates how good the starting points are. In other words, if the LS-SS-IS data points do not adhere to the 2σ rule, the CSRF cannot describe the cochlea accurately. The polynomial data that have been fitted on the measured data can be seen in column four for the pooled data and column eight for the class data. These data demonstrate how many of the unknown cochleae can be described with the CSRF at the beginning of reconstruction. The lowest value for a cochlea reconstructed from µCT data is 80% for the radius (R) and height (Z) on both the pooled and class data. Thus, 80% and more is a good measure to decide whether a cochlea can be described well with the AMG. A criterion of 60% is a fair measure to decide if a cochlea can be described with the AMG.

Radius data for the CT data indicate that only two of the cochleae, which did not form part of the CSRF, performed well against the pooled CSRF and five of the cochleae performed relatively well if a criterion of 60% and more is used. For CT data compared to the pooled CSRF data, three of the cochleae performed very well, while four of the cochleae performed relatively well. For the height (Z) of the CT cochleae, three cochleae performed relatively well against the pooled CSRF, while three of the cochleae performed well and four of the cochleae performed well against the CSRF class data. When considering the measured AMG data, it can be seen that these data do not indicate good performance against the measured CSRF. A "good" model should perform at 80% or more. This table validates the integrity of the CIMVW.

Table 4.1. Percentage of LS-SS-IS landmarks of a specific model (AMGO, AMGC, AMGP) that lie within 2σ within the POOLED CSRF and CLASS CSRF

Measure re CSRF POOLED (LS-SS-IS)				Measure re CSRF CLASS (LS-SS-IS)			
	AMGO	AMGP	PFIT		AMGO	AMGC	PFIT
RADIUS				RADIUS			
XCT9A	89.9	89.9	100.0	**XCT9A**	90.1	71.3	98.2
XCT14A	74.9	75.4	86.4	**XCT14A**	83.2	88.5	80.5
5026R	44.6	46.0	100.0	**5026R**	52.6	44.1	97.2
5056L	36.1	43.7	100.0	**5056L**	40.0	45.3	100.0
6003R	66.9	54.3	93.6	**6003R**	74.3	59.8	93.8
S51R	51.3	63.9	83.7	**S51R**	60.7	67.1	88.7
S52R	31.5	35.6	87.1	**S52R**	37.7	36.6	84.6
S32LP	60.2	9.7	51.7	**S32LP**	66.7	57.2	48.5
S45P	70.8	83.4	36.8	**S45P**	77.0	17.5	32.9
S53R	52.6	41.6	69.0	**S53R**	56.1	35.9	60.9
S54R	30.6	31.7	68.5	**S54R**	32.4	33.3	80.0
S39LP	16.1	15.9	61.4	**S39LP**	17.2	18.4	57.9
HEIGHT				HEIGHT			
XCT9A	75.9	72.4	83.9	**XCT9A**	74.3	74.0	80.0
XCT14A	79.1	79.5	84.1	**XCT14A**	78.9	77.9	86.4
5026R	80.7	83.7	67.4	**5026R**	86.2	79.5	80.2
5056L	59.1	69.0	97.5	**5056L**	63.7	68.3	93.3
6003R	42.5	70.8	94.0	**6003R**	49.2	70.8	100.0
S51R	57.7	61.8	63.4	**S51R**	58.9	64.6	85.1
S52R	69.0	73.3	74.0	**S52R**	73.3	76.1	92.0
S32LP	74.7	50.8	25.5	**S32LP**	79.8	79.8	33.3
S45P	80.2	74.3	56.8	**S45P**	78.9	80.0	55.6
S53R	69.0	76.3	39.5	**S53R**	74.7	86.4	57.0
S54R	50.3	54.3	79.8	**S54R**	53.1	64.1	80.9
S39LP	77.7	73.3	55.6	**S39LP**	84.4	76.8	63.7

4.5.4 AMG data for measured and predicted AMG spirals

The AMG spirals were compared with the measured data and predicted AMG spirals. The results are given in Table 4.2. Here the data are given similar to those of Table 4.1, but are the data measured for cochleae and AMG (the real measures). If the 80% plus criterion is used to evaluate how well the cochleae performed, four cochleae performed well, three cochleae performed relatively well and four cochleae did not adhere to the criteria for the radii of the measured AMG data for the pooled CSRF data. For the height data, seven cochleae performed very well, one performed relatively well and four cochleae failed to adhere to the criteria. When considering the performance of the radii of the measured AMG data for CSRF class, four cochleae performed very well, four cochleae performed relatively well and four cochleae did not perform well. When considering the CSRF height class data,

eight cochleae adhered to the 80% criterion, while five cochleae did not adhere to the 60% or 80% criteria.

Table 4.2. Frequency of how well measured AMG data performed against the predicted AMG data for pooled and class data

	Measure re CSRF POOLED				Measure re CSRF CLASS		
	AMGO	AMGP	PFIT		AMGO	AMGC	PFIT
	RADIUS				RADIUS		
XCT9A	62.6	61.8	92.3	**XCT9A**	62.8	58.2	93.1
XCT14A	59.7	59.7	76.6	**XCT14A**	62.8	64.7	72.8
5026R	45.2	45.1	97.8	**5026R**	49.1	44.2	95.9
5056L	37.5	43.4	78.5	**5056L**	39.0	41.9	80.6
6003R	45.9	37.8	90.4	**6003R**	52.7	43.3	96.4
S51R	47.2	51.6	72.8	**S51R**	53.1	56.6	76.5
S52R	35.5	36.2	81.7	**S52R**	36.9	34.1	78.4
S32LP	49.2	8.9	38.1	**S32LP**	52.7	43.1	38.4
S45P	60.9	64.0	26.9	**S45P**	60.2	21.6	25.5
S53R	47.8	39.3	55.3	**S53R**	49.2	35.1	47.2
S54R	32.5	30.5	71.7	**S54R**	32.5	27.8	75.9
S39LP	15.1	19.1	47.3	**S39LP**	17.8	20.4	46.1
	HEIGHT				HEIGHT		
XCT9A	83.2	81.8	83.4	**XCT9A**	83.9	84.5	84.1
XCT14A	88.0	88.4	89.5	**XCT14A**	88.2	89.0	94.9
5026R	84.7	86.2	85.0	**5026R**	89.1	84.8	83.5
5056L	68.2	80.1	84.6	**5056L**	70.9	75.5	81.9
6003R	47.6	58.5	97.8	**6003R**	51.6	57.7	100.0
S51R	66.2	75.0	75.7	**S51R**	64.8	70.9	88.2
S52R	74.1	79.3	75.9	**S52R**	77.2	81.6	92.0
S32LP	75.0	64.8	26.7	**S32LP**	82.8	83.5	31.5
S45P	88.9	86.1	40.6	**S45P**	88.1	73.9	40.4
S53R	76.5	82.2	52.7	**S53R**	82.2	90.4	59.2
S54R	52.7	62.1	79.3	**S54R**	51.2	62.8	81.5
S39LP	83.0	82.6	49.1	**S39LP**	91.5	86.0	54.1

4.6 DISCUSSION

4.6.1 Recommended workflow for the construction of 3D computational models of the cochlea

Comparison of manual vs automated modelling techniques is well described in the literature. However, such comparisons have been conducted between datasets of the same origin, i.e. CT scans, or focus on measurements of the locations of the electrode array (Noble *et al.*, 2011, Reda *et al.*, 2014, Wanna *et al.*, 2015, Cakir *et al.*, 2016, Rivas *et al.*, 2017). The spirals that are obscured are not included, nor is a standardised reference set. The models given in the literature only include a few landmarks (Avci *et al.*, 2014, Pietsch *et al.*, 2017) of the outer cochlea bony labyrinth and do not accommodate inner bony structures that can be predicted with high accuracy from a high-resolution reference dataset. The CSRF accommodates this gap in the literature.

Although several automation techniques are available, knowledge-based landmark detection uses predefined or pre-agreed definitions of the landmarks that are integrated into an algorithm. An accuracy of 90.33% was achieved by Gupta *et al.* (2015) when comparing landmark-based automated landmark 3D modelling techniques with manual 3D computational modelling of craniocephalic landmarks. The accuracies of the current study could only achieve 80% accuracy. However, craniocephalic landmarks in the Gupta study are of high quality and can be measured manually with ease. The CRSF only used µCTs as baseline, while CTs with and without an electrode inserted were included in the AMG, as these scans cannot be used as baseline for a framework because of the presence of obscured landmarks.

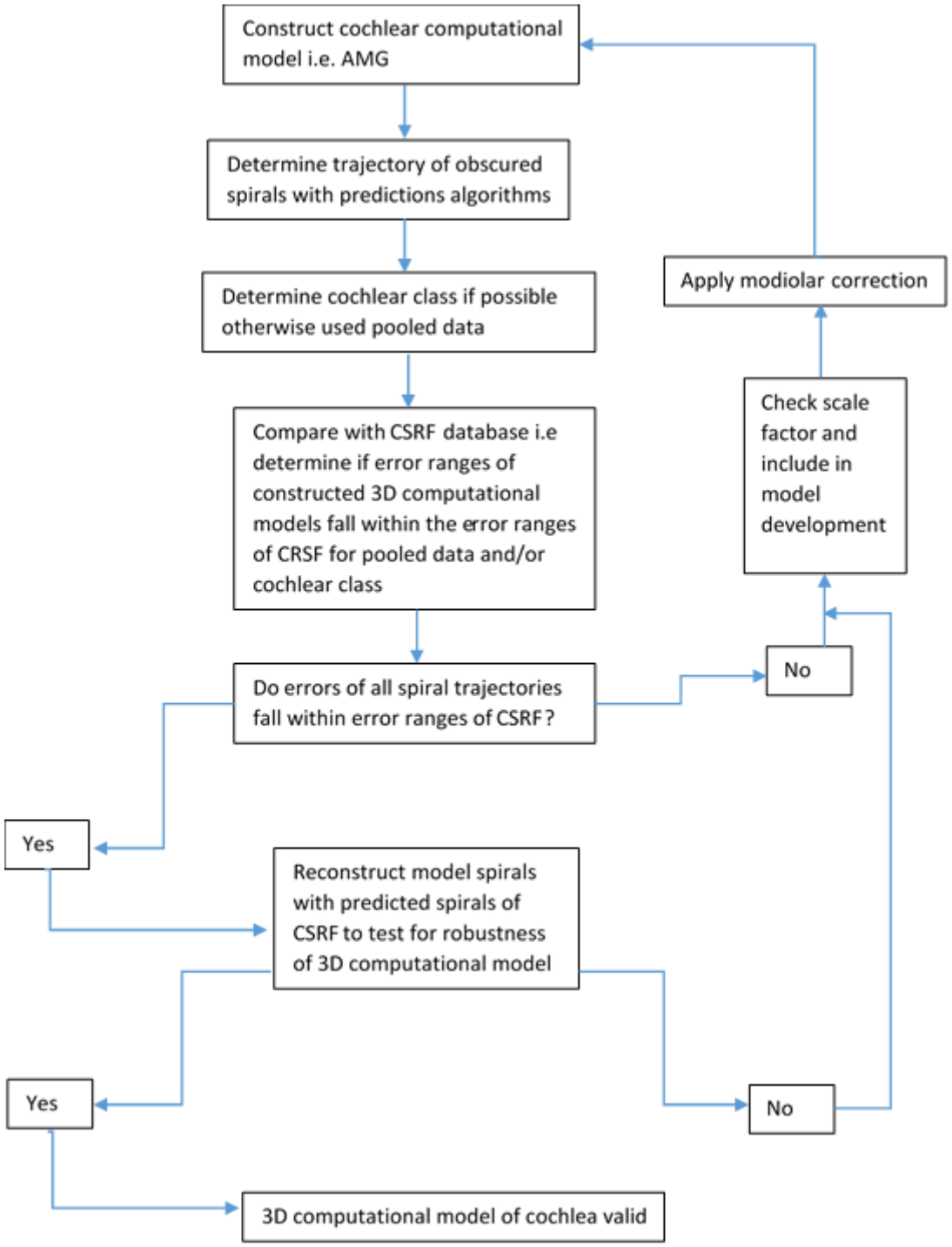

Figure 4.5. Validation of 3D computational models of the cochlea: Workflow to determine robustness and integrity

4.6.2 Validation of process

To the best of the researcher's knowledge, knowledge-based automation detection of cochlear landmarks has yet to be validated against known reference spirals. Even though user-specific 3D computational models are widely used (Briaire and Frijns, 2000a, Givelberg and Bunn, 2003, Malherbe, 2009, Braun *et al.*, 2012, Hanekom and Hanekom, 2016, Kalkman *et al.*, 2016, Malherbe *et al.*, 2016), they lack robustness, need validation and still employ a generic template for the inner cochlear structures.

Through application of the CSRF that includes more landmarks, as well as those of the inner structures (SL and modiolar wall) to the AMG model, one can validate the integrity of the AMG. The output of the CIMVW results in an estimated or predicted model performance. Criteria to determine the quality of the AMG model were more than 80% for "well performing" cochleae, 60% to 80% for relatively well-performing ones and less than 60% for "poorly" performing cochleae. The researcher speculates that these criteria can be improved by including more µCT data that describe more of the cochlear variations for the CSRF. None of the fitted height data for the CT performed well with the pooled CSRF, while only three out of the seven CT cochleae performed well against the class CSRF. The better performance of the height data for the CSRF class provides motivation for the investigation of defining subclasses for cochlear taxonomy. When considering the height data, it performed better on the AMG, i.e. the data were biased. This could be improved by including a larger dataset in the CSRF.

By comparing the measured data, an exact value of how well the CIMVW performs is obtained. The AMG only includes the LS-SS-IS of each cochlea; by including more landmarks that are contained in the CSRF, such as the MS, SLS, ILS, LSL and MSL, the AMG could morph the outer wall as well as the inner bony structures of the cochleae better. These data are validated by the CSRF data. The CSRF was validated by comparing the derived measures of the CSRF with the literature in Chapter 3. The CIMVW was thus validated.

4.6.3 Improving model accuracy

This study obtained a model accuracy of more than 80% for the "well-performing", 60% to 80% for the "fairly performing" and less than 60% for the "poorly performing" cochleae. The cochlea structures produced by the AMG included only the landmarks that define the LS, SS and IS. More accurate model outcomes are proposed by including landmarks that define the SLS, ILS, MSL, MS and LSL. Improving the AMG will produce models closer to the manually measured data. A larger sample size for the construction of the CSRF is recommended as well. The developmental stage of 3D computational modelling of the cochlea is a time-consuming process. This study makes provision for the validation of model integrity against a CSRF and provides ways to improve landmark-based automated computational modelling of the cochlea.

4.7 CONCLUSION

To validate the integrity of 3D computational models of the cochlea, this study found that the following steps should be recommended:

- Predict, if possible, the cochlear class beforehand.
- Orientate the cochleae within a mean (± std) from the reference for the pooled data (if multiple cochleae from different classes are to be modelled).
- Ensure that the scale factor used for each cochlea is correct.
- Employ modiolar correction techniques such as LMS to ensure correct orientation.
- The integrity of a 3D computational model is 80% and more for "well-performing", 60% or more for "fairly performing" and less than 60% for "poorly performing" cochleae.

CHAPTER 5 ANATOMICAL RELATION TO ELECTRODE LOCATION AND PSYCHOMETRIC OUTCOMES

5.1 CHAPTER OBJECTIVES

The objectives of this chapter are to determine if correlations between cochlear geometry, electrode array location, cochlear implant type T-levels and DR exist. In this chapter, the spiral trajectory of the electrode array for each CI user was extracted and compared to electrode location and psychometric outcomes. The CSRF was used to determine the height location of the electrode contacts.

The work presented in this chapter was submitted for publication.

5.2 ABSTRACT

CI users experience great variability in functional outcomes after cochlea implantation. Researchers have investigated many possible reasons for variation in psychometric measures. Individual cochlear anatomy identified to be one of the biggest factors that may influence the degree to which CI users benefit from electrode array insertion. The consequences of variable cochlear anatomy are intuitive as anatomical factors such as individual cochlear length affect the electrode placement, and therefore insertion depth and insertion dynamics of the electrode array, leading to a frequency-place mismatch. Most studies focus on the radial location, i.e. distance from the modiolar wall of the electrode

array. This gives a one-dimensional view of the placement of the electrode contacts. Researchers and clinicians use this measure to determine if the electrode contacts are located in the ST.

The aim of this study is to determine electrode location in two dimensions, by considering the height placement of the electrode contacts. The relation of the spiral trajectory to that of the electrode array was analysed for each cochlear spiral (LS, SS, IS, SLS) and obscured spirals (MS, LSL and MSL) predicted from the CSRF to determine which spiral, if any, may influence the electrode array spiral (ES) and, in turn, psychometric measures.

5.3 INTRODUCTION

The development of user-specific 3D volume conduction computational models of the cochlea that could better estimate the degree to which an individual will benefit from the implantation of specific CI devices has been the focus of many researchers in recent years (Malherbe, 2009, Malherbe *et al.*, 2013, Kalkman *et al.*, 2014, Malherbe *et al.*, 2015, Hanekom and Hanekom, 2016, Kalkman *et al.*, 2016, Malherbe *et al.*, 2016, Nogueira *et al.*, 2016, Seeber and Bruce, 2016). The variables that affect speech outcomes need to be incorporated into these models to understand better why CI users experience variations in threshold levels (T-levels), comfort-levels (C-levels) and DR.

Variables that affect speech outcomes have been ascribed to

i.) factors relating to the patient, such as:
- duration of hearing loss (Gstoettner *et al.*, 2004, Cosetti and Waltzman, 2012, Zohdi *et al.*, 2014),
- time-span after CI insertion (Adunka *et al.*, 2004, Cosetti and Waltzman, 2012, Zohdi *et al.*, 2014),
- prelingual status (Blamey *et al.*, 1996, Rubinstein *et al.*, 1999, Cosetti and Waltzman, 2012, Vargas *et al.*, 2013, Zohdi *et al.*, 2014),
- age at implantation (Clark *et al.*, 2012, Vargas *et al.*, 2013),
- sex of the patient (Sato *et al.*, 1991, Miller, 2007),
- education level (Meneses *et al.*, 2014, Zohdi *et al.*, 2014),
- aetiology (Cosetti and Waltzman, 2012, Zohdi *et al.*, 2014),

- amount of residual hearing present (Rubinstein *et al.*, 1999, Adunka *et al.*, 2004, Gstoettner *et al.*, 2004, Brant and Ruckenstein, 2016, Khoza-Shangase and Gautschi-Mills, 2019) and number of spiral ganglion cells (SGCs) present (Blamey *et al.*, 1996, Incesulu and Joseph B. Nadol, 1998, Khan *et al.*, 2005);

ii.) factors related to the CI, namely:

- surgical approach, insertion depth, insertion angle, type of implant, electrode location (Davis Timothy, Shepherd *et al.*, 1993, Cohen *et al.*, 1996, Dorman *et al.*, 1997, Ketten *et al.*, 1998, Gstoettner *et al.*, 1999, Rubinstein *et al.*, 1999, Friesen *et al.*, 2001, Frijns *et al.*, 2001a, Pfingst *et al.*, 2001, Tykocinski *et al.*, 2001, Husstedt, 2002, Huttenbrink *et al.*, 2002, Parkinson *et al.*, 2002, Saunders *et al.*, 2002, Skinner *et al.*, 2002, Bettman *et al.*, 2003, Briggs *et al.*, 2005, Kós *et al.*, 2005, Mens and Berenstein, 2005, Cohen *et al.*, 2006, Fayad and Linthicum, 2006, Hughes and Abbas, 2006, Stickney *et al.*, 2006, Lane *et al.*, 2007, van Wermeskerken *et al.*, 2007, Finley *et al.*, 2008, Rebscher *et al.*, 2008, Connor *et al.*, 2009, van Wermeskerken *et al.*, 2009, Meshik *et al.*, 2010, Wanna *et al.*, 2011, Nicoletti *et al.*, 2013, Kalkman *et al.*, 2014, Hochmair *et al.*, 2015, Kang *et al.*, 2015, Vermeire *et al.*, 2015, Demarcy *et al.*, 2016, Kalkman *et al.*, 2016, Aschendorff *et al.*, 2017, Büchner *et al.*, 2017, Dhanasingh and Jolly, 2017, Timm *et al.*, 2018, Khoza-Shangase and Gautschi-Mills, 2019) and insertion trauma (Adunka *et al.*, 2004, Wardrop *et al.*, 2005, Biedron *et al.*, 2010, Vargas *et al.*, 2013, Avci *et al.*, 2017).

Of these factors, anatomical inter-individual variations are a fundamental reason for the great variability seen in CI surgery outcomes (Skinner *et al.*, 2002, Erixon *et al.*, 2009, Biedron *et al.*, 2010, Martinez-Monedero *et al.*, 2011, Braun *et al.*, 2012, Shin *et al.*, 2013, Malherbe *et al.*, 2015, Malherbe *et al.*, 2016, Avci *et al.*, 2017). These cochlear variations have been found to influence the location of CI arrays and affect the potential of hearing preservation surgery and in turn speech and hearing outcomes (Rubinstein *et al.*, 1999, Adunka *et al.*, 2004, Gstoettner *et al.*, 2004, Erixon *et al.*, 2009, Cosetti and Waltzman, 2012, Zohdi *et al.*, 2014, Brant and Ruckenstein, 2016, Khoza-Shangase and Gautschi-Mills, 2019). This is intuitive when it is realised that the exact location of the electrode contacts in the cochlea dictates the spread of neural excitation, and thus the perception that may be elicited through electrical stimulation (Hanekom and Hanekom, 2016).

The effect of individual cochlear geometry on the variations in T-level, pitch perception, and DR is well illustrated in a study by Malherbe *et al.* (2016), where the researchers constructed five user-specific cochlear computational models derived from the users' cochlear anatomy. The effects of cochlear geometry were quantified by comparing these to the effect of intrascalar electrode location. Cochlear anatomy affected electrical potential distribution and neural excitation profiles to a similar extent as electrode-modiolar distance. The mean effect of morphology on T-levels between different cochleae was found to be 4 dB, while the mean difference between the T levels of the medial and lateral arrays was 6.4 dB. Variation in the cochlear frequencies as a function of cochlear length for the medial and lateral electrodes was found to be 2.1 and 1.6 mm between users respectively. Spread of excitation also varied between the medial and lateral arrays, with an increase from 4.3 mm (1.0 octaves) for the medial to 7 mm (1.6 octaves) for the lateral arrays 3 dB above T-levels. The increase in spread of excitation 10 dB above T-levels was 9.8 mm (2.3 octaves) for the medial to 14.2 mm (3.3 octaves) for the lateral arrays. This study demonstrated that variations in T-levels, characteristic frequencies and bandwidth resulting from cochlear morphology are almost as large as those resulting from electrode location (Malherbe *et al.*, 2016).

The effect of the radial distance of the electrode array has been well documented in the literature (Saunders *et al.*, 2002, Skinner *et al.*, 2002, Adunka *et al.*, 2004, Wardrop *et al.*, 2005, Biedron *et al.*, 2010, Wanna *et al.*, 2011). However, the effect of the height location of the electrode contacts needs to be addressed, as this may indicate translocation of the electrode array. For this study, live cochleae from CI users implanted with perimodiolar or modiolus-hugging arrays were chosen.

The CSRF in Chapter 3 of this thesis can be used to describe the electrode location in two dimensions (i.e. height and radius) relative to the SS, LS, IS, SLS and MS and to predict the spiral trajectories of obscured spirals MS, LSL and MSL in low-quality scans where an electrode artefact is present. The aim of this study was to investigate which cochlear spiral trajectories could determine the final location of the trajectory of the inserted electrode array and in turn, the psychometric outcomes of CI users

5.4 MATERIALS AND METHODS

CT scans of eight live cochleae i.e scans of CI users implanted with perimodiolar arrays were retrospectively collected. Procedures for the scanning of the live cochleae with electrode arrays are explained in Chapter 4. The psychometric measures T-level, DR and the array type implanted for each CI user from the cochlear database were retrospectively collected.

5.4.1 Image processing

The images were processed as explained in Chapters 3 and 4.

5.4.2 Digitisation of parameters and segmentation

The procedure for the measurement of the anatomical landmarks of each cochlea is explained in Chapter 3. The predefined landmarks are given in Table 3.1. In addition, landmarks for the electrode array were digitised as given in Table 5.1 and illustrated by the red dots in Figure 5.1.

Table 5.1. Summary of the landmarks of the electrode contacts as placed on each 5º slice for each cochlea

Point	Definition
51	Electrode position in right basal turn
52	Electrode position in left basal turn
53	Electrode position in right middle turn
54	Electrode position in left middle turn

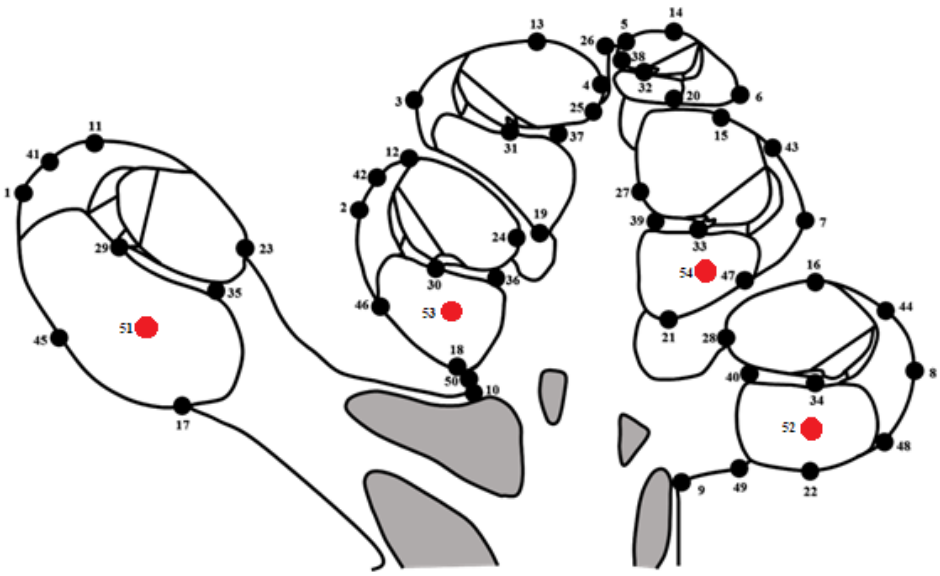

Figure 5.1. Schematic representation of the points that were placed on µCT scans of temporal bones and skulls. Landmarks that were not visible on the scan were placed outside the frame of the scan.

The mapped landmarks were used to define the parameters that describe the spatial relationship of the cochlea in a spiral-like manner, as explained in Chapter 3 and Table 3.2. The landmarks that describe the spiral trajectory of the electrode array were constructed by landmarks 51, 52, 53 and 54.

5.4.3 Data processing

The `UPCochlea.m` script was used to extract each spiral (LS, MS, SS, IS, LSL, MSL, SLS, ILS and ES). Obscured spirals (MS, LSL and MSL) were determined from the CSRF. The

trajectory of the ES was determined using the custom script `UPCochlea.m`. Regression analysis was used to determine which the spiral (LS, MS, SS, IS, SLS, ILS, LSL and MSL) influences the trajectory of the electrode array. The location of the electrode contacts over all the spirals of all the cochleae were determined using regression analysis. Each spiral was compared to the T-levels and DR of each CI user, as well as the implant type (perimodiolar versus lateral wall). Electrode arrays of the same type were pooled and analysed separately. The sample size was small and the cochlear class could not be compared individually, thus only the pooled cochleae were analysed.

5.5 RESULTS

5.5.1 Reconstruction of live cochleae and insertion depth

Reconstruction of the 3D wireframes based on the polynomial equations that were fitted to the raw measurement data are presented in Figure 5.2. The inserted electrode array is represented by the red line. The final location and trajectory of the perimodiolar electrode arrays could be visualised. The insertion depths of the cochleae are represented in Table 5.2.

Table 5.2. Insertion depth in degrees of each electrode array

User	Insertion depth
S5P	360
S31P	410
S32LP	360
S32RP	385
S38P	495
S42P	340
S43R	395
S45P	465

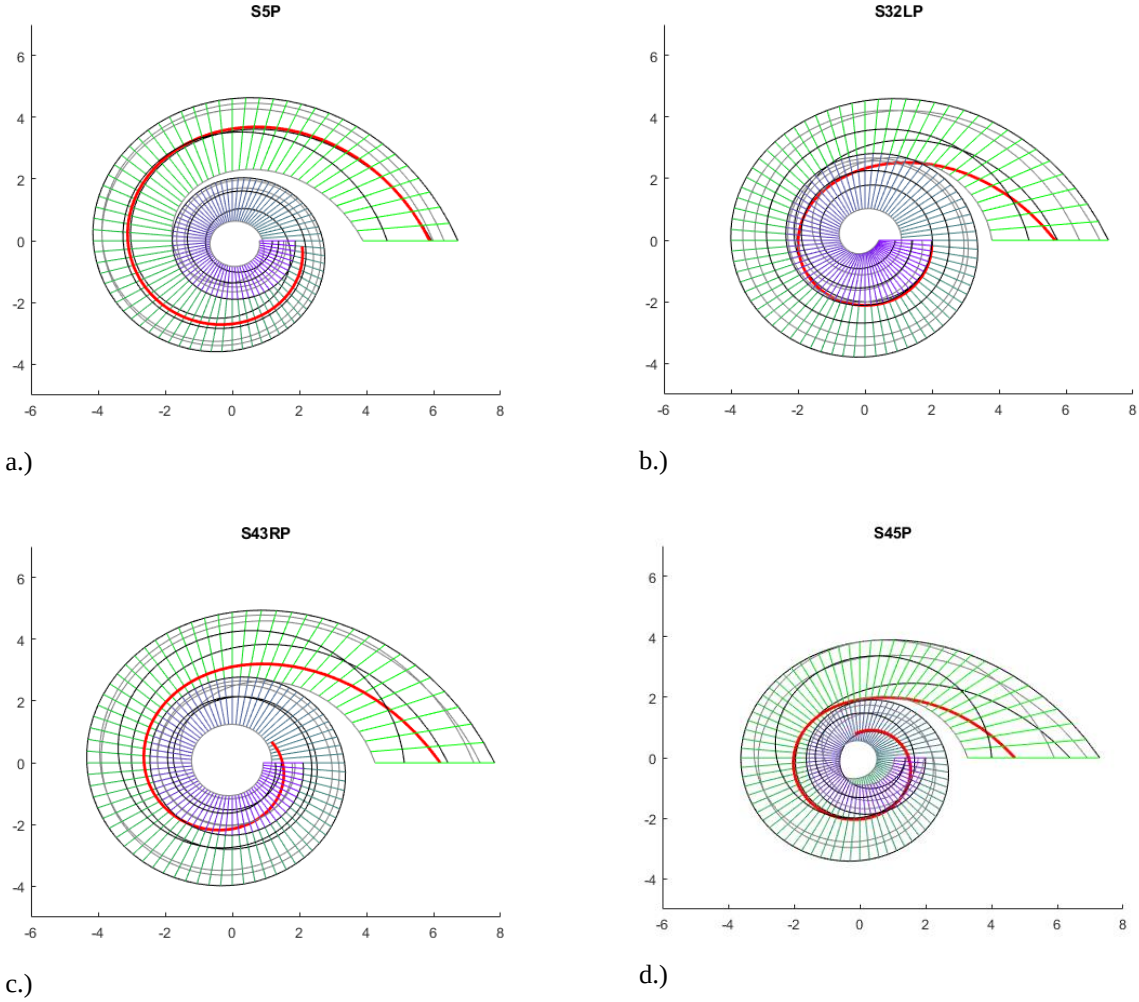

Figure 5.2. A representation of four live cochleae implanted with perimodiolar arrays. The different insertion depths in a.) 360º, b.) 360º c.) 395º and d.) 465º can be visualised, red spirals indicate the electrode array while green spirals refer to the cochlear spirals

5.5.2 Location of the ES in relation to the cochlear spirals

Regression analysis for the radius and height was performed to determine if a there is a correlation between the ES spiral and the measured spirals LS, SS. The IS, SLS and ILS, as well as the predicted MS, LSL and MSL, are shown in Table 5.3.

Table 5.3. Correlation of the ES to the cochlear spirals

Electrode radius regression with spirals								
	LS	MS	SS	IS	LSL	MSL	SLS	ILS
R^2	0.854057	0.695185	0.807725	0.823767	0.797225	0.666393	0.84632	0.849943
F	1018.247	396.8386	730.9558	813.3272	684.0943	347.5713	958.2194	985.5577
p-value	1.26E-74	9.33E-47	3.37E-64	1.71E-67	3.47E-62	2.45E-43	1.13E-72	1.41E-73
estimate of the error variance	0.413972	0.864616	0.545393	0.499891	0.575177	0.946287	0.435919	0.425642
Electrode height regression with spirals								
	LS	MS	SS	IS	LSL	MSL	SLS	ILS
R^2	0.587726	0.283149	0.568913	0.373313	0.533584	0.439502	0.577683	0.469735
F	248.0492	68.72815	229.6311	103.6505	199.0578	136.438	238.0126	154.1379
p-value	2.61E-35	2.96E-14	1.28E-33	2.16E-19	1.25E-30	1.21E-23	2.13E-34	9.40E-26
estimate of the error variance	0.194492	0.338177	0.203367	0.295642	0.220033	0.264417	0.19923	0.250154

Regression analysis for the radii and heights of the cochlear spirals and ES was used to determine if a correlation exists between electrode array location and psychometric outcomes, i.e DR and T-level; is shown in Table 5.4. The psychometric measures of the T-level (THR1) and DR (DR1) immediately after the CI were switched on and the most recent T-level (THR2) and DR (DR2) were used.

Table 5.4 Correlation of the ES to the psychoacoustic outcomes

THR1 regression with radius									
	LS	MS	SS	IS	LSL	MSL	SLS	ILS	EL
R^2	0.2385	0.1611	0.2246	0.2473	0.2528	0.2376	0.224	0.2498	0.2758
F	52.916	32.4471	48.9559	55.5394	57.173	52.6552	48.7866	56.2613	64.3528
p-value	0	0	0	0	0	0	0	0	0
estimate of the error variance	455.227	501.4824	463.4984	449.9084	446.6588	455.7628	463.8586	448.4667	432.916
THR1 regression with height									
	LS	MS	SS	IS	LSL	MSL	SLS	ILS	EL
R^2	0.0002	0.2045	0.0423	0.0904	0	0.0007	0.0198	0.0532	0
F	0.0356	43.4408	7.4636	16.7917	0.0037	0.1162	3.411	9.5009	0.0006
p-value	0.8505	0	0.007	0.0001	0.9515	0.7336	0.0665	0.0024	0.9807
estimate of the error variance	597.6384	475.5309	572.4818	543.7388	597.7513	597.3537	585.9382	565.9479	597.7623
DR1 regression with radius									
	LS	MS	SS	IS	LSL	MSL	SLS	ILS	EL
R^2	0.0041	0.0016	0.0062	0.0032	0.0043	0.0005	0.0042	0.0037	0.0165
F	0.6995	0.2642	1.0526	0.5409	0.7322	0.081	0.7213	0.634	2.8397
p-value	0.4041	0.6079	0.3064	0.4631	0.3934	0.7763	0.3969	0.427	0.0938
estimate of the error variance	227.3644	227.9491	226.8922	227.5771	227.3206	228.1961	227.3352	227.4522	224.5326
DR1 regression with height									
	LS	MS	SS	IS	LSL	MSL	SLS	ILS	EL
R^2	0.0135	0.0367	0.0217	0.0072	0.0226	0.0146	0.02	0.0003	0.0211
F	2.3059	6.4366	3.7432	1.2253	3.906	2.4978	3.4512	0.0457	3.645
p-value	0.1308	0.0121	0.0547	0.2699	0.0497	0.1159	0.0649	0.8309	0.0579
estimate of the error variance	225.2323	219.9291	223.3583	226.6621	223.148	224.9803	223.7365	228.2437	223.4853
THR2 regression with radius									
	LS	MS	SS	IS	LSL	MSL	SLS	ILS	EL
R^2	0.3656	0.2898	0.3326	0.273	0.2756	0.136	0.3674	0.3185	0.4507
F	96.7969	68.5597	83.7351	63.094	63.9015	26.4413	97.5525	78.5188	137.8577
p-value	0	0	0	0	0	0	0	0	0
estimate of the error variance	283.2171	317.0235	297.9123	324.5216	323.3916	385.6947	282.4111	304.2161	245.1957
THR2 regression with height									
	LS	MS	SS	IS	LSL	MSL	SLS	ILS	EL
R^2	0.2786	0.0063	0.5169	0.0223	0.3086	0.3692	0.4544	0.0212	0.1265
F	64.8914	1.0652	179.7372	3.8328	74.9721	98.3111	139.8915	3.6434	24.3404
p-value	0	0.3035	0	0.0519	0	0	0	0.058	0

estimate of the error variance	322.0171	443.5862	215.6657	436.4417	308.6568	281.6067	243.5761	436.9234	389.9077
DR2 regression with radius									
	LS	MS	SS	IS	LSL	MSL	SLS	ILS	EL
R^2	0.0879	0.0332	0.089	0.0327	0.0665	0.0132	0.0857	0.0632	0.0028
F	16.1992	5.769	16.4178	5.6779	11.9723	2.2526	15.7488	11.3422	0.4721
p-value	0.0001	0.0174	0.0001	0.0183	0.0007	0.1353	0.0001	0.0009	0.493
estimate of the error variance	355.1944	376.5145	354.7734	376.7118	363.5367	384.2909	356.0651	364.8138	388.3524
DR2 regression with height									
	LS	MS	SS	IS	LSL	MSL	SLS	ILS	EL
R^2	0.013	0.0009	0.0637	0.164	0.0234	0.0248	0.0594	0.027	0.0115
F	2.2051	0.1522	11.4313	32.9455	4.0205	4.2671	10.6172	4.6598	1.9511
p-value	0.1394	0.697	0.0009	0	0.0466	0.0404	0.0014	0.0323	0.1643
estimate of the error variance	384.3982	389.0912	364.6327	325.5933	380.3414	379.7969	366.2946	378.9332	384.9726

5.6 DISCUSSION

The interrelation between cochlear anatomy, electrode design and surgical approach is intuitive, as the anatomical inter-individual variations influence the final position of the electrode carrier, the approach to CI and electrode design (Erixon *et al.*, 2009, Rask-Andersen *et al.*, 2012, Avci *et al.*, 2014, Avci *et al.*, 2017, Pietsch *et al.*, 2017). The type and location of the electrode array, i.e. the proximity of the electrodes to the modiolar wall, have important psychoacoustic implications (Frijns *et al.*, 2001a, Balkany *et al.*, 2002, Husstedt, 2002, Saunders *et al.*, 2002, Hughes and Abbas, 2006, Stickney *et al.*, 2006, Adunka *et al.*, 2007, Rebscher *et al.*, 2007, Rebscher *et al.*, 2008, Connor *et al.*, 2009, Biedron *et al.*, 2010, Kalkman *et al.*, 2014, Kang *et al.*, 2015, Brant and Ruckenstein, 2016, Kalkman *et al.*, 2016, Büchner *et al.*, 2017, Dhanasingh and Jolly, 2017). This is intuitive when it is realised that the exact location of the electrode contacts in the cochlea dictates the spread of neural excitation, and thus the perception that may be elicited through electrical stimulation (Hanekom and Hanekom, 2016).

5.6.1 Insertion depth

In longer cochleae and those with a wider basal turn, electrode array bands will be positioned more laterally. Such electrode bands will produce more broadly spreading electrical fields and lower activation function amplitudes, suggesting higher neural thresholds and larger spread of excitation (Finley *et al.*, 1990, Kalkman *et al.*, 2016). A longer cochlear base length will result in the implant array lying closer to the outer cochlear wall, which may affect the separation distance of the electrode contacts and the target neurons and cause strain on the lateral wall and BM (Rask-Andersen *et al.*, 2012, Van der Marel *et al.*, 2014). Shorter cochleae need shallower insertion depth to reach low-frequency areas, while longer cochleae need deeper insertion to reach low-frequency areas. In shorter cochleae implanted with longer electrode arrays, insertion depth is thought to be deeper, thus reaching the higher-frequency areas. In order words, with smaller cochleae the high-frequency areas of the cochlea will be reached much sooner than with larger cochlea (Rask-Andersen *et al.*, 2012). Similarly, the height of each cochlear turn will affect the position of the electrode array within the ST, with a larger cochlear height leading to an array position far more separated from the OoC. A current source placed underneath the SL will produce lower neural excitation thresholds (Wilson *et al.*, 1991, Frijns *et al.*, 1995, Frijns *et al.*, 1996, Hanekom, 2001, Kalkman *et al.*, 2016). This was seen especially in cochleae of the rollercoaster profile. The insertion depths as visualised in Figure 5.2 clearly show that smaller cochleae have a deeper insertion depth. However, the final location of the electrode array depends on the individual cochlear geometry.

5.6.2 The effect of cochlear anatomy

In a study by (Avci *et al.*, 2017), the force profiles during electrode insertion are statistically significantly correlated with individual geometry. The presence of dips, peaks and vertical jumps that define cochlear taxonomy may cause translocation of the electrode array from the ST to the SV, damage to the BM and tip fold-over (Avci *et al.*, 2014, Pietsch *et al.*, 2017). By investigating the location of the electrode location in two dimensions, rather than one, the present study showed that a strong relationship between the radii of the individual spirals

LS, SS, IS, SLS and ILS exists. This means that the final location of the electrode arrays in this study is dependent on these spirals. A weaker correlation between the obscured spirals MS and MLS predicted by the CRSF in this study exists and could be explained by the definition of the landmarks. The MS landmarks were placed at the medial-most wall of each turn and varied, as these were sometimes placed at the medial-most point of the ST and at other times the medial-most point of the SV. The medial edge of the SL is difficult to discern and could thus contribute to the results shown above. For the height data of each spiral, a weaker et important, correlation between the z-location of the electrode contact in the cochlear canals exists. This should be quantified in further studies by including more CT scans with electrode arrays inserted. This confirms that individual cochlear anatomy affects electrode location in two dimensions.

5.6.3 Relationship between electrode location and psychometric outcomes

Perimodiolar electrode array designs result in a closer relationship between the array and target neurons, but carry a potential insertion trauma risk (Rask-Andersen *et al.*, 2012). Current sources placed closer to the modiolar wall in smaller, shorter, narrower cochleae produce lower neural excitation thresholds (Frijns *et al.*, 1995, Frijns *et al.*, 1996, Kalkman *et al.*, 2016). In addition, the electrodes in an array will span a smaller pitch range and have greater separation when implanted in longer cochleae. Greater separation between electrodes is said to contribute to better speech understanding, as the channels are better separated into a larger number of physiologically effective independent channels (Dorman *et al.*, 1997, Friesen *et al.*, 2001, Hochmair *et al.*, 2015). With shorter cochleae the channels will be placed closer together, which may cause channel interference (Wilson *et al.*, 1991, Stickney *et al.*, 2006). Electrical field interactions are one such form of channel interaction, which may result in an electrical-field summation occurring prior to nerve fibre activation. This would produce an altered stimulus with a different intensity than what was originally intended, consequently causing a different neural firing pattern and possibly a distorted speech signal (Stickney *et al.*, 2006, Hanekom and Hanekom, 2016). A negative correlation exists between electrode number, radial distance of the electrode contact from the modiolar

wall and T-levels, with higher T-levels for the more basal electrodes, and lower ones for the more apical electrodes. A significant correlation between DR and radial distance exists, with DR being lower with larger radial distances. DR is lower for the more basal electrodes, and higher for the more apical electrodes (WardSaunders *et al.*, 2002, Adunka *et al.*, 2004, Wardrop *et al.*, 2005, Cohen *et al.*, 2006, Biedron *et al.*, 2010, Wanna *et al.*, 2011). However, this study showed that perimodiolar arrays had only a weak correlation of radius and height for DR and T-levels. This could be explained by a few theories. Firstly, live cochleae in this study had a wide range of inactive electrodes (i.e. the first 130º), meaning that no current was available for stimulation of the basal end of the cochleae. Secondly, the psychometric readings were taken on two occasions, immediately after CI activation and subsequently the most recent readings. The time spans between readings were not considered and variable outcomes were instinctive. Other studies measured the linear distance between the electrode contact and modiolar wall, whereas this study compared a polynomial description of the ES with a predicted polynomial MS trajectory. The MS, which gave an indication of the modiolar wall, did not account for all the variation seen in cochlear geometry. This means that variation in the definition and placement of the medial-most parameter of each cochlear turn existed and may account for the very weak correlation of DR to ES for both radius and height. The strongest correlation between psychometric outcomes and the ES was seen in the THR-electrode distance. This correlation became stronger over time as more fibrous tissue was formed and an increase in threshold would be needed to maintain similar hearing outcomes.

Other factors, such as traumatic electrode array insertion, amount of residual hearing, different surgical techniques used by CI surgeons, duration of hearing loss, aetiology, type of cochlea (taxonomy), sex of the CI user and postlingual status, could provide better insight into the results for each specific user.

The surgical implications of variations in cochlear geometry during array insertion may result in difficulties in reaching the second turn without causing trauma, particularly with respect to the spiral ligament at the junction of the first and second turn, the BM and the OSL (Martinez-Monedero *et al.*, 2011). In cochleae with a smaller cochlear base length, this area

may be reached earlier during surgical array insertion, increasing the risk of surgical perforation of the cochlear membranes and wall when the electrode tip moves from the first to the second turn (Martinez-Monedero *et al.*, 2011, Rask-Andersen *et al.*, 2012).

Surgical technique plays an important role in electrode array position (Huttenbrink *et al.*, 2002, Saunders *et al.*, 2002, Peterson *et al.*, 2010, Cosetti and Waltzman, 2012, Zohdi *et al.*, 2014) and, together with cochlear morphology, accounts for the variable functional outcomes in CI users. Therefore, a future study of the electrode positions of an inserted cochlear implantation for different clinician is needed to advise on the technique needed for a particular cochlear class.

5.7 CONCLUSION

This study found that:

- Cochlear geometry effects the insertion depth of an electrode array.
- The radius of the electrode location is strongly correlated to the LS, SS, IS, SLS, ILS and LSL.
- Even though a weak correlation between the height of the electrode location and the cochlear spirals exist, more research is warranted. This can be improved upon by increasing the sample size.

CHAPTER 6 DISCUSSION

6.1 RESEARCH REVIEW

The goal of this study were to provide detailed algorithmic descriptions of the cochlear spirals that constitute the cochlear morphology. Reference spirals were algorithmically described to use as a reference for spirals that may be obscured owing to low-resolution scanning or the presence of artefacts. The PMAE was determined for each cochlear spiral over the different turns. Secondly, the study aimed to translate the manually measured landmarks into rapid knowledge-based automated cochlear computational models. These landmarks are important for finding the cochlear boundaries and define the search fields needed by the automated model to place landmarks for each cochlear type. Lastly, the functional implications of the cochlear class needed to be investigated. The DR of CI users was correlated with cochlear class and implant type (perimodiolar). The trajectory of the electrode array was also described.

6.2 GENERAL DISCUSSION

6.2.1 How accurately can the spiralling nature of the cochlea be algorithmically described from measured landmarks that describe these spirals? Can the cochlear spirals for each cochlear class be standardised?

The study showed that the manually measured landmarks could be used to describe the spiralling nature of each cochlea and to classify the cochleae as rollercoaster, sloping or

intermediate, depending on whether critical anatomical points were present. The description of each spiral allowed for the derivation of obscured spiral trajectories from the measured (reference) spirals.

6.2.2 How well can the trajectory of obscured cochlear spirals be derived from reference spirals for which all cochlear landmarks are visible? What is the accuracy of such a method?

By normalising each reference spiral to the lateral spiral of each cochlea, an average spiral trajectory for each spiral could be calculated. This allowed for the calculation of the MAE between the reference spirals for each cochlea. The PMAE was determined to establish how accurately the spirals can be distinguished from each other to make the determination of obscured spirals possible. By ranking the PMAE from best predictor to second and third best predictor for each cochlear turn, the behaviour of each spiral trajectory could be described. The reference spiral trajectories were translated to CT scans.

6.2.3 Can a CSRF be used to validate the integrity of an existing automated model generator and what would such a workflow entail?

The manually measured landmarks used to create the CSRF were translated for the development of a workflow to inform on the criteria need to test the integrity of a model and to validate the workflow. The criteria used for validating the integrity of a model was found to be more than 80% for a “good” model, more than 60% for a “fair” model and less than 60% for a “poor” model. The CIMVW was validated by comparing the measured CSRF against the measured outcomes of the model to be tested. The inclusion of more cochleae for the refinement of the CSRF could potentially increase the accuracy of the resulting criteria.

6.2.4 Which of the quantified cochlear spirals, if any contribute to the functional outcomes of cochlear implantation? Do the spiral trajectories of the cochlea predict the position of the electrode array? What is the effect of the electrode position on the functional outcomes influencing the objective outcomes after

CI insertion?

This study investigated the effect of cochlear geometry (expressed in polynomial equations) on electrode location in two dimensions. A strong relationship between the radii of the LS, SS, IS, SLS, ILS and LSL and ES trajectory of perimodiolar CIs was found. Thus, the final location of the electrode array is influenced by these spirals. A weak correlation between the heights of the electrode spirals was found which could mean that the height placement of the electrode array is influenced by cochlear geometry. This relation may become stronger if a larger sample size is included.

6.3 LIMATATIONS OF THE STUDY AND FUTURE RESEARCH

- The study used a selection of different types of cochleae; however, an increase in sample size for the construction of the CSRF and for the improvement of the accuracy with which each landmark is calculated, as well as the optimisation of smaller search fields for the placement of cochlear landmarks in the knowledge-based automated landmark computational models of the cochleae.
- The distribution among the three classes cannot be determined before the selection of cochleae to be measured are selected. An equal distribution will refine the algorithms that describe each cochlea.
- The application of the polynomial equations that describe each obscured spiral needs to be applied to low-resolution scanning modalities.
- The landmarks employed in this study are type III (Bookstein, 1991). These types of landmarks are dependent on reference orientations of other parts of the labyrinth. This was addressed to some degree by orientating the cochlea in the cochlear view. Such type III landmarks are, however, not truly homologous, as they cannot accommodate torsion and asymmetrical shapes.
- The investigation of more critical anatomical points and the refinement of clear places in the trajectory of the lateral spiral where dips, peaks and vertical jumps take

place to classify the cochlea better and the definition of subclasses will further refine cochlear taxomomy.

- The implementation of thinly sliced histologically sectioned cochleae is necessary for the exact measurement of landmark parameters in the apical region to describe the spiral trajectories of each spiral of each cochlea better.
- The inclusion of the SLS and ILS landmarks in the AMG needs to be investigated to refine cochlear geometry in a clinical setting.
- Further investigation of the functional outcomes of cochlear type is required, by comparing cochlear class to more psychoacoustic factors such as threshold level, comfort level and impedance. This can be further expanded by separating electrode types into manufacturer types as well.
- Correlations between the final electrode location and the cochlear spirals in two dimensions are promising and need further investigation.
- Other than cochlear morphology, surgical technique affects electrode array position. A blind study involving a variety of CI surgeons is needed to inform clinicians of the appropriate surgical technique required for CI.
- The functional implications of cochlear class need further attention, as the sample size was too small. However, the method addressed the validity of our findings and deductions. The radial position of the electrode contacts was investigated in two dimensions, rather than one. The present study showed that a strong relationship between the radii of the individual spirals LS, SS, IS, SLS and ILS and electrode location exists. By using a larger sample size, validity to the correlations can be deduced, as well as, the correlation between height positions of the electrode location and the cochlear spirals.
- Future studies on the electrode positions of an inserted cochlear implantation by different surgeons is needed to advise surgeons on the technique needed for a particular cochlear class.

CHAPTER 7 CONCLUSION

The following conclusions were drawn from this study:

- This study presented a predefined set of anatomical landmarks that describe cochlear geometry, classify each cochlea and offer a way to extract these anatomical landmarks.
- Algorithms that describe each cochlear spiral of each cochlear class were developed and can be used to derive mathematical descriptions of each spiral in circumstances where a spiral may be obscured.
- The study provided a workflow (CIMVW) for validating the integrity of 3D computational models of the cochleae. An accuracy of 80% and above is recommended to decide if a 3D computational cochlea model is valid.
- The study calculated the trajectory of electrode arrays of CI users to determine if cochlear morphology affects the position of the electrode contact in two dimensions. A strong correlation between the radii LS, SS, IS, SLS, ILS and LSL and the radial location of the electrode was found. A weak relation ($R^2 \leq 0.05$) between the heights of the cochlear spirals and electrode location was found.
- The correlation between the electrode location and psychometric outcomes was weak, with the strongest correlation, which increases with time after cochlear implantation, seen in T-levels. Individual factors could play a role in the relationship seen between electrode location and psychometric outcomes.

REFERENCES

Abdel Salam, S., Tayel, S., Mehanna, A., Eid, M. & Afifi, W. 2013. Comparison of Scalar Location and Insertion Depth of Cochlear Implant Electrode Implanted Through The Round Window Versus Cochleostomy Approach. *J Int Adv Otol,* 9**,** 30-37.

Adunka, O., Gstoettner, W., Hambek, M., Unkelbach, M. H., Radeloff, A. & Kiefer, J. 2004. Preservation of basal inner ear structures in cochlear implantation. *ORL J Otorhinolaryngol Relat Spec,* 66**,** 306-12.

Adunka, O. F., Radeloff, A., Gstoettner, W. K., Pillsbury, H. C. & Buchman, C. A. 2007. Scala Tympani Cochleostomy II: Topography and Histology. *Laryngoscope,* 117**,** 2195-2200.

Agrawal, S., Schart-Morén, N., Liu, W., Ladak, H. M., Rask-Andersen, H. & Li, H. 2018. The secondary spiral lamina and its relevance in cochlear implant surgery. *Ups J Med Sci,* 123**,** 9-18.

Agrawal, V. & Newbold, C. 2012. Computer modelling of the cochlea and the cochlear implant: A review. *Cochlear Implants Int,* 13**,** 113-123.

Alansary, A., Oktay, O., Li, Y., Folgoc, L. L., Hou, B., Vaillant, G., Kamnitsas, K., Vlontzos, A., Glocker, B., Kainz, B. & Rueckert, D. 2019. Evaluating reinforcement learning agents for anatomical landmark detection. *Med Image Anal,* 53**,** 156-164.

Aneja, D., Vora, S. R., Camci, E. D., Shapiro, L. G. & Cox, T. C. 2015. Automated Detection of 3D Landmarks for the Elimination of Non-Biological Variation in Geometric Morphometric Analyses. *Proc IEEE Int Symp Comput Based Med Syst,* 2015**,** 78-83.

Arnold, B., Jäger, L. & Grevers, G. 1996. Visualization of Inner Ear Structures by Three-Dimensional High-Resolution Magnetic Resonance Imaging. *Otol Neurotol,* 17**,** 480-485.

Aschendorff, A., Briggs, R., Brademann, G., Helbig, S., Hornung, J., Lenarz, T., Marx, M., Ramos, A., Stöver, T., Escudé, B. & James, C. J. 2017. Clinical investigation of the Nucleus Slim Modiolar Electrode. *Audiol Neurotool,* 22**,** 169-179.

Avci, E., Nauwelaers, T., Hamacher, V. & Kral, A. 2017. Three-Dimensional Force Profile During Cochlear Implantation Depends on Individual Geometry and Insertion Trauma. *Ear Hear,* 38**,** e168-e179.

Avci, E., Nauwelaers, T., Lenarz, T., Hamacher, V. & Kral, A. 2014. Variations in microanatomy of the human cochlea. *J Comp Neurol,* 522**,** 3245-61.

Baker, G. & Barnes, N. Principal flow for tubular objects with non-circular cross-sections. ICPR 2004, 2004. IEEE, 750-753.

Balkany, T. J., Eshraghi, A. A. & Yang, N. 2002. Modiolar Proximity of Three Perimodiolar Cochlear Implant Electrodes. *Acta Otolaryngol,* 122**,** 363-369.

Bettman, R. H., Van Olphen, A. F., Zonneveld, F. W. & Huizing, E. H. 2003. Electrode insertion depth in cochlear implantees estimated during surgery, on plain film radiographs and with electrode function testing. *Eur Arch Otorhinolaryngol,* 260**,** 536-40.

Biedron, S., Prescher, A., Ilgner, J. & Westhofen, M. 2010. The Internal Dimensions of the Cochlear Scalae With Special Reference to Cochlear Electrode Insertion Trauma. *Otol Neurotol,* 31**,** 731-737.

Biedron, S., Westhofen, M. & Ilgner, J. 2009. On the number of turns in human cochleae. *Otol Neurotol,* 30**,** 414-417.

Blamey, P., Arndt, P., Bergeron, F., Bredberg, G., Brimacombe, J., Facer, G., Larky, J., Lindstrom, B., Nedzelski, J., Peterson, A., Shipp, D., Staller, S. & Whitford, L. 1996. Factors affecting auditory performance of postlinguistically deaf adults using cochlear implants. *Audiol Neurootol,* 1**,** 293-306.

Bookstein, F. L. 1986. Size and Shape Spaces for Landmark Data in Two Dimensions. *Statist Sci,* 1**,** 181-222.

Bookstein, F. L. 1997. Shape and the Information in Medical Images. *Comput Vis Image Underst,* 66**,** 97-118.

Bozorg Grayeli, A., Saint Yrieix, C., Imauchi, Y., Cyna-Gorse, F., Ferrary, E. & Sterkers, O. 2005. *Temporal bone density measurements using CT in otosclerosis*.

Brant, J. A. & Ruckenstein, M. J. 2016. Electrode selection for hearing preservation in cochlear implantation: A review of the evidence. *World J Otorhinolaryngol Head Neck Surg,* 2**,** 157-160.

Braun, K., Bohnke, F. & Stark, T. 2012. Three-dimensional representation of the human cochlea using micro-computed tomography data: presenting an anatomical model for further numerical calculations. *Acta Otolaryngol,* 132**,** 603-13.

Briaire, J. J. & Frijns, J. H. 2000a. 3D mesh generation to solve the electrical volume conduction problem in the implanted inner ear. *Simulat Model Pract,* 8**,** 57-73.

Briaire, J. J. & Frijns, J. H. 2000b. Field patterns in a 3D tapered spiral model of the electrically stimulated cochlea. *Hear Res,* 148**,** 18-30.

Briggs, R. J. S., Tykocinski, M., Stidham, K. & Roberson, J. B. 2005. Cochleostomy site: Implications for electrode placement and hearing preservation. *Acta Otolaryngol,* 125**,** 870-876.

Büchner, A., Illg, A., Majdani, O. & Lenarz, T. 2017. Investigation of the effect of cochlear implant electrode length on speech comprehension in quiet and noise compared with the results with users of electro-acoustic-stimulation, a retrospective analysis. *PLoS One,* 12**,** e0174900.

Cakir, A., Labadie, R. F., Zuniga, M. G., Dawant, B. M. & Noble, J. H. 2016. Evaluation of Rigid Cochlear Models for Measuring Cochlear Implant Electrode Position. *Otology & neurotology : official publication of the American Otological Society, American Neurotology Society [and] European Academy of Otology and Neurotology,* 37**,** 1560-1564.

Chaturvedi, A., Mohan, C., Mahajan, S. & Kakkar, V. 2006. *Imaging of cochlear implants*.

Choi, C. T. & Hsu, C.-H. 2009. Conditions for generating virtual channels in cochlear prosthesis systems. *Ann Biomed Eng,* 37**,** 614.

Choi, C. T. & Wang, S. P. 2014. Modeling ECAP in cochlear implants using the FEM and equivalent circuits. *IEEE Trans Magn,* 50**,** 49-52.

Clark, J. H., Yeagle, J., Arbaje, A. I., Lin, F. R., Niparko, J. K. & Francis, H. W. 2012. Cochlear Implant Rehabilitation in Older Adults: Literature Review and Proposal of a Conceptual Framework. *J Am Geriatr Soc,* 60**,** 1936-1945.

Coetzee, H. L., Loots, G. P. & Meiring, J. H. 2003. *Human Histology,* Pretoria, Van Schaik.

Cohen, L. T. 2009. Practical model description of peripheral neural excitation in cochlear implant recipients: 2. Spread of the effective stimulation field (ESF), from ECAP and FEA. *Hear Res,* 247**,** 100-111.

Cohen, L. T., Saunders, E., Knight, M. R. & Cowan, R. S. C. 2006. Psychophysical measures in patients fitted with Contour™ and straight Nucleus electrode arrays. *Hear Res,* 212**,** 160-175.

Cohen, L. T., Xu, J., Xu, S. A. & Clark, G. M. 1996. Improved and simplified methods for specifying positions of the electrode bands of a cochlear implant array. *Am J Otol,* 17**,** 859-865.

Connor, S. E., Bell, D. J., O'gorman, R. & Fitzgerald-O'connor, A. 2009. CT and MR imaging cochlear distance measurements may predict cochlear implant length required for a 360 degrees insertion. *AJNR Am J Neuroradiol,* 30**,** 1425-30.

Connor, S. E. J., Holland, N. J., Agger, A., Leong, A. C., Varghese, R. A., Jiang, D. & Fitzgerald O'connor, A. 2012. Round window electrode insertion potentiates retention in the scala tympani. *Acta Otolaryngol,* 132**,** 932-937.

Coomes Peterson, D. & Schofield, B. R. 2007. Projections from auditory cortex contact ascending pathways that originate in the superior olive and inferior colliculus. *Hear Res,* 232**,** 67-77.

Copeland, B. J., Pillsbury, H. C. & Buchman, C. A. 2004. Prospective evaluation of intraoperative cochlear implant radiographs. *Otol Neurotol,* 25**,** 295-7.

Cords, S. M., Reuter, G., Issing, P. R., Sommer, A., Kuzma, J. & Lenarz, T. 2000. A Silastic Positioner for a Modiolus-Hugging Position of Intracochlear Electrodes: Electrophysiologic Effects. *Otol Neurotol,* 21**,** 212-217.

Cosetti, M. K. & Waltzman, S. B. 2012. Outcomes in cochlear implantation: variables affecting performance in adults and children. *Otolaryngol Clin North Am,* 45**,** 155-71.

Crous, H. G., Hanekom, T. & Hanekom, J. J. 2018. *Investigating the automation of the 3D computational developmet workflow of the cochlear implant.* Masters Dissertation, University of Pretoria.

Dang, K., Clerc, M., Vandersteen, C., Guevara, N. & Gnansia, D. In situ validation of a parametric model of electrical field distribution in an implanted cochlea. 7th International IEEE/EMBS Conference on Neural Engineering (NER) 2015. 667-670.

Davidson, H. C., Harnsberger, H. R., Lemmerling, M. M., Mancuso, A. A., White, D. K., Tong, K. A., Dahlen, R. T. & Shelton, C. 1999. MR evaluation of vestibulocochlear anomalies associated with large endolymphatic duct and sac. *AJNR Am J Neuroradiol,* 20**,** 1435-41.

Davis Timothy, J. T. Relationship Between Electrode-to-Modiolus Distance and Current Levels for Adults With Cochlear Implants. *Otol Neurotol,* 37**,** 31-7.

Demarcy, T., Vandersteen, C., Raffaelli, C., Gnansia, D., Guevara, N., Ayache, N. & Delingette, H. Uncertainty Quantification of Cochlear Implant Insertion from CT Images. Workshop on Clinical Image-Based Procedures, 2016. Springer, 27-35.

Dhanasingh, A. & Jolly, C. 2017. An overview of cochlear implant electrode array designs. *Hear Res,* 356**,** 93-103.

Diamantopoulos, Ii, Ludman, C. N., Martel, A. L. & O'donoghue, G. M. 1999. Magnetic resonance imaging virtual endoscopy of the labyrinth. *Am J Otol,* 20**,** 748-51.

Dimopoulos, P. & Muren, C. 1990. Anatomic variations of the cochlea and relations to other temporal bone structures. *Acta Radiol,* 31**,** 439-444.

Dorman, M. F., Loizou, P. C. & Rainey, D. 1997. Simulating the effect of cochlear-implant electrode insertion depth on speech understanding. *J Acoust Soc Am,* 102**,** 2993-6.

Douglas, T. S. 2004. Image processing for craniofacial landmark identification and measurement: a review of photogrammetry and cephalometry. *Comput Med Imaging Graph,* 28**,** 401-409.

Drake, R. L., Vogl, A. W. & Mitchell, A. W. M. 2010. Head and Neck. *Gray's anatomy for students.* 2 ed. Philadelphia: Churchill Livingstone Elsevier.

Erixon, E., Högstorp, H., Wadin, K. & Rask-Andersen, H. 2009. Variational anatomy of the human cochlea: Implications for cochlear implantation. *Otol Neurotol,* 30**,** 14-22.

Erixon, E. & Rask-Andersen, H. 2013. How to predict cochlear length before cochlear implantation surgery. *Acta Otolaryngol,* 133**,** 1258-65.

Escudé, B., James, C., Deguine, O., Cochard, N., Eter, E. & Fraysse, B. 2006a. The Size of the Cochlea and Predictions of Insertion Depth Angles for Cochlear Implant Electrodes. *Audiol Neurootol,* 11 Suppl 1**,** 27-33.

Escudé, B., James, C., Deguine, O., Cochard, N., Eter, E. & Fraysse, B. 2006b. The Size of the Cochlea and Predictions of Insertion Depth Angles for Cochlear Implant Electrodes. *Audiol Neurotol,* 11**,** 27-33.

Escudé, B., James, C., Deguine, O., Cochard, N., Eter, E. & Fraysse, B. 2006c. The Size of the Cochlea and Predictions of Insertion Depth Angles for Cochlear Implant Electrodes. *Audiology and Neurotology,* 11**,** 27-33.

Eshraghi, A. A., Nazarian, R., Telischi, F. F., Rajguru, S. M., Truy, E. & Gupta, C. 2012. The cochlear implant: historical aspects and future prospects. *Anat Rec,* 295**,** 1967-80.

Fatterpekar, G. M., Doshi, A. H., Dugar, M., Delman, B. N., Naidich, T. P. & Som, P. M. 2006. Role of 3D CT in the Evaluation of the Temporal Bone. *Radiographics,* 26**,** S117-S132.

Fayad, J. N. & Linthicum, F. H. 2006. Multichannel Cochlear Implants: Relation of Histopathology to Performance. *Laryngoscope,* 116**,** 1310-1320.

Fernández, C. 1952. Dimensions of the cochlea (guinea pig). *J Acoust Soc Am,* 24**,** 519-523.

Fernando, A. F., Opulencia, A. P., Maglalang, G. M. & Chua, A. H. 2011. An anatomical study of the cochlea among Filipinos using high-resolution computed tomography scans. *Otolaryngol Head Neck Surg,* 26**,** 6-9.

Finley, C. C., Holden, T. A., Holden, L. K., Whiting, B. R., Chole, R. A., Neely, G. J., Hullar, T. E. & Skinner, M. W. 2008. Role of electrode placement as a contributor to variability in cochlear implant outcomes. *Otol Neurotol,* 29**,** 920-8.

Finley, C. C., Wilson, B. S. & White, M. W. 1990. Models of neural responsiveness to electrical stimulation. *In:* Miller, J. M. & Spelman, F. A. (eds.) *Cochlear Implants: Models of the Electrically Stimulated Ear.* New York, NY: Springer New York.

Fishman, A. J. 2012. Imaging and anatomy for cochlear implants. *Otolaryngol Clin North Am,* 45**,** 1-24.

Friesen, L. M., Shannon, R. V., Baskent, D. & Wang, X. 2001. Speech recognition in noise as a function of the number of spectral channels: comparison of acoustic hearing and cochlear implants. *J Acoust Soc Am,* 110**,** 1150-63.

Frijns, J. H., Briaire, J. J. & Grote, J. J. 2001a. The importance of human cochlear anatomy for the results of modiolus-hugging multichannel cochlear implants. *Otol Neurotol,* 22**,** 340-9.

Frijns, J. H., De Snoo, S. L. & Ten Kate, J. H. 1996. Spatial selectivity in a rotationally symmetric model of the electrically stimulated cochlea. *Hear Res,* 95**,** 33-48.

Frijns, J. H. M., Briaire, J. J. & Grote, J. J. 2001b. The Importance of Human Cochlear Anatomy for the Results of Modiolus-Hugging Multichannel Cochlear Implants. *Otol Neurotol,* 22**,** 340-349.

Frijns, J. H. M., Briaire, J. J. & Schoonhoven, R. 2000. Integrated use of volume conduction and neural models to simulate the response to cochlear implants. *Simulat Model Pract,* 8**,** 75-97.

Frijns, J. H. M., De Snoo, S. L. & Schoonhoven, R. 1995. Potential distributions and neural excitation patterns in a rotationally symmetric model of the electrically stimulated cochlea. *Hear Res,* 87**,** 170-186.

Ghiz, A. F., Salt, A. N., Demott, J. E., Henson, M. M., Henson, O. W. & Gewalt, S. L. 2001. Quantitative anatomy of the round window and cochlear aqueduct in guinea pigs. *Hear Res,* 162**,** 105-112.

Gibson, D., Gluth, M., Whyte, A. & Atlas, M. 2012. Rotation of the osseous spiral lamina from the hook region along the basal turn of the cochlea: results of a magnetic resonance image anatomical study using high-resolution DRIVE sequences. *Surg Radiol Anat,* 34**,** 781-785.

Givelberg, E. & Bunn, J. 2003. A comprehensive three-dimensional model of the cochlea. *J Comput Phys,* 191**,** 377-391.

Gleeson, T. G., Lacy, P. D., Bresnihan, M., Gaffney, R., Brennan, P. & Viani, L. 2003. High resolution computed tomography and magnetic resonance imaging in the pre-operative assessment of cochlear implant patients. *J Laryngol Otol,* 117**,** 692-5.

Gstoettner, W., Franz, P., Hamzavi, J., Plenk, H., Jr., Baumgartner, W. & Czerny, C. 1999. Intracochlear position of cochlear implant electrodes. *Acta Otolaryngol,* 119**,** 229-33.

Gstoettner, W., Kiefer, J., Baumgartner, W. D., Pok, S., Peters, S. & Adunka, O. 2004. Hearing preservation in cochlear implantation for electric acoustic stimulation. *Acta Otolaryngol,* 124**,** 348-52.

Gunz, P., Ramsier, M., Kuhrig, M., Hublin, J. J. & Spoor, F. 2012. The mammalian bony labyrinth reconsidered, introducing a comprehensive geometric morphometric approach. *J Anat,* 220**,** 529-43.

Gupta, A., Kharbanda, O. P., Sardana, V., Balachandran, R. & Sardana, H. K. 2015. A knowledge-based algorithm for automatic detection of cephalometric landmarks on CBCT images. *Int J Comput Assist Radiol Surg,* 10**,** 1737-52.

Hanekom, T. 2001. Three-dimensional spiraling finite element model of the electrically stimulated cochlea. *Ear Hear,* 22**,** 300-15.

Hanekom, T. 2005. Modelling encapsulation tissue around cochlear implant electrodes. *Med Biol Eng Comput,* 43**,** 47-55.

Hanekom, T. & Hanekom, J. J. 2016. Three-dimensional models of cochlear implants: A review of their development and how they could support management and maintenance of cochlear implant performance. *Network,* 27**,** 67-106.

Hans, P., Grant, A. J., Laitt, R. D., Ramsden, R. T., Kassner, A. & Jackson, A. 1999. Comparison of three-dimensional visualization techniques for depicting the scala vestibuli and scala tympani of the cochlea by using high-resolution MR imaging. *AJNR Am J Neuroradiol,* 20**,** 1197-206.

Hardy, M. 1938. The length of the organ of Corti in man. *Am J Anat,* 62**,** 291-311.

Held, P., Fellner, C., Fellner, F., Seitz, J. & Strutz, J. 1997. MRI of inner ear anatomy using 3D MP-RAGE and 3D CISS sequences. *Br J Radiol,* 70**,** 465-72.

Hochmair, I., Hochmair, E., Nopp, P., Waller, M. & Jolly, C. 2015. Deep electrode insertion and sound coding in cochlear implants. *Hear Res,* 322**,** 14-23.

Hoffman, J. & De Beer, F. Characteristics of the micro-focus X-ray tomography system at the MIXRAD facility at NECSA in South Africa. 18th WCNDT, 2012.

Hofman, R., Segenhout, J. & Wit, H. 2009. Three-dimensional reconstruction of the pigeon inner ear. *J Vestib Res,* 19**,** 21-26.

Hughes, M. L. & Abbas, P. J. 2006. Electrophysiologic channel interaction, electrode pitch ranking, and behavioral threshold in straight versus perimodiolar cochlear implant electrode arrays. *J Acoust Soc Am,* 119**,** 1538-1547.

Husstedt, H. W. 2002. Nondestructive three-dimensional analysis of electrode to modiolus proximity. *Otol Neurotol,* 23**,** 49.

Huttenbrink, K. B., Zahnert, T., Jolly, C. & Hofmann, G. 2002. Movements of cochlear implant electrodes inside the cochlea during insertion: an x-ray microscopy study. *Otol Neurotol,* 23**,** 187-91.

Incesulu, A. & Joseph B. Nadol, J. 1998. Correlation of Acoustic Threshold Measures and Spiral Ganglion Cell Survival in Severe to Profound Sensorineural Hearing Loss: Implications for Cochlear Implantation. *Ann Otol Rhinol Laryngol,* 107**,** 906-911.

Ishida, I. M., Sugiura, M., Naganawa, S., Teranishi, M. & Nakashima, T. 2007. Cochlear modiolus and lateral semicircular canal in sudden deafness. *Acta Otolaryngol,* 127**,** 1157-61.

Iyaniwura, J. E., Elfarnawany, M., Ladak, H. M. & Agrawal, S. K. 2018. An automated A-value measurement tool for accurate cochlear duct length estimation. *Otolaryngol Head Neck Surg,* 47**,** 5.

Jäger, L., Bonell, H., Liebl, M., Srivastav, S., Arbusow, V., Hempel, M. & Reiser, M. 2005. CT of the Normal Temporal Bone: Comparison of Multi– and Single–Detector Row CT. *Radiology,* 235**,** 133-141.

Johnson, L. A., Della Santina, C. C. & Wang, X. 2012. Temporal bone characterization and cochlear implant feasibility in the common marmoset (Callithrix jacchus). *Hear Res,* 290**,** 37-44.

Jolly, C. N., Spelman, F. A. & Clopton, B. M. 1996. Quadrupolar stimulation for cochlear prostheses: modeling and experimental data. *IEEE Trans Biomed Eng,* 43**,** 857-865.

Kalkman, R. K., Briaire, J. J., Dekker, D. M. & Frijns, J. H. 2014. Place pitch versus electrode location in a realistic computational model of the implanted human cochlea. *Hear Res,* 315**,** 10-24.

Kalkman, R. K., Briaire, J. J. & Frijns, J. H. 2016. Stimulation strategies and electrode design in computational models of the electrically stimulated cochlea: An overview of existing literature. *Network,* 27**,** 107-134.

Kang, S., Chwodhury, T., Moon, I. J., Hong, S. H., Yang, H., Won, J. H. & Woo, J. 2015. Effects of electrode position on spatiotemporal auditory nerve fiber responses: a 3D computational model study. *Comput Math Method M,* 2015**,** 1-13.

Karino, S., Hayashi, N., Aoki, S., Ohtomo, K. & Yamasoba, T. 2004. New method of using reconstructed images for assessment of patency of intracochlear spaces for cochlear implant candidates. *Laryngoscope,* 114**,** 1253-8.

Kaur, D. & Kaur, Y. 2014. Various Image Segmentation Techniques: A Review. *IJCSMC,* 3**,** 809-814.

Kawano, A., Seldon, H., Clark, G., Ramsden, R. & Raine, C. 1998. Intracochlear factors contributing to psychophysical percepts following cochlear implantation. *Acta Otolaryngol,* 118**,** 313-326.

Kawano, A., Seldon, H. L. & Clark, G. M. 1996. Computer-aided three-dimensional reconstruction in human cochlear maps: measurement of the lengths of organ of Corti, outer wall, inner wall, and Rosenthal's canal. *Ann Otol Rhinol Laryngol,* 105**,** 701-709.

Kendi, T. K., Arikan, O. K. & Koc, C. 2004a. Magnetic resonance imaging of cochlear modiolus: determination of mid-modiolar area and modiolar volume. *J Laryngol Otol,* 118**,** 496-9.

Kendi, T. K., Arikan, O. K. & Koç, C. 2004b. Magnetic resonance imaging of cochlear modiolus: determination of mid-modiolar area and modiolar volume. *J Laryngol Otol,* 118**,** 496-499.

Ketten, D. R. 1994. The role of temporal bone imaging in cochlear implants. *Curr Opin Otolaryngol Head Neck Surg,* 2**,** 401-408.

Ketten, D. R., Skinner, M. W., Wang, G., Vannier, M. W., Gates, G. A. & Neely, J. G. 1998. In vivo measures of cochlear length and insertion depth of Nucleus cochlear implant electrode arrays. *Ann Otol Rhinol Laryngol,* 175**,** 1-16.

Khan, A. M., Whiten, D. M., Nadol, J. J. B. & Eddington, D. K. 2005. Histopathology of human cochlear implants: Correlation of psychophysical and anatomical measures. *Hear Res,* 205**,** 83-93.

Khoza-Shangase, K. & Gautschi-Mills, K. 2019. Exploration of factors influencing the preservation of residual hearing following cochlear implantation. *SAJCD,* 66.

Kikidis, D. & Bibas, A. 2014. A Clinically Oriented Introduction and Review on Finite Element Models of the Human Cochlea. *Biomed Res Int,* 2014**,** 8-16.

Kirk, E. C. & Gosselin-Ildari, A. D. 2009. Cochlear Labyrinth Volume and Hearing Abilities in Primates. *Anat Rec,* 292**,** 765-776.

Koch, R. W., Ladak, H. M., Elfarnawany, M. & Agrawal, S. K. 2017. Measuring Cochlear Duct Length – a historical analysis of methods and results. *Otolaryngol Head Neck Surg,* 46**,** 19.

Kong, W. J., Cheng, H. M., Ma, H., Wang, Y. J. & Han, P. 2012. Evaluation of the implanted cochlear implant electrode by CT scanning with three-dimensional reconstruction. *Acta Otolaryngol,* 132**,** 116-22.

Kós, M.-I., Boëx, C., Sigrist, A., Guyot, J.-P. & Pelizzone, M. 2005. Measurements of electrode position inside the cochlea for different cochlear implant systems. *Acta Otolaryngol,* 125**,** 474-480.

Kral, A., Hartmann, R., Mortazavi, D. & Klinke, R. 1998. Spatial resolution of cochlear implants: the electrical field and excitation of auditory afferents. *Hear Res,* 121**,** 11-28.

Krombach, G. A., Van Den Boom, M., Di Martino, E., Schmitz-Rode, T., Westhofen, M., Prescher, A., Gunther, R. W. & Wildberger, J. E. 2005. Computed tomography of the inner ear: size of anatomical structures in the normal temporal bone and in the temporal bone of patients with Meniere's disease. *Eur Radiol,* 15**,** 1505-13.

Lagravère, M. O., Low, C., Flores-Mir, C., Chung, R., Carey, J. P., Heo, G. & Major, P. W. 2010. Intraexaminer and interexaminer reliabilities of landmark identification on digitized lateral cephalograms and formatted 3-dimensional cone-beam computerized tomography images. *Am J Orthod Dentofacial Orthop,* 137**,** 598-604.

Lane, J. I., Witte, R. J., Driscoll, C. L., Shallop, J. K., Beatty, C. W. & Primak, A. N. 2007. Scalar localization of the electrode array after cochlear implantation: clinical experience using 64-slice multidetector computed tomography. *Otol Neurotol,* 28**,** 658-62.

Lawson, J. T., Cranley, K. & Toner, J. G. 1998. Digital imaging: a valuable technique for the postoperative assessment of cochlear implantation. *Eur Radiol,* 8**,** 951-4.

Le-Tien, T. & Pham-Chi, H. 2014. An Approach for Efficient Detection of Cephalometric Landmarks. *Procedia Comp Sci,* 37**,** 293-300.

Lee, C.-F., Li, G.-J., Wan, S.-Y., Lee, W.-J., Tzen, K.-Y., Chen, C.-H., Song, Y.-L., Chou, Y.-F., Chen, Y.-S. & Liu, T.-C. 2010. Registration of Micro-Computed Tomography and Histological Images of the Guinea Pig Cochlea to Construct an Ear Model Using an Iterative Closest Point Algorithm. *Ann Biomed Eng,* 38**,** 1719-1727.

Lee, C. C. & Sherman, S. M. 2011. On the classification of pathways in the auditory midbrain, thalamus, and cortex. *Hear Res,* 276**,** 79-87.

Lemmerling, M. M., Mancuso, A. A., Antonelli, P. J. & Kubilis, P. S. 1997. Normal modiolus: CT appearance in patients with a large vestibular aqueduct. *Radiology,* 204**,** 213-219.

Leung, J., Wang, N., Yeagle, J. D. & Et Al. 2005. Predictive models for cochlear implantation in elderly candidates. *Arch Otolaryngol Head Neck Surg,* 131**,** 1049-1054.

Li, P. M., Wang, H., Northrop, C., Merchant, S. N. & Nadol Jr, J. B. 2007. Anatomy of the round window and hook region of the cochlea with implications for cochlear implantation and other endocochlear surgical procedures. *Otol Neurotol,* 28**,** 641-648.

Li, S. F., Zhang, T. Y. & Wang, Z. M. 2006. An Approach for Precise Three-Dimensional Modeling of the Human Inner Ear. *J Otorhinolaryngol Relat Spec,* 68**,** 302-310.

Lim, Y. S., Park, S.-I., Kim, Y. H., Oh, S. H. & Kim, S. J. 2005. Three-dimensional analysis of electrode behavior in a human cochlear model. *Med Eng Phys,* 27**,** 695-703.

Liu, B., Gao, X. L., Yin, H. X., Luo, S. Q. & Lu, J. 2007. A detailed 3D model of the guinea pig cochlea. *Brain Struct Func,* 212**,** 223-230.

Ludman, C. N. 2000. Recent advances in magnetic resonance imaging of the inner ear. *Audiol Med*.

Lutz, J., Jäger, V., Hempel, M., Srivastav, S., Reiser, M. & Jäger, L. 2007. Delineation of temporal bone anatomy: feasibility of low-dose 64-row CT in regard to image quality. *Eur Radiol,* 17**,** 2638-2645.

Malherbe, T. K. 2009. *Development of a method to create subject specific cochlear models for electric hearing*. Master of Engineering (Bio-Engineering), Pretoria.

Malherbe, T. K., Hanekom, T. & Hanekom, J. J. 2013. Can subject-specific single-fibre electrically evoked auditory brainstem response data be predicted from a model? *Med Eng Phys,* 35**,** 926-36.

Malherbe, T. K., Hanekom, T. & Hanekom, J. J. 2015. The effect of the resistive properties of bone on neural excitation and electric fields in cochlear implant models. *Hear Res,* 327**,** 126-135.

Malherbe, T. K., Hanekom, T. & Hanekom, J. J. 2016. Constructing a three-dimensional electrical model of a living cochlear implant user's cochlea. *Int J Numer Method Biomed Eng,* 32**,** e02751.

Martinez-Monedero, R., Niparko, J. K. & Aygun, N. 2011. Cochlear Coiling Pattern and Orientation Differences in Cochlear Implant Candidates. *Otol Neurotol,* 32**,** 1086-1093

Melhem, E. R., Shakir, H., Bakthavachalam, S., Macdonald, C. B., Gira, J., Caruthers, S. D. & Jara, H. 1998. Inner ear volumetric measurements using high-resolution 3D T2-weighted fast spin-echo MR imaging: initial experience in healthy subjects. *AJNR Am J Neuroradiol,* 19**,** 1819-22.

Meneses, M. S. D., Cardoso, C. C. & Silva, I. M. D. C. 2014. Fatores que interferem no desempenho de usuários de implante coclear em testes de percepção de fala. *Revista CEFAC,* 16**,** 65-71.

Meng, Q. L., Han, H., Jin, Z., Bo, Y., Zhang, Y. Y., Pang, G., Zhu, Y. Y. & Duan, M. 2007. Anatomic study of maximum intensity projection of the membranous labyrinth and the internal auditory meatus - MRI scan in 16 Chinese adults. *Acta Otolaryngol,* 127**,** 1150-1156.

Mens, L. H. & Berenstein, C. K. 2005. Speech perception with mono-and quadrupolar electrode configurations: a crossover study. *Otol Neurotol,* 26**,** 957-964.

Meshik, X., Holden, T. A., Chole, R. A. & Hullar, T. E. 2010. Optimal cochlear implant insertion vectors. *Otol Neurotol,* 31**,** 58-69.

Micco, A. G. & Richter, C.-P. 2006. Tissue resistivities determine the current flow in the cochlea. *Curr Opin Otolaryngol Head Neck Surg,* 14**,** 352-355

Miller, J. D. 2007. Sex differences in the length of the organ of Corti in humans. *J Acoust Soc Am,* 121**,** El151-5.

Murugasu, E., Hans, P., Jackson, A. & Ramsden, R. T. 1999. The application of three-dimensional magnetic resonance imaging rendering of the inner ear in assessment for cochlear implantation. *Am J Otol,* 20**,** 752-7.

Naganawa, S., Ito, T., Iwayama, E., Fukatsu, H., Ishigaki, T., Nakashima, T. & Ichinose, N. 1999. MR Imaging of the Cochlear Modiolus: Area Measurement in Healthy

Subjects and in Patients with a Large Endolymphatic Duct and Sac1. *Radiology,* 213**,** 819-823.

Nair, S. B., Abou-Elhamd, K. A. & Hawthorne, M. 2000. A retrospective analysis of high resolution computed tomography in the assessment of cochlear implant patients. *Clin Otolaryngol Allied Sci,* 25**,** 55-61.

Neri, E., Caramella, D., Cosottini, M., Zampa, V., Jackson, A., Berrettini, S., Sellari-Franceschini, S. & Bartolozzi, C. 2000. High-resolution magnetic resonance and volume rendering of the labyrinth. *Eur Radiol,* 10**,** 114-8.

Ni, G., Elliott, S. J., Ayat, M. & Teal, P. D. 2014. Modelling Cochlear Mechanics. *Biomed Res Int,* 2014**,** 1-42.

Nicoletti, M., Wirtz, C. & Hemmert, W. 2013. Modeling sound localization with cochlear implants. *The technology of binaural listening.* Springer.

Noble, J. H., Labadie, R. F., Majdani, O. & Dawant, B. M. 2011. Automatic segmentation of intracochlear anatomy in conventional CT. *IEEE Trans Biomed Eng,* 58**,** 2625-32.

Nogueira, W., Schurzig, D., Büchner, A., Penninger, R. T. & Würfel, W. 2016. Validation of a Cochlear Implant Patient-Specific Model of the Voltage Distribution in a Clinical Setting. *Front Bioeng Biotechnol,* 4.

O'connell, B. P., Hunter, J. B., Haynes, D. S., Holder, J. T., Dedmon, M. M., Noble, J. H., Dawant, B. M. & Wanna, G. B. 2017. Insertion depth impacts speech perception and hearing preservation for lateral wall electrodes. *Laryngoscope,* 127**,** 2352-2357.

Oxenham, A. J. & Bacon, S. P. 2003. Cochlear Compression: Perceptual Measures and Implications for Normal and Impaired Hearing. *Ear Hear,* 24**,** 352-366.

Pal, N. R. & Pal, S. K. 1993. A review on image segmentation techniques. *Pattern Recogn,* 26**,** 1277-1294.

Parkinson, A. J., Arcaroli, J., Staller, S. J., Arndt, P. L., Cosgriff, A. & Ebinger, K. 2002. The Nucleus® 24 Contour™ Cochlear Implant System: Adult Clinical Trial Results. *Ear Hear,* 23**,** 41S-48S.

Parthasarathi, A. A., Grosh, K. & Nuttall, A. L. 2000. Three-dimensional numerical modeling for global cochlear dynamics. *J Acoust Soc Am,* 107**,** 474-485.

Pasanisi, E., Vincenti, V., Bacciu, A., Guida, M. & Bacciu, S. 2002. The Nucleus Contour Electrode Array: An Electrophysiological Study. *Laryngoscope,* 112**,** 1653-1656.

Pelliccia, P., Venail, F., Bonafe, A., Makeieff, M., Iannetti, G., Bartolomeo, M. & Mondain, M. 2014. Cochlea size variability and implications in clinical practice. *Acta Otorhinolaryngol Ital,* 34**,** 42-9.

Peterson, N. R., Pisoni, D. B. & Miyamoto, R. T. 2010. Cochlear implants and spoken language processing abilities: review and assessment of the literature. *Restor Neurol Neurosci,* 28**,** 237-50.

Pfingst, B. E., Franck, K. H., Xu, L., Bauer, E. M. & Zwolan, T. A. 2001. Effects of electrode configuration and place of stimulation on speech perception with cochlear prostheses. *JARO-J Assoc Res Oto,* 2**,** 87-103.

Pietsch, M., Aguirre Dávila, L., Erfurt, P., Avci, E., Lenarz, T. & Kral, A. 2017. Spiral Form of the Human Cochlea Results from Spatial Constraints. *Sci Rep,* 7**,** 7500-7500.

Pochini Sobrinho, F., Lazarini, P. R., Yoo, H. J., Abreu Júnior, L. & Meira, A. S. 2009. A method for measuring the length of the cochlea through magnetic resonance imaging. *Braz J Otorhinolaryngol,* 75**,** 261-267.

Polly, P. D., Stayton, C. T., Dumont, E. R., Pierce, S. E., Rayfield, E. J. & Angielczyk, K. D. 2016. Combining geometric morphometrics and finite element analysis with evolutionary modeling: towards a synthesis. *J Vertebr Paleontol,* 36**,** e1111225.

Postnov, A., Zarowski, A., De Clerck, N., Vanpoucke, F., Offeciers, E., Dyck, D. & Peeters, S. 2006. *High resolution micro-CT scanning as an innovatory tool for evaluation of the surgical positioning of cochlear implant electrodes*.

Poznyakovskiy, A. A., Zahnert, T., Kalaidzidis, Y., Lazurashvili, N., Schmidt, R., Hardtke, H.-J., Fischer, B. & Yarin, Y. M. 2011. A segmentation method to obtain a complete geometry model of the hearing organ. *Hear Res,* 282**,** 25-34.

Poznyakovskiy, A. A., Zahnert, T., Kalaidzidis, Y., Schmidt, R., Fischer, B., Baumgart, J. & Yarin, Y. M. 2008. The creation of geometric three-dimensional models of the inner ear based on micro computer tomography data. *Hear Res,* 243**,** 95-104.

Proctor, B., Bollobas, B. & Niparko, J. K. 1986. Anatomy of the round window niche. *Ann Otol Rhinol Laryngol,* 95**,** 444-6.

Purcell, D., Johnson, J., Fischbein, N. & Lalwani, A. K. 2003. Establishment of normative cochlear and vestibular measurements to aid in the diagnosis of inner ear malformations. *Otolaryngol Head Neck Surg,* 128**,** 78-87.

Raft, S., Nowotschin, S., Liao, J. & E Morrow, B. 2004. *Suppression of neural fate and control of inner ear morphogenesis by TBX1*.

Rask-Andersen, H., Liu, W., Erixon, E., Kinnefors, A., Pfaller, K., Schrott-Fischer, A. & Glueckert, R. 2012. Human cochlea: anatomical characteristics and their relevance for cochlear implantation. *Anat Rec,* 295**,** 1791-811.

Rau, T. S., Hussong, A., Herzog, A., Majdani, O., Lenarz, T. & Leinung, M. 2011. Accuracy of computer-aided geometric 3D reconstruction based on histological serial microgrinding preparation. *Comput Med Imaging Graph,* 14**,** 581-594.

Rebscher, S. J., Hetherington, A., Bonham, B., Wardrop, P., Whinney, D. & Leake, P. A. 2008. Considerations for design of future cochlear implant electrode arrays: electrode array stiffness, size, and depth of insertion. *J Rehabil Res Dev,* 45**,** 731-747.

Rebscher, S. J., Hetherington, A. M., Snyder, R. L., Leake, P. A. & Bonham, B. H. 2007. Design and fabrication of multichannel cochlear implants for animal research. *J Neurosci Methods,* 166**,** 1-12.

Rebscher, S. J., Talbot, N., Bruszewski, W., Heilmann, M., Brasell, J. & Merzenich, M. M. 1996. A transparent model of the human scala tympani cavity. *J Neurosci Methods,* 64**,** 105-114.

Reda, F. A., Mcrackan, T. R., Labadie, R. F., Dawant, B. M. & Noble, J. H. 2014. Automatic segmentation of intra-cochlear anatomy in post-implantation CT of unilateral cochlear implant recipients. *Med Image Anal,* 18**,** 605-615.

Rivas, A., Cakir, A., Hunter, J. B., Labadie, R. F., Zuniga, M. G., Wanna, G. B., Dawant, B. M. & Noble, J. H. 2017. Automatic Cochlear Duct Length Estimation for Selection of Cochlear Implant Electrode Arrays. *Otol Neurotol,* 38**,** 339-346.

Rodt, T., Ratiu, P., Becker, H., Bartling, S., Kacher, D., Anderson, M., Jolesz, F. A. & Kikinis, R. 2002a. 3D visualisation of the middle ear and adjacent structures using reconstructed multi-slice CT datasets, correlating 3D images and virtual endoscopy to the 2D cross-sectional images. *Neuroradiol J,* 44**,** 783-790.

Rodt, T., Ratiu, P., Becker, H., Bartling, S., Kacher, D. F., Anderson, M., Jolesz, F. A. & Kikinis, R. 2002b. 3D visualisation of the middle ear and adjacent structures using

reconstructed multi-slice CT datasets, correlating 3D images and virtual endoscopy to the 2D cross-sectional images. *Neuroradiology,* 44**,** 783-90.

Rubinstein, J. T., Parkinson, W. S., Tyler, R. S. & Gantz, B. J. 1999. Residual speech recognition and cochlear implant performance: effects of implantation criteria. *Am J Otol,* 20**,** 445-52.

Ruivo, J., Mermuys, K., Bacher, K., Kuhweide, R., Offeciers, E. & Casselman, J. W. 2009. Cone beam computed tomography, a low-dose imaging technique in the postoperative assessment of cochlear implantation. *Otol Neurotol,* 30**,** 299-303.

Sakellarios, A. I., Tachos, N. S., Rigas, G., Bibas, T., Ni, G., Böhnke, F. & Fotiadis, D. I. 2017. A validated methodology for the 3D reconstruction of cochlea geometries using human microCT images. *Measurement Science and Technology,* 28**,** 054001.

Salt, A. N., Henson, M. M., Gewalt, S. L., Keating, A. W., Demott, J. E. & Henson Jr, O. W. 1995. Detection and quantification of endolymphatic hydrops in the guinea pig cochlea by magnetic resonance microscopy. *Hear Res,* 88**,** 79-86.

Sato, H., Sando, I. & Takahashi, H. 1991. Sexual dimorphism and development of the human cochlea. Computer 3-D measurement. *Acta Otolaryngol,* 111**,** 1037-40.

Saunders, E., Cohen, L., Aschendorff, A., Shapiro, W., Knight, M., Stecker, M., Richter, B., Waltzman, S., Tykocinski, M., Roland, T., Laszig, R. & Cowan, R. 2002. Threshold, Comfortable Level and Impedance Changes as a Function of Electrode-Modiolar Distance. *Ear Hear,* 23**,** 28S-40S.

Schick, B., Brors, D., Koch, O., Schafers, M. & Kahle, G. 2001. Magnetic resonance imaging in patients with sudden hearing loss, tinnitus and vertigo. *Otol Neurotol,* 22**,** 808-12.

Seeber, B. U. & Bruce, I. C. 2016. The history and future of neural modeling for cochlear implants. *Network,* 27**,** 53-66.

Seemann, M., Seemann, O., Bonel, H., Suckfüll, M., Englmeier, K.-H., Naumann, A., Allen, C. & Reiser, M. 1999. Evaluation of the middle and inner ear structures: comparison of hybrid rendering, virtual endoscopy and axial 2D source images. *Eur Radiol,* 9**,** 1851-1858.

Seitz, J., Held, P., Waldeck, A., Strotzer, M., Volk, M., Strutz, J. & Feuerbach, S. 2001. Value of high-resolution MR in patients scheduled for cochlear implantation. *Acta Radiol,* 42**,** 568-73.

Sennaroglu, L., Saatci, I., Aralasmak, A., Gursel, B. & Turan, E. 2002. Magnetic resonance imaging versus computed tomography in pre-operative evaluation of cochlear implant candidates with congenital hearing loss. *J Laryngol Otol,* 116**,** 804-10.

Shepherd, R. K., Hatsushika, S. & Clark, G. M. 1993. Electrical stimulation of the auditory nerve: The effect of electrode position on neural excitation. *Hear Res,* 66**,** 108-120.

Shin, K. J., Lee, J. Y., Kim, J. N., Yoo, J. Y., Shin, C., Song, W. C. & Koh, K. S. 2013. Quantitative analysis of the cochlea using three-dimensional reconstruction based on microcomputed tomographic images. *Anat Rec,* 296**,** 1083-8.

Skinner, M. W., Ketten, D. R., Holden, L. K., Harding, G. W., Smith, P. G., Gates, G. A., Neely, J. G., Kletzker, G. R., Brunsden, B. & Blocker, B. 2002. CT-derived estimation of cochlear morphology and electrode array position in relation to word recognition in Nucleus-22 recipients. *J Assoc Res Otolaryngol,* 3**,** 332-50.

Steele, C. R. & Taber, L. A. 1979. Comparison of WKB calculations and experimental results for three-dimensional cochlear models. *J Acoust Soc Am,* 65**,** 1007-1018.

Stickney, G. S., Loizou, P. C., Mishra, L. N., Assmann, P. F., Shannon, R. V. & Opie, J. M. 2006. Effects of electrode design and configuration on channel interactions. *Hear Res,* 211**,** 33-45.

Suesserman, M. F. & Spelman, F. A. 1993. Lumped-parameter model for in vivo cochlear stimulation. *IEEE Trans Biomed Eng,* 40**,** 237-245.

Summerfield, A. & Marshall, D. 1995. Preoperative predictors of outcomes from cochlear implantation in adults: performance and quality of life. *Ann Otol Rhinol Laryngol,* 166**,** 105-108.

Taha, T., Wahba, H., Ibrahim, A. S. & Abdelazim, Y. 2015. Cochlear implant tailored imaging protocol: What clinicians need to know. *EJRNM,* 46**,** 33-43.

Takagi, A. & Sando, I. 1989. Computer-Aided Three-Dimensional Reconstruction: A Method of Measuring Temporal Bone Structures Including the Length of the Cochlea. *Ann Otol Rhinol Laryngol,* 98**,** 515-522.

Thorne, M., Salt, A. N., Demott, J. E., Henson, M. M., Henson, O. W. & Gewalt, S. L. 1999. Cochlear Fluid Space Dimensions for Six Species Derived From Reconstructions of Three-Dimensional Magnetic Resonance Images. *Laryngoscope,* 109**,** 1661-1668.

Tian, Q., Linthicum, F. H., Jr. & Fayad, J. N. 2006. Human cochleae with three turns: an unreported malformation. *Laryngoscope,* 116**,** 800-3.

Timm, M. E., Majdani, O., Weller, T., Windeler, M., Lenarz, T., Büchner, A. & Salcher, R. B. 2018. Patient specific selection of lateral wall cochlear implant electrodes based on anatomical indication ranges. *PLoS One,* 13**,** e0206435.

Tong, Y. C., Busby, P. A. & Clark, G. M. 1988. Perceptual studies on cochlear implant patients with early onset of profound hearing impairment prior to normal development of auditory, speech, and language skills. *J Acoust Soc Am,* 84**,** 951-962.

Tóth, M., Alpár, A., Bodon, G., Moser, G. & Patonay, L. 2006. Surgical anatomy of the cochlea for cochlear implantation. *Ann Anat,* 188**,** 363-370.

Tran, P., Sue, A., Wong, P., Li, Q. & Carter, P. 2015. Development of HEATHER for cochlear implant stimulation using a new modeling workflow. *IEEE Trans Biomed Eng,* 62**,** 728-735.

Tykocinski, M., Saunders, E., Cohen, L. T., Treaba, C., Briggs, R. J. S., Gibson, P., Clark, G. M. & Cowan, R. S. C. 2001. The Contour Electrode Array: Safety Study and Initial Patient Trials of a New Perimodiolar Design. *Otol Neurotol,* 22**,** 33-41.

Vaid, S. & Vaid, N. 2014. Imaging for cochlear implantation: structuring a clinically relevant report. *Clin Radiol,* 69**,** e9-e24.

Van Der Marel, K. S., Briaire, J. J., Wolterbeek, R., Snel-Bongers, J., Verbist, B. M. & Frijns, J. H. 2014. Diversity in cochlear morphology and its influence on cochlear implant electrode position. *Ear Hear,* 35**,** e9-20.

Van Wermeskerken, G. K., Prokop, M., Van Olphen, A. F. & Albers, F. W. 2007. Intracochlear assessment of electrode position after cochlear implant surgery by means of multislice computer tomography. *Eur Arch Otorhinolaryngol,* 264**,** 1405-7.

Van Wermeskerken, G. K., Van Olphen, A. F. & Graamans, K. 2009. Imaging of electrode position in relation to electrode functioning after cochlear implantation. *Eur Arch Otorhinolaryngol,* 266**,** 1527-31.

Vargas, J. L., Sainz, M., Roldan, C., Alvarez, I. & De La Torre, A. 2013. Analysis of electrical thresholds and maximum comfortable levels in cochlear implant patients. *Auris Nasus Larynx,* 40**,** 260-265.

Veillon, F., Riehm, S., Emachescu, B., Haba, D., Roedlich, M. N., Greget, M. & Tongio, J. 2001. Imaging of the windows of the temporal bone. *Semin Ultrasound CT MR,* 22**,** 271-80.

Verbist, B. M., Ferrarini, L., Briaire, J. J., Zarowski, A., Admiraal-Behloul, F., Olofsen, H., Reiber, J. H. C. & Frijns, J. H. M. 2009. Anatomic Considerations of Cochlear Morphology and Its Implications for Insertion Trauma in Cochlear Implant Surgery. *Otol Neurotol,* 30**,** 471-477.

Verbist, B. M., Frijns, J. H. M., Geleijns, J. & Van Buchem, M. A. 2005. Multisection CT as a valuable tool in the postoperative assessment of cochlear implant patients. *AJNR Am J Neuroradiol,* 26**,** 424-429.

Verbist, B. M., Joemai, R. M. S., Briaire, J. J., Teeuwisse, W. M., Veldkamp, W. J. H. & Frijns, J. H. M. 2010. Cochlear Coordinates in Regard to Cochlear Implantation: A Clinically Individually Applicable 3 Dimensional CT-Based Method. *Otol Neurotol,* 31**,** 738-744.

Vermeire, K., Landsberger, D. M., Van De Heyning, P. H., Voormolen, M., Punte, A. K., Schatzer, R. & Zierhofer, C. 2015. Frequency-place map for electrical stimulation in cochlear implants: Change over time. *Hear Res,* 326**,** 8-14.

Voie, A. H. & Spelman, F. A. 1995. Three-dimensional reconstruction of the cochlea from two-dimensional images of optical sections. *Comput Med Imaging Graph,* 19**,** 377-384.

Volume Graphics. 2010. *3D volume rendering software VGStudio by Volume Graphics.* [Online]. Available: http://www.volumegraphics.com [Accessed].

Wada, H., Sugawara, M., Kobayashi, T., Hozawa, K. & Takasaka, T. 1998. Measurement of guinea pig basilar membrane using computer-aided three-dimensional reconstruction system. *Hear Res,* 120**,** 1-6.

Walby, A. P. 1985. Scala tympani measurement. *Ann Otol Rhinol Laryngol,* 94**,** 393-397.

Wang, H., Northrop, C., Burgess, B., Liberman, M. C. & Merchant, S. N. 2006. Three-Dimensional Virtual Model of the Human Temporal Bone: A Stand-Alone, Downloadable Teaching Tool. *Otol Neurotol,* 27**,** 452-457.

Wanna, G. B., Noble, J. H., Gifford, R. H., Dietrich, M. S., Sweeney, A. D., Zhang, D., Dawant, B. M., Rivas, A. & Labadie, R. F. 2015. Impact of Intrascalar Electrode Location, Electrode Type, and Angular Insertion Depth on Residual Hearing in Cochlear Implant Patients: Preliminary Results. *Otol Neurotol,* 36**,** 1343-8.

Wanna, G. B., Noble, J. H., Mcrrackan, T. R., Dawant, B. M., Dietrich, M. S., Watkins, L., Rivas, A., Schuman, T. A. & Labadie, R. F. 2011. Assessment of electrode placement and audiologic outcomes in bilateral cochlear implantation. *Otol Neurotol,* 32**,** 428.

Wardrop, P., Whinney, D., Rebscher, S. J., Luxford, W. & Leake, P. 2005. A temporal bone study of insertion trauma and intracochlear position of cochlear implant electrodes. II: Comparison of Spiral Clarion and HiFocus II electrodes. *Hear Res,* 203**,** 68-79.

Webster, M. & Sheets, H. D. 2010. A Practical Introduction to Landmark-Based Geometric Morphometrics. *The Paleontological Society Papers,* 16**,** 163-188.

Wilson, B. S., Finley, C. C., Lawson, D. T., Wolford, R. D., Eddington, D. K. & Rabinowitz, W. M. 1991. Better speech recognition with cochlear implants. *Nature,* 352**,** 236-8.

Wimmer, W., Vandersteen, C., Guevara, N., Caversaccio, M. & Delingette, H. 2019. Robust Cochlear Modiolar Axis Detection in CT. *arXiv preprint arXiv:190701870*.

Wong, P., George, S., Tran, P., Sue, A., Carter, P. & Li, Q. 2016. Development and validation of a high-fidelity finite-element model of monopolar stimulation in the implanted Guinea Pig cochlea. *IEEE Trans Biomed Eng,* 63**,** 188-198.

Wu, D. K. & Kelley, M. W. 2012. Molecular Mechanisms of Inner Ear Development. *Cold Spring Harb Perspect Biol,* 4.

Wurfel, W., Lanfermann, H., Lenarz, T. & Majdani, O. 2014. Cochlear length determination using Cone Beam Computed Tomography in a clinical setting. *Hear Res,* 316**,** 65-72.

Wysocki, J. A. 1999. Dimensions of the human vestibular and tympanic scalae. *Hear Res,* 135**,** 39-46.

Xianfen, D., Siping, C., Changhong, L. & Yuanmei, W. 2005. 3D semi-automatic segmentation of the cochlea and inner ear. *Conf Proc IEEE Eng Med Biol Soc,* 6**,** 6285-8.

Xu, J., Xu, S. A., Cohen, L. T. & Clark, G. M. 2000. Cochlear view: postoperative radiography for cochlear implantation. *Am J Otol,* 21**,** 49-56.

Yifang, X. & Collins, L. M. 2005. Predicting dynamic range and intensity discrimination for electrical pulse-train stimuli using a stochastic auditory nerve model: the effects of stimulus noise. *IEEE Trans Biomed Eng,* 52**,** 1040-1049.

Yoo, K. S., Wang, G., Rubinstein, J. T. & Vannier, M. W. 2001. Semiautomatic segmentation of the cochlea using real-time volume rendering and regional adaptive snake modeling. *JDI,* 14**,** 173-81.

Yoo, S. K., Wang, G., Rubinstein, J. T. & Vannier, M. W. 2000. Three-dimensional geometric modeling of the cochlea using helico-spiral approximation. *IEEE Trans Biomed Eng,* 47**,** 1392-402.

Zaghloul, R. a. H., El-Sheikh, M. L., El-Baky, F. a. A. & El-Nouem, K. I. 2011. Role of high resolution CT and radiography in postoperative evaluation of cochlear implantation. *EJRNM,* 42**,** 177-184.

Zohdi, I., Abdelmessih, M. W., El Shennawy, A. M., Ashour, B., Mohamed, B., Kandil, H. & Eldin, G. 2014. Statistical Analysis of Various Factors Affecting the Results of Cochlear Implantation. *J Int Adv Otol,* 10**,** 118-23.

Zou, J., Hannula, M., Lehto, K., Feng, H., Lahelma, J., Aula, A. S., Hyttinen, J. & Pyykko, I. 2015a. X-ray microtomographic confirmation of the reliability of CBCT in identifying the scalar location of cochlear implant electrode after round window insertion. *Hear Res,* 326**,** 59-65.

Zou, J., Lähelmä, J., Koivisto, J., Dhanasingh, A., Jolly, C., Aarnisalo, A., Wolff, J. & Pyykkö, I. 2015b. Imaging cochlear implantation with round window insertion in human temporal bones and cochlear morphological variation using high-resolution cone beam CT. *Acta Otolaryngol,* 135**,** 466-472.

Zrunek, M. & Lischka, M. 1981. Dimensions of the scala vestibuli and sectional areas of both scales. *Eur Arch Otorhinolaryngol,* 233**,** 99-104.

Zrunek, M., Lischka, M., Hochmair-Desoyer, I. & Burian, K. 1980. Dimensions of the scala tympani in relation to the dimaters of multichannel electrodes. *AMA Arch Otolaryngol,* 229**,** 159-165.

ADDENDUM A CSRF TABLES

Table A.1. CSRF for the a.) radius (mean and std) and b.) height (mean and std) for each spiral of the pooled data and for each cochlear class

a.)

Radius (mean)								
Spiral	**LS**	**MS**	**SS**	**IS**	**LSL**	**MSL**	**SLS**	**ILS**
Pooled data (mean)								
Coeff 6	0,021729	0,009557	-0,00601	0,033769	0,00891	0,003193	0,00766	0,026996
Coeff 5	-0,01903	-0,0139	-0,02001	-0,02103	-0,01409	-0,0053	-0,01871	-0,0171
Coeff 4	-0,09849	-0,04879	0,032841	-0,14522	-0,04011	-0,01389	-0,02714	-0,1175
Coeff 3	0,044477	0,031837	0,050079	0,069206	0,035856	0,005608	0,054372	0,05699
Coeff 2	0,160133	0,113918	-0,00698	0,195332	0,097858	0,058196	0,074634	0,179186
Coeff 1	-0,10652	-0,0594	-0,09922	-0,13084	-0,08286	-0,04515	-0,11537	-0,12842
Coeff 0	0,208721	0,059214	0,167348	0,098267	0,140437	0,085452	0,20108	0,167919
Rollercoaster (mean)								
Coeff 6	0,016082	0,009206	-0,00831	0,032362	0,004047	0,002228	0,004217	0,023692
Coeff 5	-0,02723	-0,01652	-0,03051	-0,02547	-0,01772	-0,00517	-0,02677	-0,02147
Coeff 4	-0,07765	-0,04702	0,044297	-0,14447	-0,01939	-0,00979	-0,01003	-0,10366
Coeff 3	0,069942	0,037022	0,082649	0,086156	0,049019	0,005471	0,081346	0,073301
Coeff 2	0,14245	0,113565	-0,02047	0,203072	0,074418	0,052239	0,05572	0,167729
Coeff 1	-0,12044	-0,05829	-0,11608	-0,14444	-0,09034	-0,04445	-0,1304	-0,14128
Coeff 0	0,215695	0,064846	0,175457	0,102042	0,149676	0,099842	0,210089	0,173632
Intermediate (mean)								
Coeff 6	0,020738	0,005823	-0,00893	0,030347	0,006632	0,000785	0,005758	0,026789
Coeff 5	-0,00922	-0,00509	-0,00747	-0,0133	-0,00851	-0,00198	-0,00796	-0,00703
Coeff 4	-0,09277	-0,03424	0,043815	-0,12684	-0,03007	-0,00415	-0,02259	-0,11751
Coeff 3	0,015277	0,005279	0,011409	0,041313	0,017037	-0,00611	0,019857	0,022603
Coeff 2	0,153352	0,101837	-0,01656	0,172559	0,087049	0,051744	0,072142	0,175002
Coeff 1	-0,09507	-0,05447	-0,08279	-0,11332	-0,0718	-0,04206	-0,10261	-0,11145
Coeff 0	0,20604	0,055612	0,162821	0,096252	0,14795	0,066082	0,19595	0,165902
Sloping (mean)								
Coeff 6	0,039456	0,017248	0,005726	0,043881	0,026729	0,009731	0,020799	0,036701
Coeff 5	-0,01346	-0,02232	-0,01286	-0,02234	-0,01384	-0,0109	-0,01525	-0,02285
Coeff 4	-0,1676	-0,07989	-0,0192	-0,18034	-0,11661	-0,04085	-0,08366	-0,15656
Coeff 3	0,024957	0,064848	0,027484	0,071382	0,032448	0,024641	0,040121	0,072626
Coeff 2	0,222242	0,136595	0,048327	0,214335	0,183448	0,084802	0,13252	0,21905
Coeff 1	-0,08773	-0,07139	-0,08107	-0,12385	-0,08157	-0,05162	-0,09583	-0,12256
Coeff 0	0,193837	0,049773	0,152568	0,091222	0,100864	0,074959	0,184841	0,155402
Radius (standard deviation)								
Spiral	**LS**	**MS**	**SS**	**IS**	**LSL**	**MSL**	**SLS**	**ILS**
Pooled data (Standard deviation								
Coeff 6	0,05406	-0,00495	0,021563	0,061981	0,041264	0,05589	0,044899	0,051922
Coeff 5	-0,01706	-0,02149	-0,0368	-0,02192	-0,00894	-0,04377	-0,02494	-0,02204

ADDENDUM A

Coeff 4	-0,23298	-0,04302	-0,09533	-0,28401	-0,15913	-0,24883	-0,18683	-0,2303
Coeff 3	0,021919	0,056674	0,084315	0,059134	-0,01274	0,086237	0,06158	0,061012
Coeff 2	0,311407	0,227962	0,158595	0,385836	0,207415	0,308452	0,26336	0,337011
Coeff 1	-0,08488	-0,09184	-0,082	-0,11886	-0,06852	-0,08374	-0,09931	-0,11384
Coeff 0	0,348213	0,180685	0,31004	0,22666	0,26187	0,15137	0,33234	0,294125
Rollercoaster (standard deviation)								
Coeff 6	0,05988	0,004003	0,076321	0,051785	0,067723	0,010072	0,071683	0,047221
Coeff 5	0,018739	0,001406	0,004287	0,004665	-0,00479	-0,05021	0,004921	0,009544
Coeff 4	-0,25143	-0,06772	-0,31936	-0,23855	-0,30914	-0,03525	-0,30977	-0,21495
Coeff 3	-0,07633	0,002558	-0,03589	-0,04593	-0,05753	0,161111	-0,0312	-0,04549
Coeff 2	0,311003	0,231126	0,369069	0,33517	0,404601	0,127484	0,382593	0,31071
Coeff 1	-0,06437	-0,10685	-0,03728	-0,04541	-0,0499	-0,134	-0,07145	-0,06967
Coeff 0	0,342292	0,167734	0,271655	0,233782	0,210007	0,140544	0,312178	0,301883
Intermediate (standard deviation)								
Coeff 6	-0,04444	-0,0612	-0,1055	0,054744	-0,08169	0,015783	-0,0221	0,027962
Coeff 5	-0,07721	-0,03659	-0,07429	-0,0351	-0,03359	0,008879	-0,03837	-0,0214
Coeff 4	0,170138	0,240607	0,452448	-0,25504	0,392711	-0,02578	0,127545	-0,10703
Coeff 3	0,202624	0,096031	0,183103	0,13631	0,052169	-0,10088	0,087376	0,061612
Coeff 2	-0,06559	-0,13682	-0,39761	0,365436	-0,44208	0,020572	-0,10306	0,153698
Coeff 1	-0,16841	-0,11974	-0,1211	-0,21645	-0,10429	0,009587	-0,12731	-0,15326
Coeff 0	0,380299	0,22671	0,370924	0,205327	0,338111	0,146136	0,362099	0,293851
Sloping (standard deviation)								
Coeff 6	0,05406	-0,00495	0,021563	0,061981	0,041264	0,05589	0,044899	0,051922
Coeff 5	-0,01706	-0,02149	-0,0368	-0,02192	-0,00894	-0,04377	-0,02494	-0,02204
Coeff 4	-0,23298	-0,04302	-0,09533	-0,28401	-0,15913	-0,24883	-0,18683	-0,2303
Coeff 3	0,021919	0,056674	0,084315	0,059134	-0,01274	0,086237	0,06158	0,061012
Coeff 2	0,311407	0,227962	0,158595	0,385836	0,207415	0,308452	0,26336	0,337011
Coeff 1	-0,08488	-0,09184	-0,082	-0,11886	-0,06852	-0,08374	-0,09931	-0,11384
Coeff 0	0,348213	0,180685	0,31004	0,22666	0,26187	0,15137	0,33234	0,294125

b.)

Height (mean)								
Spiral	**LS**	**MS**	**SS**	**IS**	**LSL**	**MSL**	**SLS**	**ILS**
Pooled data								
Coeff 6	0,02629	0,012696	0,039144	0,028694	0,007762	-0,00996	0,045764	0,032742
Coeff 5	-0,00066	-0,09592	-0,03887	-0,04523	-0,01122	-0,01183	-0,01659	-0,03467
Coeff 4	-0,07225	-0,05563	-0,11136	-0,1403	-0,00556	0,039585	-0,17379	-0,12841
Coeff 3	-0,08207	0,262752	0,047161	0,107837	-0,03681	0,008606	-0,04583	0,026012
Coeff 2	0,023568	0,158205	0,036148	0,180812	-0,05231	-0,04487	0,147231	0,102224
Coeff 1	0,572713	0,329682	0,399249	0,460179	0,395385	0,241042	0,490923	0,536724
Coeff 0	1,527706	1,454267	1,892887	1,014085	1,405112	1,343265	1,7331	1,201293
Rollercoaster								
Coeff 6	0,047305	0,043398	0,057302	0,044967	0,007479	-0,00798	0,063758	0,058962
Coeff 5	-0,0124	-0,10707	-0,05417	-0,0645	-0,02197	-0,0187	-0,03483	-0,05899
Coeff 4	-0,14254	-0,18326	-0,16924	-0,2094	0,01219	0,035047	-0,23881	-0,22892
Coeff 3	-0,06955	0,276433	0,0818	0,152972	-0,02145	0,024438	-0,00522	0,087323
Coeff 2	0,076142	0,306813	0,072265	0,256603	-0,09077	-0,0393	0,208704	0,205917
Coeff 1	0,64302	0,40338	0,435522	0,515548	0,439884	0,25609	0,533995	0,580826
Coeff 0	1,620103	1,533795	2,044165	1,043886	1,467088	1,40707	1,855044	1,248544
Intermediate								
Coeff 6	-0,00247	-0,01997	0,015901	0,005316	0,001263	-0,01487	0,02072	0,001536
Coeff 5	0,0116	-0,06969	-0,02094	-0,01425	0,010471	0,001725	0,000639	-0,01451
Coeff 4	0,035087	0,069107	-0,03128	-0,03839	0,013169	0,053783	-0,08109	0,000485
Coeff 3	-0,09293	0,195138	0,00856	0,027802	-0,0855	-0,02767	-0,07935	-0,02356
Coeff 2	-0,07313	0,028329	-0,0295	0,064053	-0,08936	-0,06491	0,057424	-0,04436
Coeff 1	0,508684	0,286796	0,369457	0,438051	0,356241	0,24437	0,451964	0,495698
Coeff 0	1,480329	1,436185	1,789234	1,034318	1,391632	1,317249	1,658855	1,202342
Sloping								
Coeff 6	0,01929	-0,01557	0,029994	0,025407	0,021135	-0,00739	0,04058	0,014984
Coeff 5	0,010591	-0,11337	-0,02795	-0,0477	-0,02111	-0,01461	0,004408	-0,00124
Coeff 4	-0,0703	0,083193	-0,09372	-0,13144	-0,09441	0,028564	-0,15929	-0,0782
Coeff 3	-0,09834	0,352478	0,018646	0,128024	0,011399	0,023701	-0,10187	-0,06062

ADDENDUM A

Coeff 2	0,053783	-0,03304	0,055393	0,180699	0,133473	-0,02686	0,137703	0,076695
Coeff 1	0,48722	0,193333	0,34889	0,338277	0,338608	0,189578	0,438031	0,484755
Coeff 0	1,344439	1,252756	1,643133	0,886491	1,246898	1,192473	1,513825	1,058828
Height (standard deviation)								
Spiral	**LS**	**MS**	**SS**	**IS**	**LSL**	**MSL**	**SLS**	**ILS**
Pooled data								
Coeff 6	0,043235	0,019366	0,044384	0,058911	0,011811	-0,03055	0,048205	0,044453
Coeff 5	0,00236	0,01099	-0,04096	-0,00246	-0,00676	-0,08695	-0,03929	0,0041
Coeff 4	-0,18463	-0,14525	-0,15567	-0,36651	-0,09162	-0,04038	-0,19421	-0,25996
Coeff 3	-0,0528	-0,05215	0,08518	-0,0014	0,006119	0,169939	0,075563	-0,03842
Coeff 2	0,244895	0,32592	0,155959	0,72511	0,231592	0,304922	0,236246	0,490638
Coeff 1	0,180116	0,157469	0,132354	0,074594	0,12017	0,119395	0,143166	0,124082
Coeff 0	0,349272	0,362459	0,518918	0,057004	0,341982	0,341134	0,428056	0,174642
Rollercoaster								
Coeff 6	0,010293	-0,02284	0,014505	0,082686	0,05974	0,032864	0,032986	0,049806
Coeff 5	0,000902	-0,0323	-0,05111	0,014961	0,042824	0,032203	-0,03418	0,009478
Coeff 4	-0,07515	0,019108	-0,06188	-0,46165	-0,36522	-0,29051	-0,1436	-0,30544
Coeff 3	-0,01459	0,137493	0,139089	-0,04662	-0,21008	-0,11661	0,090125	-0,01967
Coeff 2	0,167648	0,204378	0,117765	0,771972	0,532695	0,657088	0,197077	0,559607
Coeff 1	0,076999	-0,05584	0,031046	0,032745	0,151703	0,181417	0,038695	0,026987
Coeff 0	0,351448	0,253283	0,47267	0,046022	0,240416	0,205022	0,394755	0,132482
Intermediate								
Coeff 6	-0,02144	0,027171	0,008697	0,078928	-0,04924	0,184707	-0,00888	-0,01737
Coeff 5	0,024657	0,070668	0,011105	0,041658	-0,03667	0,073498	0,009434	0,019685
Coeff 4	0,096145	-0,16717	-0,02296	-0,37715	0,197288	-0,77643	0,030144	0,031176
Coeff 3	-0,11369	-0,25059	-0,07283	-0,16254	0,127594	-0,36282	-0,0809	-0,11184
Coeff 2	-0,07453	0,225095	0,013515	0,621871	-0,12655	0,720194	0,003948	0,118155
Coeff 1	0,21266	0,256764	0,226593	0,17613	0,051108	0,344886	0,254926	0,215328
Coeff 0	0,318454	0,486468	0,401455	0,062181	0,325004	0,233657	0,365701	0,225798
Sloping								
Coeff 6	0,043235	0,019366	0,044384	0,058911	0,011811	-0,03055	0,048205	0,044453
Coeff 5	0,00236	0,01099	-0,04096	-0,00246	-0,00676	-0,08695	-0,03929	0,0041
Coeff 4	-0,18463	-0,14525	-0,15567	-0,36651	-0,09162	-0,04038	-0,19421	-0,25996
Coeff 3	-0,0528	-0,05215	0,08518	-0,0014	0,006119	0,169939	0,075563	-0,03842
Coeff 2	0,244895	0,32592	0,155959	0,72511	0,231592	0,304922	0,236246	0,490638
Coeff 1	0,180116	0,157469	0,132354	0,074594	0,12017	0,119395	0,143166	0,124082
Coeff 0	0,349272	0,362459	0,518918	0,057004	0,341982	0,341134	0,428056	0,174642

ADDENDUM A

Table A.2. PNMAE ranked in order of error. The polynomial equation for each reference spiral is also given for a) radius and b.) height of each obscured spiral.

a.)

To predict MS										
Class	**Intermediate**					**Rollercoaster**				
Reference	**LS**	**SS**	**IS**	**SLS**	**ILS**	**LS**	**SS**	**IS**	**SLS**	**ILS**
PNMAE 720º	0,519	0,487	0,684	0,493	0,558	1,043	0,885	0,957	0,953	0,943
Rank PNMAE	3	1	5	2	4	5	1	4	3	2
Predictor coeff										
Coeff 6	0,014	-0,014	0,023	0,000	0,020	0,007	-0,017	0,022	-0,005	0,014
Coeff 5	-0,004	-0,002	-0,008	-0,003	-0,002	-0,010	-0,014	-0,009	-0,010	-0,005
Coeff 4	-0,056	0,075	-0,089	0,011	-0,080	-0,030	0,089	-0,094	0,036	-0,055
Coeff 3	0,010	0,006	0,035	0,014	0,017	0,032	0,044	0,048	0,043	0,035
Coeff 2	0,049	-0,113	0,068	-0,028	0,070	0,028	-0,130	0,087	-0,056	0,053
Coeff 1	-0,039	-0,027	-0,056	-0,046	-0,055	-0,060	-0,056	-0,084	-0,070	-0,080
Coeff 0	0,144	0,103	0,039	0,134	0,106	0,146	0,107	0,036	0,141	0,105
Class	**Sloping**					**Pooled**				
Reference	**LS**	**SS**	**IS**	**SLS**	**ILS**	**LS**	**SS**	**IS**	**SLS**	**ILS**
PNMAE 720º	0,518	0,329	0,296	0,452	0,417	2,021	1,860	2,068	1,906	1,905
Rank PNMAE	5	2	1	4	3	4	1	5	3	2
Predictor coeff										
Coeff 6	0,027	-0,014	0,032	0,004	0,023	0,012	-0,016	0,024	-0,002	0,017
Coeff 5	0,011	0,011	0,000	0,008	-0,001	-0,005	-0,006	-0,007	-0,005	-0,003
Coeff 4	-0,105	0,073	-0,121	-0,005	-0,092	-0,050	0,082	-0,096	0,022	-0,069
Coeff 3	-0,048	-0,045	0,008	-0,030	0,009	0,013	0,018	0,037	0,023	0,025
Coeff 2	0,103	-0,106	0,093	-0,005	0,099	0,046	-0,121	0,081	-0,039	0,065
Coeff 1	-0,020	-0,012	-0,063	-0,029	-0,061	-0,047	-0,040	-0,071	-0,056	-0,069
Coeff 0	0,173	0,123	0,050	0,162	0,127	0,150	0,108	0,039	0,142	0,109
To predict SS										
Class	**Intermediate**					**Rollercoaster**				
Reference	LS		IS	SLS	ILS	LS		IS	SLS	ILS
PNMAE 720º	0,400		0,706	0,262	0,536	0,565		0,934	0,357	0,696
Rank PNMAE	2		1	3	4	2		1	3	4
Predictor coeff										
Coeff 6	0,028		0,038	0,014	0,034	0,024		0,039	0,012	0,031
Coeff 5	-0,002		-0,006	0,000	0,000	0,003		0,005	0,004	0,009
Coeff 4	-0,131		-0,163	-0,064	-0,155	-0,118		-0,183	-0,053	-0,143
Coeff 3	0,004		0,029	0,008	0,011	-0,012		0,003	-0,001	-0,009
Coeff 2	0,163		0,181	0,085	0,184	0,158		0,217	0,074	0,182
Coeff 1	-0,012		-0,029	-0,019	-0,027	-0,004		-0,028	-0,014	-0,024
Coeff 0	0,041		-0,064	0,032	0,003	0,039		-0,071	0,034	-0,002
Class	**Sloping**					**Pooled**				
Reference	LS		IS	SLS	ILS	LS		IS	SLS	ILS
PNMAE 720º	0,270		0,229	0,190	0,214	1,149		1,932	0,745	1,495
Rank PNMAE	3		1	2	4	2		1	3	4
Predictor coeff										
Coeff 6	0,041		0,046	0,018	0,037	0,028		0,040	0,014	0,033
Coeff 5	-0,001		-0,011	-0,003	-0,012	0,001		-0,001	0,001	0,003
Coeff 4	-0,178		-0,194	-0,077	-0,165	-0,131		-0,178	-0,060	-0,150

ADDENDUM A

Coeff 3	-0,003		0,053	0,015	0,054	-0,006		0,019	0,004	0,007
Coeff 2	0,209		0,199	0,101	0,205	0,167		0,202	0,082	0,186
Coeff 1	-0,008		-0,051	-0,018	-0,050	-0,007		-0,032	-0,016	-0,029
Coeff 0	0,050		-0,074	0,039	0,003	0,041		-0,069	0,034	0,001
To predict IS										
Class	**Intermediate**					**Rollercoaster**				
Reference	LS	SS		SLS	ILS	LS	SS		SLS	ILS
PNMAE 720º	0,511	0,698		0,563	0,440	0,819	0,933		0,897	0,414
Rank PNMAE	2	3		1	4	2	3		1	4
Predictor coeff										
Coeff 6	-0,009	-0,038		-0,024	-0,003	-0,016	-0,039		-0,027	-0,008
Coeff 5	0,004	0,006		0,005	0,006	-0,002	-0,005		-0,001	0,004
Coeff 4	0,033	0,163		0,100	0,009	0,065	0,183		0,130	0,040
Coeff 3	-0,025	-0,029		-0,021	-0,018	-0,016	-0,003		-0,005	-0,012
Coeff 2	-0,018	-0,181		-0,096	0,002	-0,059	-0,217		-0,143	-0,034
Coeff 1	0,017	0,029		0,010	0,002	0,023	0,028		0,014	0,003
Coeff 0	0,105	0,064		0,096	0,067	0,110	0,071		0,105	0,069
Class	**Sloping**					**Pooled**				
Reference	LS	SS		SLS	ILS	LS	SS		SLS	ILS
PNMAE 720º	0,354	0,229		0,292	0,235	1,510	1,925		1,712	0,997
Rank PNMAE	3	2		1	4	2	3		1	4
Predictor coeff										
Coeff 6	-0,005	-0,046	0,000	-0,028	-0,009	-0,012	-0,040	0,000	-0,026	-0,007
Coeff 5	0,011	0,011	0,000	0,009	-0,001	0,002	0,001	0,000	0,002	0,004
Coeff 4	0,015	0,194	0,000	0,116	0,029	0,047	0,178	0,000	0,118	0,028
Coeff 3	-0,056	-0,053	0,000	-0,038	0,001	-0,025	-0,019	0,000	-0,015	-0,012
Coeff 2	0,009	-0,199	0,000	-0,098	0,006	-0,035	-0,202	0,000	-0,121	-0,016
Coeff 1	0,043	0,051	0,000	0,034	0,002	0,024	0,032	0,000	0,015	0,002
Coeff 0	0,123	0,074	0,000	0,112	0,077	0,110	0,069	0,000	0,103	0,070
To predict LSL										
Class	**Intermediate**					**Rollercoaster**				
Reference	LS	SS	IS	SLS	ILS	LS	SS	IS	SLS	ILS
PNMAE 720º	0,718	0,812	0,778	0,745	0,864	1,471	1,589	1,394	1,497	1,346
Rank PNMAE	1	4	3	2	5	3	5	2	4	1
Predictor coeff										
Coeff 6	0,014	-0,015	0,023	-0,001	0,019	0,012	-0,012	0,027	0,000	0,019
Coeff 5	-0,001	0,001	-0,005	0,001	0,001	-0,009	-0,012	-0,008	-0,009	-0,004
Coeff 4	-0,060	0,071	-0,093	0,007	-0,084	-0,056	0,062	-0,121	0,009	-0,082
Coeff 3	-0,002	-0,005	0,023	0,003	0,005	0,020	0,033	0,036	0,031	0,024
Coeff 2	0,064	-0,099	0,082	-0,014	0,084	0,066	-0,092	0,125	-0,018	0,090
Coeff 1	-0,022	-0,011	-0,040	-0,030	-0,038	-0,029	-0,025	-0,052	-0,039	-0,049
Coeff 0	0,056	0,014	-0,050	0,046	0,017	0,064	0,025	-0,046	0,059	0,023
Class	**Sloping**					**Pooled**				
Reference	LS	SS	IS	SLS	ILS	LS	SS	IS	SLS	ILS
PNMAE 720º	0,295	0,160	0,162	0,233	0,201	2,322	2,643	2,473	2,450	2,290
Rank PNMAE	5	1	2	4	3	2	5	4	3	1
Predictor coeff										
Coeff 6	0,015	-0,025	0,021	-0,007	0,012	0,013	-0,015	0,025	-0,001	0,018
Coeff 5	0,000	0,001	-0,010	-0,002	-0,011	-0,005	-0,006	-0,007	-0,005	-0,003
Coeff 4	-0,061	0,117	-0,077	0,040	-0,048	-0,058	0,073	-0,105	0,013	-0,077
Coeff 3	-0,009	-0,006	0,047	0,009	0,048	0,009	0,014	0,033	0,019	0,021

ADDENDUM A

Coeff 2	0,047	-0,162	0,037	-0,061	0,043	0,062	-0,105	0,097	-0,023	0,081
Coeff 1	-0,007	0,001	-0,051	-0,017	-0,049	-0,024	-0,016	-0,048	-0,033	-0,046
Coeff 0	0,112	0,062	-0,012	0,101	0,066	0,068	0,027	-0,042	0,061	0,027
To predict MSL										
Class	**Intermediate**					**Rollercoaster**				
Reference	LS	SS	IS	SLS	ILS	LS	SS	IS	SLS	ILS
PNMAE 720º	0,535	0,525	0,767	0,513	0,632	1,466	1,433	1,415	1,428	1,383
Rank PNMAE	3	1	5	2	4	5	4	2	3	1
Predictor coeff										
Coeff 6	0,015	-0,014	0,026	0,002	0,023	0,013	-0,010	0,029	0,002	0,021
Coeff 5	-0,008	-0,005	-0,012	-0,005	-0,006	-0,021	-0,025	-0,020	-0,021	-0,016
Coeff 4	-0,065	0,065	-0,105	-0,003	-0,098	-0,066	0,052	-0,131	0,000	-0,091
Coeff 3	0,026	0,016	0,050	0,023	0,030	0,062	0,075	0,078	0,074	0,066
Coeff 2	0,075	-0,086	0,100	0,001	0,105	0,087	-0,070	0,146	0,003	0,112
Coeff 1	-0,052	-0,035	-0,067	-0,055	-0,066	-0,074	-0,069	-0,097	-0,083	-0,094
Coeff 0	0,132	0,093	0,029	0,123	0,093	0,112	0,073	0,002	0,107	0,072
Class	**Sloping**					**Pooled**				
Reference	LS	SS	IS	SLS	ILS	LS	SS	IS	SLS	ILS
PNMAE 720º	0,454	0,260	0,249	0,367	0,328	1,939	2,162	2,418	2,061	2,101
Rank PNMAE	5	2	1	4	3	1	4	5	2	3
Predictor coeff										
Coeff 6	0,036	-0,005	0,041	0,013	0,032	0,017	-0,010	0,030	0,004	0,023
Coeff 5	-0,003	-0,002	-0,014	-0,005	-0,014	-0,014	-0,015	-0,016	-0,014	-0,012
Coeff 4	-0,152	0,026	-0,168	-0,051	-0,139	-0,079	0,052	-0,128	-0,009	-0,101
Coeff 3	0,000	0,003	0,056	0,019	0,058	0,042	0,046	0,066	0,050	0,054
Coeff 2	0,165	-0,044	0,156	0,057	0,161	0,096	-0,071	0,133	0,011	0,117
Coeff 1	-0,043	-0,035	-0,087	-0,053	-0,085	-0,062	-0,054	-0,086	-0,070	-0,084
Coeff 0	0,143	0,093	0,020	0,132	0,097	0,123	0,082	0,013	0,116	0,082
To predict SLS										
Class	**Intermediate**					**Rollercoaster**				
Reference	LS	SS	IS		ILS	LS	SS	IS		ILS
PNMAE 720º	0,217	0,262	0,569		0,370	0,782	1,068	1,527		1,438
Rank PNMAE	1	2	3		4	1	2	4		3
Predictor coeff										
Coeff 6	0,014	-0,014	0,024		0,020	0,012	-0,012	0,027		0,019
Coeff 5	-0,001	0,000	-0,005		0,001	0,000	-0,004	0,001		0,005
Coeff 4	-0,067	0,064	-0,100		-0,091	-0,066	0,053	-0,130		-0,091
Coeff 3	-0,004	-0,008	0,021		0,003	-0,011	0,001	0,005		-0,008
Coeff 2	0,078	-0,085	0,096		0,099	0,084	-0,074	0,143		0,109
Coeff 1	0,007	0,019	-0,010		-0,008	0,010	0,014	-0,014		-0,011
Coeff 0	0,010	-0,032	-0,096		-0,029	0,005	-0,034	-0,105		-0,035
Class	**Sloping**					**Pooled**				
Reference	LS	SS	IS		ILS	LS	SS	IS		ILS
PNMAE 720º	0,120	0,190	0,291		0,116	0,666	0,745	1,719		1,127
Rank PNMAE	1	2	3		4	1	2	4	3	5
Predictor coeff										
Coeff 6	0,022	-0,018	0,028		0,019	0,014	-0,014	0,026		0,019
Coeff 5	0,002	0,003	-0,009		-0,009	0,000	-0,001	-0,002		0,002
Coeff 4	-0,101	0,077	-0,116		-0,088	-0,071	0,060	-0,118		-0,090
Coeff 3	-0,018	-0,015	0,038		0,039	-0,010	-0,004	0,015		0,003
Coeff 2	0,108	-0,101	0,098		0,104	0,085	-0,082	0,121		0,105

ADDENDUM A

Coeff 1	0,010	0,018	-0,034		-0,032	0,009	0,016	-0,015		-0,013
Coeff 0	0,011	-0,039	-0,112		-0,035	0,008	-0,034	-0,103		-0,033
To predict ILS										
Class	**Intermediate**					**Rollercoaster**				
Reference	LS	SS	IS	SLS		LS	SS	IS	SLS	
PNMAE 720º	0,361	0,538	0,448	0,373		0,489	0,697	0,414	0,582	
Rank PNMAE	1	4	3	2		2	4	1	3	
Predictor coeff										
Coeff 6	-0,006	-0,034	0,003	-0,020		-0,007	-0,031	0,008	-0,019	
Coeff 5	-0,002	0,000	-0,006	-0,001		-0,006	-0,009	-0,004	-0,005	
Coeff 4	0,024	0,155	-0,009	0,091		0,025	0,143	-0,040	0,091	
Coeff 3	-0,007	-0,011	0,018	-0,003		-0,003	0,009	0,012	0,008	
Coeff 2	-0,021	-0,184	-0,002	-0,099		-0,025	-0,182	0,034	-0,109	
Coeff 1	0,016	0,027	-0,002	0,008		0,020	0,024	-0,003	0,011	
Coeff 0	0,038	-0,003	-0,067	0,029		0,041	0,002	-0,069	0,035	
Class	**Sloping**					**Pooled**				
Reference	LS	SS	IS	SLS		LS	SS	IS	SLS	
PNMAE 720º	0,146	0,217	0,234	0,115		0,982	1,493	1,006	1,127	
Rank PNMAE	2	3	4	1		1	4	2	3	
Predictor coeff										
Coeff 6	0,003	-0,037	0,009	-0,019		-0,005	-0,033	0,007	-0,019	
Coeff 5	0,011	0,012	0,001	0,009		-0,002	-0,003	-0,004	-0,002	
Coeff 4	-0,013	0,165	-0,029	0,088		0,019	0,150	-0,028	0,090	
Coeff 3	-0,057	-0,054	-0,001	-0,039		-0,013	-0,007	0,012	-0,003	
Coeff 2	0,004	-0,205	-0,006	-0,104		-0,019	-0,186	0,016	-0,105	
Coeff 1	0,042	0,050	-0,002	0,032		0,022	0,029	-0,002	0,013	
Coeff 0	0,046	-0,003	-0,077	0,035		0,041	-0,001	-0,070	0,033	
b.)										
To predict MS										
Class	**Intermediate**					**Rollercoaster**				
Reference	LS	SS	IS	SLS	ILS	LS	SS	IS	SLS	ILS
PNMAE 720º	1,119	1,164	1,210	1,192	1,207	2,392	2,481	1,894	2,312	2,169
Rank PNMAE	1	2	5	3	4	4	5	1	3	2
Predictor coeff										
Coeff 6	0,017	0,035	0,025	0,040	0,021	0,004	0,014	0,002	0,020	0,015
Coeff 5	0,080	0,048	0,054	0,069	0,054	0,092	0,051	0,041	0,070	0,047
Coeff 4	-0,033	-0,098	-0,105	-0,147	-0,067	0,040	0,014	-0,025	-0,054	-0,044
Coeff 3	-0,282	-0,183	-0,164	-0,269	-0,214	-0,336	-0,189	-0,120	-0,274	-0,184
Coeff 2	-0,099	-0,057	0,035	0,029	-0,071	-0,224	-0,228	-0,049	-0,095	-0,098
Coeff 1	0,218	0,081	0,148	0,162	0,205	0,233	0,031	0,109	0,127	0,172
Coeff 0	0,043	0,346	-0,394	0,218	-0,229	0,084	0,496	-0,476	0,312	-0,277
Class	**Sloping**					**Pooled**				
Reference	LS	SS	IS	SLS	ILS	LS	SS	IS	SLS	ILS
PNMAE 720º	0,441	0,563	0,621	0,504	0,564	4,271	4,405	4,373	4,119	4,395
Rank PNMAE	1	3	5	2	4	2	5	3	1	4
Predictor coeff										
Coeff 6	0,040	0,052	0,047	0,064	0,035	0,014	0,026	0,016	0,033	0,020
Coeff 5	0,142	0,098	0,075	0,135	0,128	0,095	0,057	0,051	0,079	0,061
Coeff 4	-0,176	-0,202	-0,246	-0,277	-0,185	-0,017	-0,056	-0,085	-0,118	-0,073
Coeff 3	-0,516	-0,382	-0,257	-0,520	-0,473	-0,345	-0,216	-0,155	-0,309	-0,237
Coeff 2	0,099	0,101	0,245	0,195	0,126	-0,135	-0,122	0,023	-0,011	-0,056

ADDENDUM A

Coeff 1	0,336	0,178	0,166	0,280	0,333	0,243	0,070	0,130	0,161	0,207
Coeff 0	0,105	0,447	-0,419	0,299	-0,222	0,073	0,439	-0,440	0,279	-0,253
To predict SS										
Class	**Intermediate**					**Rollercoaster**				
Reference	LS		IS	SLS	ILS	LS		IS	SLS	ILS
PNMAE 720º	0,446		0,835	0,232	0,673	0,888		2,114	0,481	1,585
Rank PNMAE	2		1	3	4	2		1	3	4
Predictor coeff										
Coeff 6	-0,018		-0,010	0,005	-0,014	-0,010		-0,012	0,006	0,002
Coeff 5	0,032		0,007	0,021	0,006	0,041		-0,010	0,019	-0,005
Coeff 4	0,065		-0,007	-0,049	0,031	0,026		-0,039	-0,068	-0,058
Coeff 3	-0,100		0,019	-0,086	-0,031	-0,147		0,069	-0,085	0,005
Coeff 2	-0,043		0,092	0,085	-0,015	0,004		0,179	0,133	0,130
Coeff 1	0,137		0,067	0,081	0,124	0,202		0,078	0,096	0,141
Coeff 0	-0,303		-0,740	-0,128	-0,575	-0,412		-0,972	-0,184	-0,773
Class	**Sloping**					**Pooled**				
Reference	LS		IS	SLS	ILS	LS		IS	SLS	ILS
PNMAE 720º	0,298		0,607	0,113	0,523	2,487		5,224	1,126	4,159
Rank PNMAE	2		1	3	4	2		1	3	4
Predictor coeff										
Coeff 6	-0,012		-0,005	0,012	-0,017	-0,013		-0,010	0,007	-0,006
Coeff 5	0,044		-0,023	0,037	0,031	0,038		-0,006	0,022	0,004
Coeff 4	0,027		-0,043	-0,075	0,018	0,039		-0,029	-0,062	-0,017
Coeff 3	-0,134		0,125	-0,138	-0,091	-0,129		0,061	-0,093	-0,021
Coeff 2	-0,002		0,143	0,094	0,024	-0,013		0,145	0,111	0,066
Coeff 1	0,158		-0,012	0,102	0,155	0,173		0,061	0,092	0,137
Coeff 0	-0,342		-0,866	-0,148	-0,668	-0,365		-0,879	-0,160	-0,692
To predict IS										
Class	**Intermediate**					**Rollercoaster**				
Reference	LS	SS		SLS	ILS	LS	SS		SLS	ILS
PNMAE 720º	0,647	0,834		0,776	0,404	1,400	2,117		1,749	0,715
Rank PNMAE	2	3		1	4	2	3		1	4
Predictor coeff										
Coeff 6	-0,008	0,010		0,015	-0,004	0,002	0,012		0,018	0,014
Coeff 5	0,025	-0,007		0,015	0,000	0,051	0,010		0,029	0,005
Coeff 4	0,072	0,007		-0,042	0,038	0,065	0,039		-0,029	-0,019
Coeff 3	-0,118	-0,019		-0,105	-0,050	-0,216	-0,069		-0,154	-0,064
Coeff 2	-0,135	-0,092		-0,006	-0,106	-0,175	-0,179		-0,047	-0,049
Coeff 1	0,069	-0,067		0,014	0,057	0,124	-0,078		0,018	0,063
Coeff 0	0,437	0,740		0,612	0,165	0,560	0,972		0,788	0,199
Class	**Sloping**					**Pooled**				
Reference	LS	SS		SLS	ILS	LS	SS		SLS	ILS
PNMAE 720º	0,370	0,607		0,535	0,163	2,995	5,236		4,297	1,519
Rank PNMAE	2	3		1	4	2	3		1	4
Predictor coeff										
Coeff 6	-0,007	0,005		0,017	-0,012	-0,002	0,010		0,017	0,004
Coeff 5	0,067	0,023		0,060	0,053	0,045	0,006		0,029	0,011
Coeff 4	0,070	0,043		-0,032	0,061	0,068	0,029		-0,033	0,012
Coeff 3	-0,259	-0,125		-0,263	-0,216	-0,190	-0,061		-0,154	-0,082
Coeff 2	-0,145	-0,143		-0,049	-0,119	-0,157	-0,145		-0,034	-0,079
Coeff 1	0,170	0,012		0,114	0,168	0,113	-0,061		0,031	0,077

ADDENDUM A

Coeff 0	0,524	0,866		0,718	0,197	0,514	0,879		0,719	0,187
To predict LSL										
Class	**Intermediate**					**Rollercoaster**				
Reference	LS	SS	IS	SLS	ILS	LS	SS	IS	SLS	ILS
PNMAE 720º	0,882	0,935	0,871	0,948	0,805	1,968	1,802	2,480	1,859	2,129
Rank PNMAE	3	4	2	5	1	3	1	5	2	4
Predictor coeff										
Coeff 6	-0,004	0,014	0,004	0,019	0,000	0,039	0,048	0,036	0,055	0,050
Coeff 5	0,001	-0,031	-0,024	-0,010	-0,024	0,009	-0,031	-0,041	-0,012	-0,036
Coeff 4	0,021	-0,044	-0,051	-0,092	-0,012	-0,150	-0,176	-0,215	-0,244	-0,234
Coeff 3	-0,007	0,092	0,111	0,006	0,061	-0,047	0,100	0,169	0,016	0,106
Coeff 2	0,016	0,059	0,150	0,144	0,044	0,162	0,158	0,337	0,291	0,288
Coeff 1	0,149	0,013	0,080	0,094	0,137	0,197	-0,004	0,074	0,091	0,137
Coeff 0	0,087	0,390	-0,350	0,262	-0,186	0,149	0,561	-0,411	0,377	-0,212
Class	**Sloping**					**Pooled**				
Reference	LS	SS	IS	SLS	ILS	LS	SS	IS	SLS	ILS
PNMAE 720º	0,223	0,297	0,467	0,251	0,386	3,136	3,856	3,978	3,407	3,361
Rank PNMAE	1	3	5	2	4	1	4	5	3	2
Predictor coeff										
Coeff 6	-0,002	0,010	0,005	0,022	-0,007	0,019	0,031	0,021	0,038	0,025
Coeff 5	0,036	-0,008	-0,030	0,029	0,023	0,011	-0,028	-0,034	-0,005	-0,023
Coeff 4	0,028	0,001	-0,042	-0,074	0,019	-0,067	-0,106	-0,135	-0,168	-0,123
Coeff 3	-0,126	0,008	0,133	-0,130	-0,082	-0,045	0,084	0,145	-0,009	0,063
Coeff 2	-0,091	-0,089	0,054	0,005	-0,065	0,076	0,088	0,233	0,200	0,155
Coeff 1	0,170	0,012	0,000	0,114	0,167	0,177	0,004	0,065	0,096	0,141
Coeff 0	0,112	0,453	-0,412	0,305	-0,215	0,123	0,488	-0,391	0,328	-0,204
To predict MSL										
Class	**Intermediate**					**Rollercoaster**				
Reference	LS	SS	IS	SLS	ILS	LS	SS	IS	SLS	ILS
PNMAE 720º	0,681	0,814	0,668	0,790	0,690	1,537	1,381	2,346	1,447	1,824
Rank PNMAE	3	5	1	4	2	3	1	5	2	4
Predictor coeff										
Coeff 6	0,013	0,029	0,013	0,033	0,014	0,054	0,063	0,051	0,070	0,065
Coeff 5	0,012	-0,021	-0,013	0,001	-0,014	0,006	-0,034	-0,044	-0,016	-0,039
Coeff 4	-0,026	-0,079	-0,063	-0,126	-0,044	-0,173	-0,198	-0,237	-0,266	-0,256
Coeff 3	-0,067	0,033	0,051	-0,055	0,002	-0,091	0,056	0,125	-0,029	0,061
Coeff 2	0,006	0,033	0,104	0,116	0,014	0,112	0,108	0,287	0,241	0,238
Coeff 1	0,247	0,112	0,175	0,191	0,231	0,376	0,174	0,252	0,270	0,315
Coeff 0	0,149	0,448	-0,277	0,324	-0,115	0,207	0,619	-0,353	0,435	-0,154
Class	**Sloping**					**Pooled**				
Reference	LS	SS	IS	SLS	ILS	LS	SS	IS	SLS	ILS
PNMAE 720º	0,330	0,513	0,389	0,423	0,375	2,842	3,376	4,168	2,914	3,388
Rank PNMAE	1	5	3	4	2	1	3	5	2	4
Predictor coeff										
Coeff 6	0,031	0,043	0,038	0,055	0,026	0,038	0,050	0,038	0,056	0,043
Coeff 5	0,029	-0,015	-0,038	0,022	0,015	0,011	-0,027	-0,034	-0,005	-0,023
Coeff 4	-0,113	-0,140	-0,183	-0,215	-0,122	-0,118	-0,153	-0,175	-0,215	-0,171
Coeff 3	-0,140	-0,006	0,119	-0,144	-0,096	-0,091	0,039	0,101	-0,055	0,019
Coeff 2	0,092	0,094	0,237	0,188	0,118	0,076	0,083	0,223	0,194	0,151
Coeff 1	0,340	0,182	0,170	0,284	0,338	0,331	0,156	0,216	0,248	0,293
Coeff 0	0,174	0,516	-0,350	0,368	-0,153	0,184	0,550	-0,329	0,390	-0,142

ADDENDUM A

To predict SLS										
Class	**Intermediate**					**Rollercoaster**				
Reference	LS	SS	IS		ILS	LS	SS	IS		ILS
PNMAE 720º	0,312	0,232	0,777		0,603	0,561	0,483	1,753		1,213
Rank PNMAE	2	1	3		4	2	1	3		4
Predictor coeff										
Coeff 6	-0,023	-0,005	-0,015		-0,019	-0,016	-0,006	-0,018		-0,005
Coeff 5	0,011	-0,021	-0,015		-0,015	0,022	-0,019	-0,029		-0,023
Coeff 4	0,114	0,049	0,042		0,080	0,094	0,068	0,029		0,010
Coeff 3	-0,013	0,086	0,105		0,055	-0,062	0,085	0,154		0,090
Coeff 2	-0,128	-0,085	0,006		-0,100	-0,129	-0,133	0,047		-0,003
Coeff 1	0,056	-0,081	-0,014		0,043	0,106	-0,096	-0,018		0,045
Coeff 0	-0,175	0,128	-0,612		-0,448	-0,228	0,184	-0,788		-0,589
Class	**Sloping**					**Pooled**				
Reference	LS	SS	IS		ILS	LS	SS	IS		ILS
PNMAE 720º	0,215	0,113	0,537		0,446	1,567	1,129	4,296		3,198
Rank PNMAE	2	1	3		4	2	1	3		4
Predictor coeff										
Coeff 6	-0,024	-0,012	-0,017		-0,029	-0,019	-0,007	-0,017		-0,013
Coeff 5	0,007	-0,037	-0,060		-0,006	0,016	-0,022	-0,029		-0,018
Coeff 4	0,102	0,075	0,032		0,093	0,102	0,062	0,033		0,045
Coeff 3	0,004	0,138	0,263		0,047	-0,036	0,093	0,154		0,072
Coeff 2	-0,096	-0,094	0,049		-0,070	-0,124	-0,111	0,034		-0,045
Coeff 1	0,056	-0,102	-0,114		0,053	0,082	-0,092	-0,031		0,046
Coeff 0	-0,194	0,148	-0,718		-0,520	-0,205	0,160	-0,719		-0,532

To predict ILS										
Class	**Intermediate**					**Rollercoaster**				
Reference	LS	SS	IS	SLS		LS	SS	IS	SLS	
PNMAE 720º	0,495	0,670	0,403	0,600		0,846	1,584	0,719	1,211	
Rank PNMAE	2	4	1	3		2	4	1	3	
Predictor coeff										
Coeff 6	-0,004	0,014	0,004	0,019		-0,011	-0,002	-0,014	0,005	
Coeff 5	0,026	-0,006	0,000	0,015		0,045	0,005	-0,005	0,023	
Coeff 4	0,034	-0,031	-0,038	-0,080		0,084	0,058	0,019	-0,010	
Coeff 3	-0,068	0,031	0,050	-0,055		-0,152	-0,005	0,064	-0,090	
Coeff 2	-0,028	0,015	0,106	0,100		-0,126	-0,130	0,049	0,003	
Coeff 1	0,013	-0,124	-0,057	-0,043		0,060	-0,141	-0,063	-0,045	
Coeff 0	0,273	0,575	-0,165	0,448		0,361	0,773	-0,199	0,589	
Class	**Sloping**					**Pooled**				
Reference	LS	SS	IS	SLS		LS	SS	IS	SLS	
PNMAE 720º	0,245	0,522	0,154	0,443		1,885	4,167	1,503	3,199	
Rank PNMAE	2	4	1	3		2	4	1	3	
Predictor coeff										
Coeff 6	0,005	0,017	0,012	0,029		-0,006	0,006	-0,004	0,013	
Coeff 5	0,014	-0,031	-0,053	0,006		0,034	-0,004	-0,011	0,018	
Coeff 4	0,009	-0,018	-0,061	-0,093		0,056	0,017	-0,012	-0,045	
Coeff 3	-0,043	0,091	0,216	-0,047		-0,108	0,021	0,082	-0,072	
Coeff 2	-0,026	-0,024	0,119	0,070		-0,079	-0,066	0,079	0,045	
Coeff 1	0,003	-0,155	-0,168	-0,053		0,036	-0,137	-0,077	-0,046	
Coeff 0	0,327	0,668	-0,197	0,520		0,326	0,692	-0,187	0,532	

ADDENDUM A